SECTION 1 – SITE CHARACTERIZATION

TABLE OF CONTENTS

Figures

Tables

1.1 Overview

This site characterization for Harvest Bend CCS LLC's (Harvest Bend CCS) White Castle Injection Well (WC IW)-B Well No. 001 and No. 002 was prepared to meet the requirements of Statewide Order (SWO) 29-N-6 **§3607.C.2.m** [Title 40, U.S. Code of Federal Regulations (40 CFR) **§146.82(a)(3)**]. This section describes the regional and site geology for the proposed location. This site characterization incorporates analysis from multiple data types, including core, well logs, seismic (3D), academic and professional publications (e.g., regional geologic frameworks), and nearby subsurface analogs.

1.2 Regional Geology

The proposed White Castle CO_2 Sequestration (White Castle) Project site is located in southeastern Louisiana within the Gulf of Mexico basin. The onshore portion of the basin spans 148,049,000 acres and encompasses portions of Texas, Louisiana, Mississippi, Alabama, Arkansas, Missouri, Kentucky, Tennessee, Florida, and Georgia to the state-waters boundary of the United States (Roberts-Ashby, et al., 2012). The location of the White Castle Project is displayed in Figure 1-1 relative to present coastal extents of the basin within the continental United States.

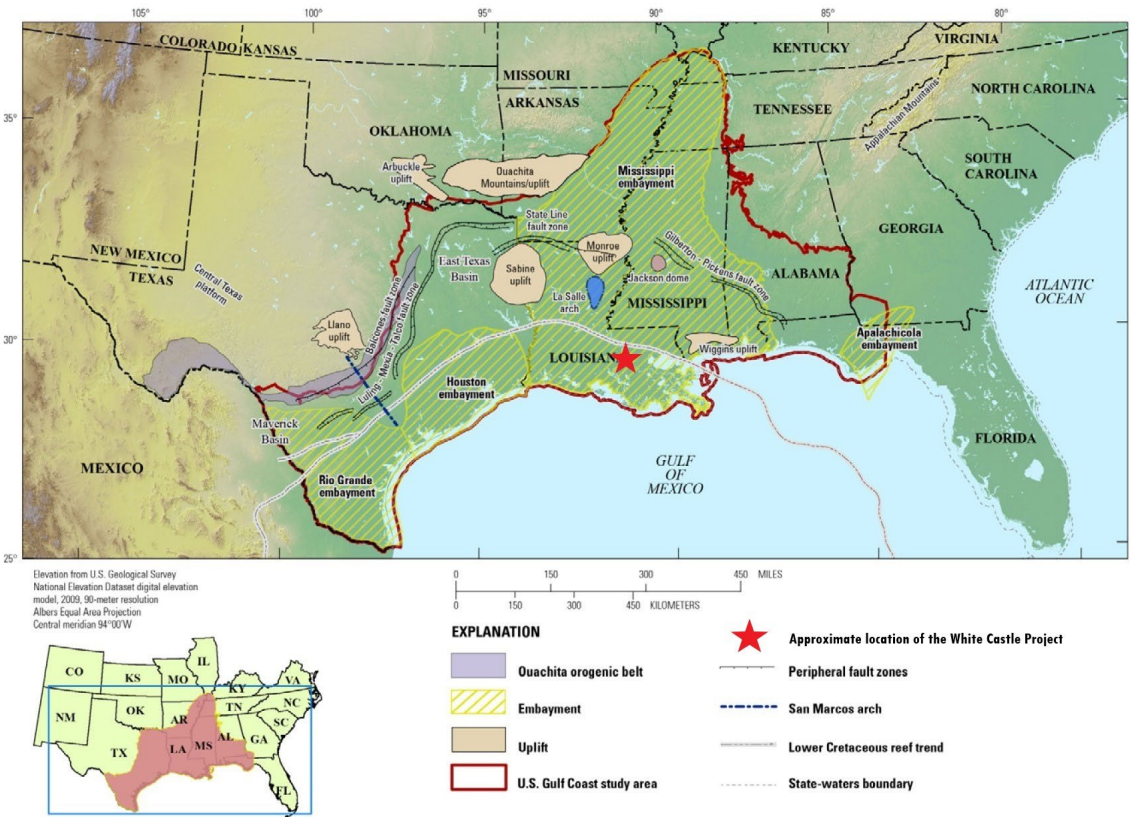

Figure 1-1 – Regional Gulf of Mexico Locator Map (Roberts-Ashby et al., 2012)

The Gulf of Mexico basin was formed by crustal extension and sea-floor spreading associated with the separation of the North American plate and Yucatan block during the Mesozoic breakup of Pangaea. Rifting initiated during the Middle Jurassic stretched and attenuated the underlying continental crust for approximately 25 million years. The deformation resulted in variable thickness of transitional crusts underlying the basin that contributed to later development of regional arches, embayments, and salt domes in the northern portion of the basin (Galloway W. E., 2008).

As the structural impression of the Gulf of Mexico formed, sediment began to accumulate in the young basin. Initial sedimentation occurred during the Late Triassic to Early Jurassic periods and was characterized by deposition of deltaic sandstones, siltstones, shales, conglomerates, and non-marine red beds of the Eagle Mills formation (Galloway W. E., 2008). During the Middle to Late Jurassic, the Yucatan block continued to drift southward away from the North American plate, resulting in a narrow connection between the Gulf of Mexico and Atlantic Ocean. The shallow hypersaline environment and communication with the Atlantic allowed for widespread deposition of a thick anhydrite and salt sequence, collectively called the Louann Salt (Galloway W. E., 2008). The Louann Salt contains up to 4 kilometers (km) of continuous salt section deposited over sediments of the Eagle Mills formation. Where that formation was absent, deposition occurred directly over pre-Cambrian igneous basement rock (Galloway W. E., 2008). Subsequent fill of the Gulf of Mexico basin resulted in a thick succession of clastics, carbonates, salts, and evaporites deposited in a highly cyclic depositional environment that was subject to sediment supply fluctuations and frequent sea level change (Galloway W. E., 2008; Roberts-Ashby, et al., 2012). These strata are Late Jurassic to Holocene in age, with total sediment accumulation reaching up to 20 km near the basin depocenter in southern Louisiana (Galloway W. E., 2008).

The structural opening of the Gulf of Mexico basin was also accompanied by northwest-to-southeast-trending transfer faults that influenced distribution of the Louann Salt and basin subsidence rates. Basement structures associated with the Ouachita range, Appalachian range, and Llano uplift contributed to Louann Salt placement and affected subsequent sediment distributions. Regional salt tectonics were also influenced by structural flexures such as the Balcones, Luling-Mexia-Talco, State Line, and Pickins-Gilberton fault zones (Galloway W. E., 2008). The current landscape of the Gulf of Mexico basin is primarily influenced by sediment loading and salt mobilization. These processes are typically expressed by structures such as growth faults, allochthonous salt bodies, salt welds, salt-based detachment faults, salt diapirs, and basin-floor compressional fold belts (Galloway W. E., 2008).

The White Castle Project is located in a tectonic salt province [redacted] further detail of the [redacted] production is discussed in *Section 1.9 – Site Evaluation of Mineral Resources*. Radial faulting associated with the offset domes has

been evaluated through 3D seismic surveys incorporated into structural mapping and modeling of the White Castle Project.

Figure 1-2(A) identifies the approximate location of the proposed White Castle Project site relative to the north-south seismic line (Peel, Travis, & Hossack, 1995). The present structural setting of the Gulf of Mexico basin, displayed in Figure 1-2(B), has a regional, dip-oriented seismic line conducted near the proposed White Castle site.

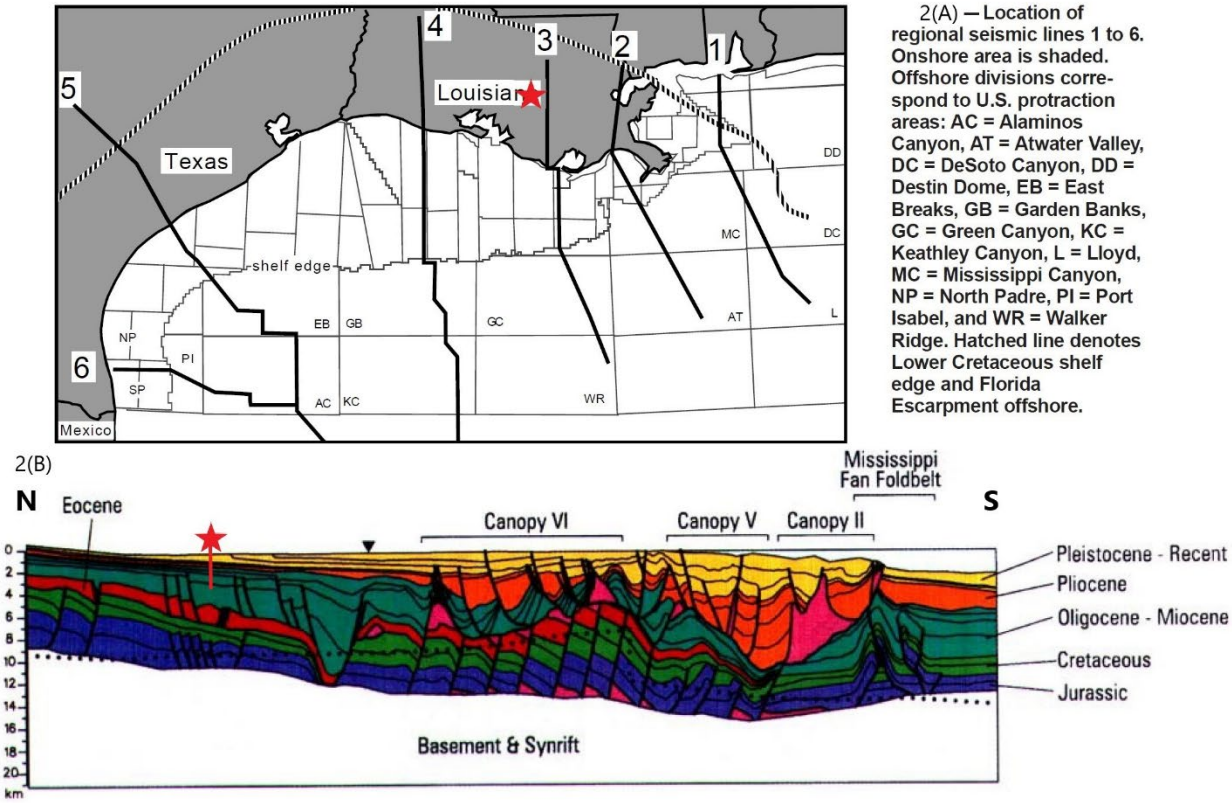

Figure 1-2 – Locator map and regional seismic line 3 (modified from Peel et al., 1995). The red star represents the approximate location of the White Castle Project.

The proposed injection interval of the White Castle sequestration site consists of Miocene sands encased within fine-grained Miocene shales that will provide regional upper and lower confinement to the injection interval (Figure 1-3). Stratigraphically, the proposed gross interval overlies the Lower Miocene depositional episode and underlies the Pliocene Citronelle Group.

Miocene strata of the Louisiana Gulf Coast represent a series of three fluvio-deltaic depositional episodes interrupted by first- and second-order marine transgressions. The section is primarily composed of terrigenous clastic sediments deposited during periods of rapid subsidence and abundant deposition. Sediments associated with regressive cycles represent Miocene reservoirs and are typically expressed in the geologic section by an increased presence of deltaic sands, silts, and clays. Periods of transgressive coastal onlaps are represented by marine transgressive shales that mark the division of Miocene strata into three stratigraphic units: the Lower, Middle, and

Upper Miocene. Index fossils associated with the Miocene section breaks, listed from oldest to youngest, include [redacted] (Hulsey, 2016; Galloway W. E., 2008). These benthic faunal markers are associated with first-order maximum flooding surfaces that correspond to global eustatic highs and are interpreted by the U.S. Geological Survey (USGS) to "serve as fine-grained sealing units" (Roberts-Ashby, et al., 2012).

Figure 1-3 illustrates the regional stratigraphic column as expected to be encountered at the proposed White Castle storage site and highlights the major stratigraphic intervals of this study. In the figure, individual Miocene units are plotted relative to key biostratigraphic markers and a coastal-onlap curve, to provide context to regional transgressive flooding surfaces. The [redacted] biomarker corresponds to the lower confining transgressive sequence, the [redacted] biomarkers correspond to the upper confining transgressive sequence, and the [redacted] biomarker corresponds to the Upper Miocene [redacted] formation. For the purposes of this permit application, the proposed injection interval includes Miocene strata from the Lentic Jeff biostratigraphic marker to the first appearance of the [redacted] biomarker. This gross geologic section contains both shale and sand intervals; however, only clean, sandy intervals with reservoir potential were modeled to sequester CO_2.

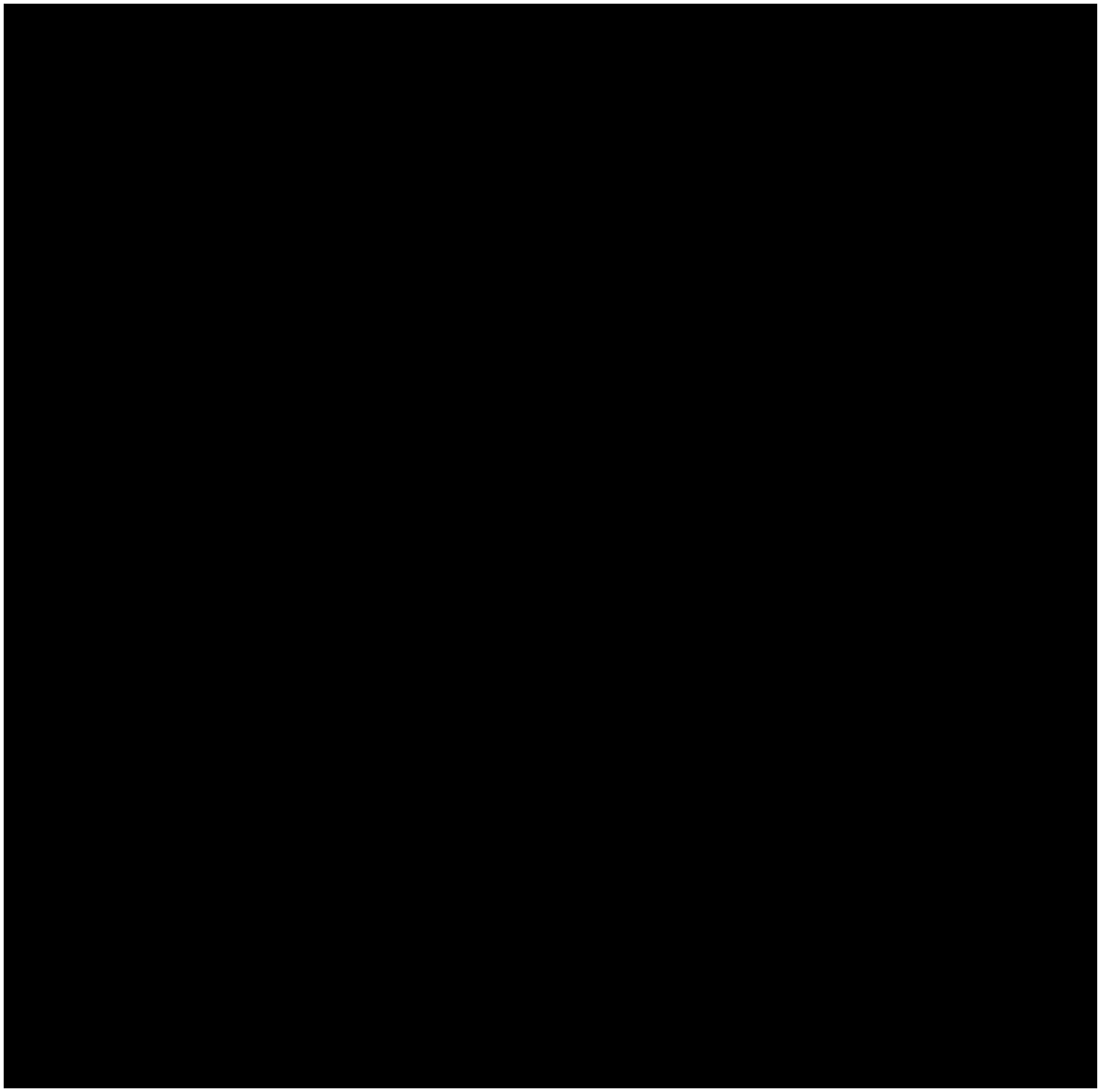

Figure 1-3 – Stratigraphic column of Miocene section with detailed coastal-onlap curve and key benthic foraminiferal biomarkers (Treviño & Rhatigan, 2017).

Lower Confining Zone:

The Lower Miocene shale is a regionally extensive shale deposited conformably on top of Miocene-aged sediments during a period of second-order marine transgression. Regional mapping performed around the White Castle Project indicates that the shale correlates with the index fossil associated with a Lower Miocene maximum flooding surface (Figure 1-3). Maximum flooding surfaces tend to be represented by periods of regional transgression associated with increased seal levels, eustatic highs, and the deposition of regionally extensive fine-grained to silt-sized clay minerals. These shales tend to be fine-grained and function as regional sealing units between episodes of regressive deposition (Roberts-Ashby, et al., 2012).

Injection Zone: *Miocene Sandstones*

Miocene sandstones near the White Castle sequestration site are generally described as fluvial-dominated deltaic deposits, dipping gently to the southeast where they thicken and increase in age basinward (Roberts-Ashby, et al., 2012). Sediments derived primarily from Appalachian and Cumberland Plateau uplands were delivered to southeastern Louisiana via the ancestral Mississippi and Tennessee Rivers. Deposition took place on the continental slope where sediments were subsequently reworked by mass-wasting and shallow marine regression (Galloway, Ganey-Curry, Li, & Buffler, 2000; Hulsey, 2016). Following Oligocene time, sediment influx began to slow along the western portion of the basin and accelerate along the eastern portion. This resulted in minimal Miocene progradation of the south Texas continental shelf, while the Louisiana continental shelf margin accumulated enough sediment to prograde basinward more than 160 km (Galloway, Ganey-Curry, Li, & Buffler, 2000; Roberts-Ashby, et al., 2012). Sandstones contained within the three Miocene stratigraphic units are lithologically similar, described as poorly consolidated to consolidated sandstones sourced from the ancestral Mississippi River. A more detailed stratigraphic review of Gulf Coast Miocene strata can be referenced in Galloway (either 2000 or 2008).

In 2012, the USGS analyzed regional Neogene reservoir porosity and permeability data measured by Nehring Associates, Inc. (2010). The data included 432 petroleum-reservoir-averaged porosity measurements and 259 petroleum-reservoir-averaged permeability measurements, which were leveraged to characterize average porosity and permeability of the Miocene storage assessment unit (SAU). The USGS reported that Miocene sands generally contain an average porosity of approximately 28% (±4%) and an average permeability of approximately 500 millidarcy (mD) (Roberts-Ashby, et al., 2012). The Miocene section is anticipated to be present between 3,000' and 12,000' below surface, near the proposed White Castle sequestration site.

Middle Miocene

Sandstones affiliated with the Middle Miocene 3 mega annum (Ma) depositional episode prograde the continental margin as much as 70 km and are bound between the underlying [redacted] shale and the overlying [redacted] shale (Galloway W. E., 2008). The USGS performed regional mapping that suggests that the gross Middle Miocene section averages 3,200' (±900') with an average net sand thickness of 480' (±140') (Roberts-Ashby, et al., 2012).

Upper Miocene

Sandstones affiliated with the Upper Miocene 6 Ma depositional episode extend across the approximately 40-90 km and are bound between the underlying [redacted] shale and the overlying [redacted] shale (Galloway W. E., 2008). The USGS regional mapping suggests the gross Upper Miocene section averages 5,400' (±1,000') with an average net sand thickness of 1,500' (±400') (Roberts-Ashby, et al., 2012).

Lower Miocene

Sandstones affiliated with the Lower Miocene 8 Ma depositional episode prograde the continental margin 65-80 km and are bound between the underlying Oligocene Anahuac shale

and the overlying [redacted] shale (Galloway W. , 2008). Regional mapping performed by the USGS suggest the gross Lower Miocene section averages 3,100 ± 800 feet with an average net sand thickness of 1,150 ± 500 feet (Roberts-Ashby, et al., 2012).

Upper Confining Zone: *Upper Miocene [redacted] Shale*

The Upper Miocene depositional episode was terminated by a regional marine flooding event associated with the first occurrence of benthic foraminifer [redacted], depending on which biostratigraphic marker was present (Galloway, Ganey-Curry, Li, & Buffler, 2000). The [redacted] shale represents a retrogradational package characterized by increased sea levels, eustatic highs, and the deposition of regionally extensive, fine-grained to silt-sized clay minerals. Transgressive shales such as the [redacted] tend to be fine-grained and function as regional sealing units between episodes of regressive deposition (Roberts-Ashby, et al., 2012).

1.3 Site Geology

[redacted]

Upon issuance of the Class VI Order to Construct, data will be gathered during drilling of the proposed well to update the data obtained via research with site-specific information. Table 1-1 (page 13) lists open-hole wireline logs planned during the drilling, with top and base depths designed to provide specific data pertinent to the site characterization application. If necessary, the proposed top and base of each investigative procedure will be subject to minor depth changes during the drilling, to analyze the objective formations. During drilling, coring operations are planned to obtain mineralogic, petrophysical, mechanical, and geochemical data to further refine this site characterization. Anticipated depths to the injection and confining intervals of the proposed well are listed in Table 1-2.

General mineralogy and reservoir characteristics are described regionally first, from pooled studies. If available, offset core and cuttings data from published research will be included. Finally, analyses of offset wellbores are compiled to represent the proposed well site characteristics. Wireline logs, petrophysical analyses, and production data from wellbores adjacent to the proposed well were also studied to calculate anticipated conditions at the site.

Additionally, a stratigraphic test well is planned to be drilled prior to the issuance of the Class VI permit and used to collect the same data mentioned above, which will then be used to update previous models. This well will be strategically placed updip of the proposed injection well, [redacted].

[redacted] The stratigraphic column in Figure 1-5 corresponds to depths in this well. Table 1-3 (page 15) displays the formation tops

and depths to the upper confining zone, injection zone, and lower confining zone as logged in the well.

Figure 1-4 – Project Overview Map

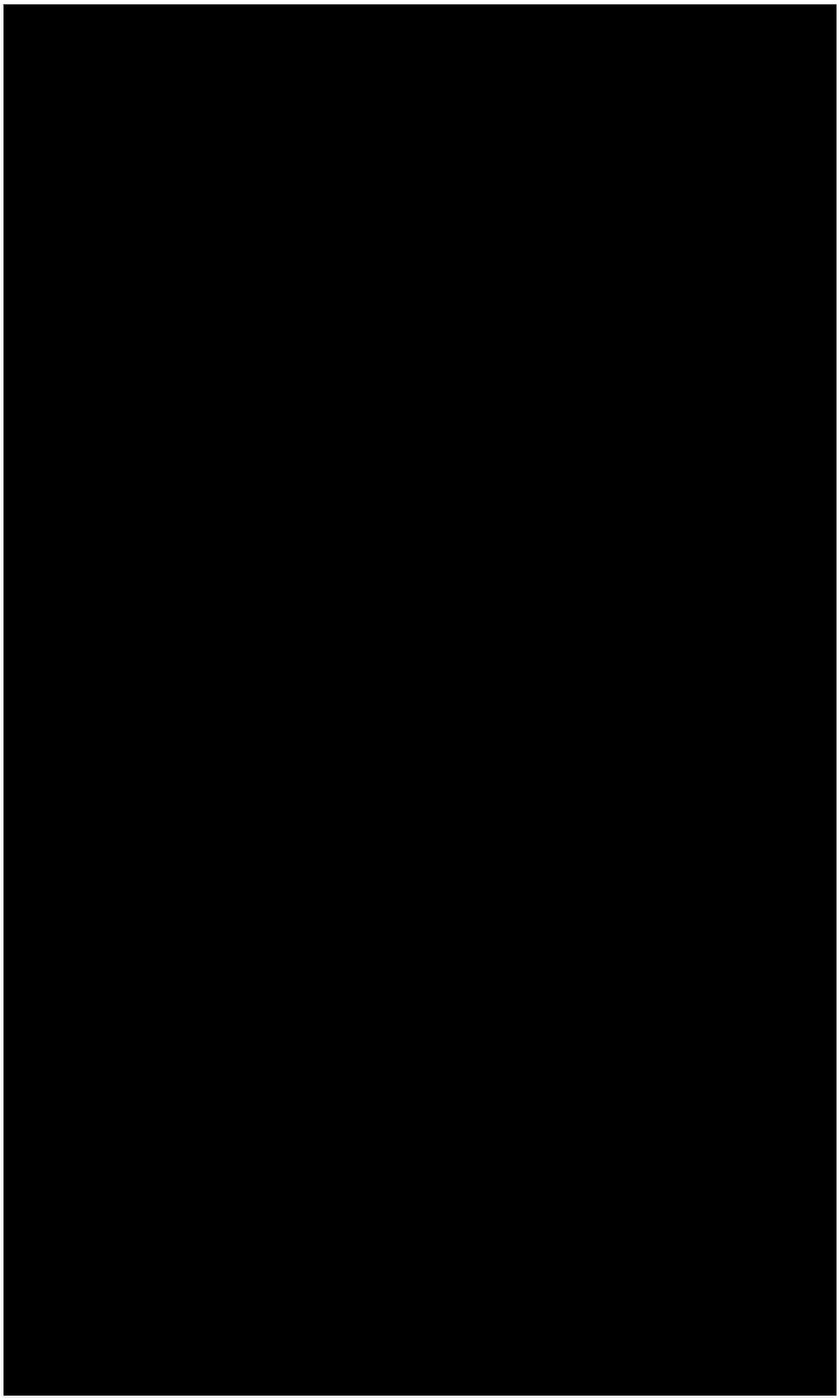

Figure 1-5 – Stratigraphic Column from SN [redacted]

Table 1-1 – Planned Geophysical-Wireline Logged Intervals

Geophysical Log Suite	Log Interval Top (ft)	Log Interval Bottom (ft)	Use
[redacted]			

Table 1-2 – Cored Intervals Planned Within Anticipated Formations – WC IW-B No. 002

Approximate Core Depth Intervals (t S)	Core Type	Number of Cores	Predominate Lithology	Formation/Zone
[redacted]				

*TVDSS – true vertical depth subsea

**200’ interval depths approximated in formations where 30’, 60’, or 90’ core barrels may be selected with the aid of near bit gamma ray during drilling.

Table 1-3 – Injection and Confining Zones as Encountered in Well SN [redacted]

System	Group/ Formation Name	Injection/ Confining Zone	Formation Top – Formation Bottom (ft)	Thickness (ft)
Miocene	[redacted]	Upper Confining	[redacted]	[redacted]
Miocene	[redacted]	Injection Interval	[redacted]	[redacted]
Miocene	[redacted]	Lower Confining	[redacted]	[redacted]

1.3.1 Injection Zone

The injection zone is comprised of the lower Upper Miocene, Middle Miocene, and the Lower Miocene sands, which include maximum flooding surfaces [redacted]. Figure 1-6 (page 18) depicts these maximum flooding surfaces.

Upper Miocene deposition at the White Castle location was dominated by the Mississippi–Tennessee Delta System, which was "alluvial apron, with sediments largely derived from a rejuvenated continental interior, the Nashville Dome, and southern Appalachian uplands" (Wu, 2002). The only Upper Miocene sands included in the injection interval are those in the [redacted] sand, a [redacted] equivalent. The [redacted] sand is bounded below by the maximum flooding surface of the [redacted], which marks the beginning of the Middle Miocene. This section contains blocky sands, which represent an extensive reworking of sediments in a high-energy depositional setting commonly associated with deltas or near-shore zone deposits (Nwagwu, Emujakporue, Ugwu, & Oghonya, 2019).

Middle Miocene is defined by "two widespread transgressive deposits associated with the faunal tops [redacted]" (Combellas-Bigott & Galloway, 2005). The Middle Miocene, similar to the Upper Miocene, received the bulk of the sediments from the Mississippi and Tennessee delta systems, with "salt-related structural provinces controlling the location and configuration of the depocenters" (Combellas-Bigott & Galloway, 2005). Depositional settings within the Middle Miocene are broken down into four different genetic cycles, differentiated by major maximum flooding surfaces. The details of these genetic cycles and associated maximum flooding surfaces are provided in Figure 1-7 (page 19).

Figure 1-8 (page 20) depicts the depositional environment maps for each cycle. Cycle 1 is represented by image A, cycle 2 by image B, cycle 3 by image C, and cycle 4 by image D. The primary depositional environments reflect varying deltaic style. Cycle 1 represents a progradational to aggradational delta-lobe complex; cycle 2 is characterized by minor aggradational to progradational delta-lobe complex; cycle 3 is characterized as delta-flank facies; and cycle 4 reverted back to the progradational to aggradational delta-lobe complex.

The [redacted] is characterized as a regional transgressive marine shale that is the lower bound of the Middle Miocene and upper bound of the Lower Miocene (William E. Galloway, 2000). Bureau of Economic Geology (BEG) studies identified the [redacted] as one of the most "significant" confining zones for CO_2 injection, due to the lateral extensive presence and sealant nature (Treviño & Rhatigan, 2017). Episodes of "sandstone-dominated deltaic and shore-zone progradation" were disrupted by the [redacted] transgression, which occurred towards the end of the "early Miocene and the beginning of the Middle Miocene" (Meckel & Trevino, 2014). The [redacted] intra-reservoir seal allows the total gross injection interval to be divided into upper and lower sections for targeted injection, utilizing an upper and lower injection wellbore, respectively.

During the early Miocene (Lower Miocene), deltaic progradation along the Mississippi delta was restored (William E. Galloway, 2000). The White Castle location falls on the eastern edge of the Mississippi Deltaic axis and is depicted as a fluvial-dominated delta as seen in Figure 1-9 (page 21). Similar to the environments in the Miocene sections above, similar stratigraphic sequences will be encountered throughout the injection interval.

Primary lithologies within the Miocene section are interbedded sandstones, siltstones, and shales with varying clay and calcite concentrations. Meckel and Trevino (2014) performed an analysis of the potential for carbon sequestration within the Miocene along the Gulf Coast. Core samples within the correlative injection zone were characterized as fine- to coarse-grained sandstones with interbedded mudstones and siltstones (Meckel & Trevino, 2014). Figure 1-10 (page 22) is a thin section from this study of fine-grained sandstone within the Miocene, depicting high porosity. This description corresponds with a sample log in an offset well (SN [redacted]) within the injection interval, with descriptions ranging from fine- to coarse-grained gray sandstones, with interbedded siltstones, shales, and clays (Watson, 1965).

Sand packages within the injection interval that contain optimal reservoir qualities will be targeted for injection, with the interbedded shales acting as individual seals within the interval. Further analysis was done on the lateral extents of these individual sands and shales by utilizing offset 3D seismic surveys to develop a geocellular model. The resulting model was implemented into the reservoir simulation to better illustrate sands that could potentially communicate within the injection interval. Further details of the geocellular model will be discussed in *Section 2 – Carbon Front Model*.

An open hole log from an offset well (SN [redacted]) depicting local stratigraphy is displayed in Figure 1-11 (page 23). A shale volume (Vshale) log was calculated from the spontaneous

potential (SP) curve to determine the clay content within the section. The Vshale curve is found in track 1 with a shading applied to depict the varying shale content. A deep resistivity curve is plotted in track 2. The injection interval occurs at the top of the [redacted] sand and encompasses all strata down to the [redacted]. The gross thickness of the injection zone depicted in Figure 1-11 is roughly [redacted]. *Appendix B-6* illustrates the gross injection interval isopach map for the area, while *Appendix B-2* represents the top of [redacted] structure map.

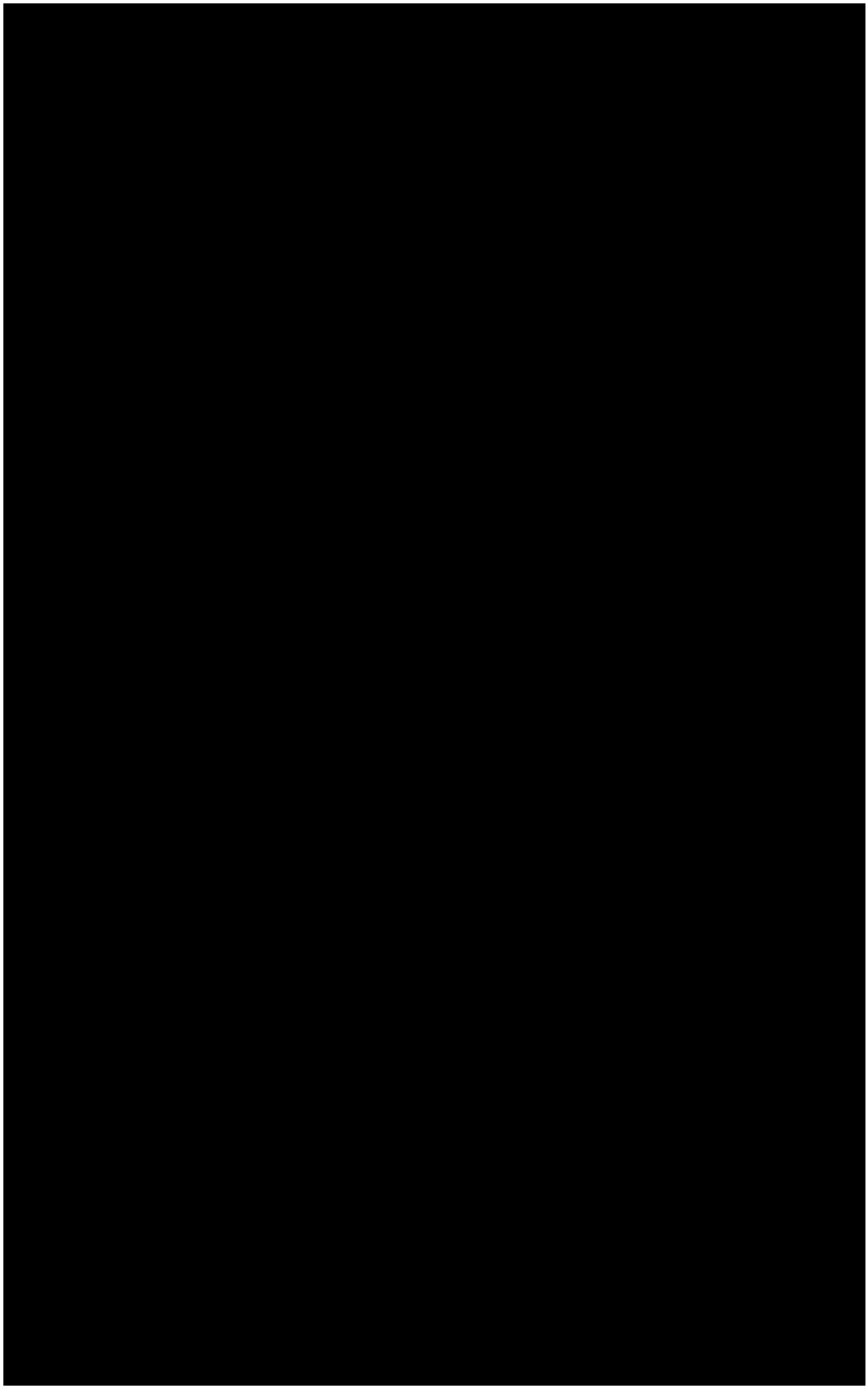

Figure 1-6 – Stratigraphic section of Miocene with injection interval indicated (Olariu, DeAngelo, Dunlap, & Treviño, 2019).

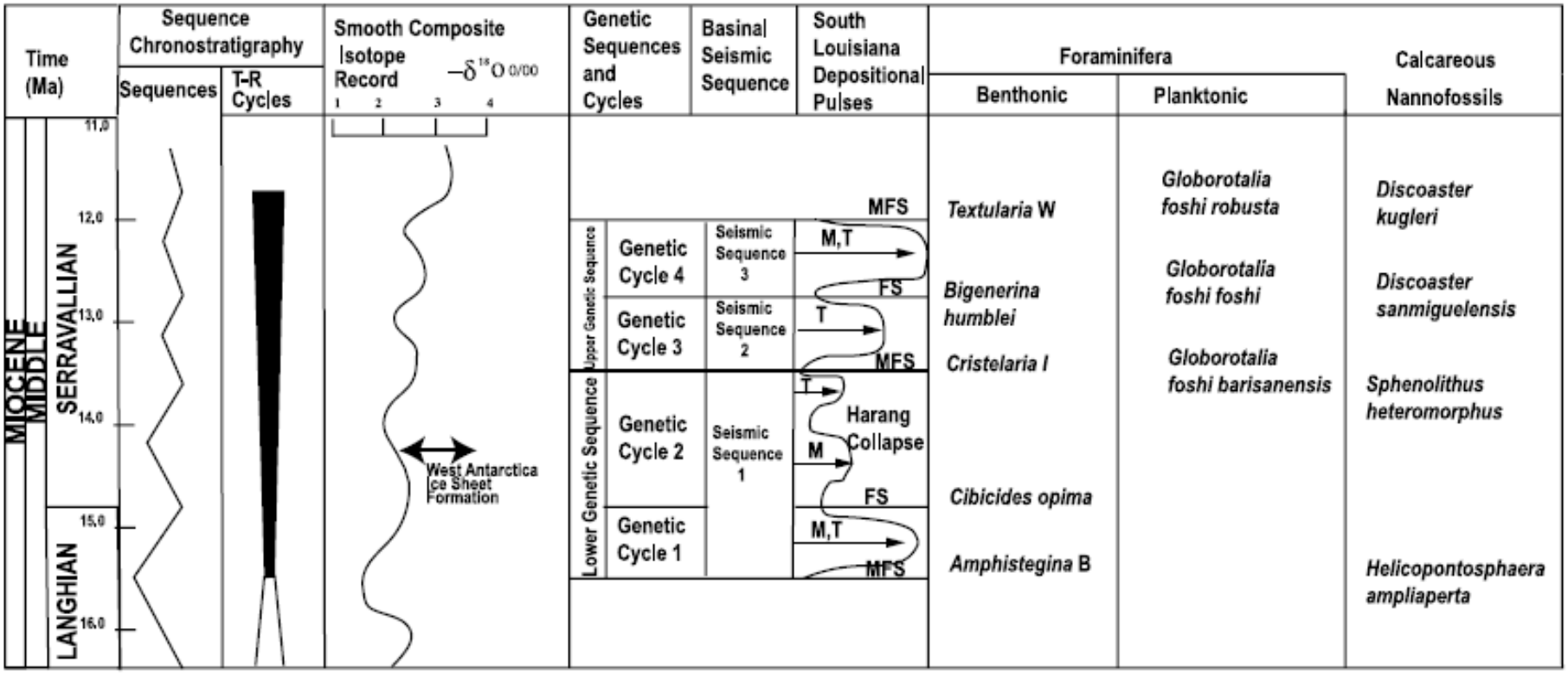

Figure 1-7 – Stratigraphic sequence with genetic cycles depicted (Combellas-Bigott & Galloway, 2005).

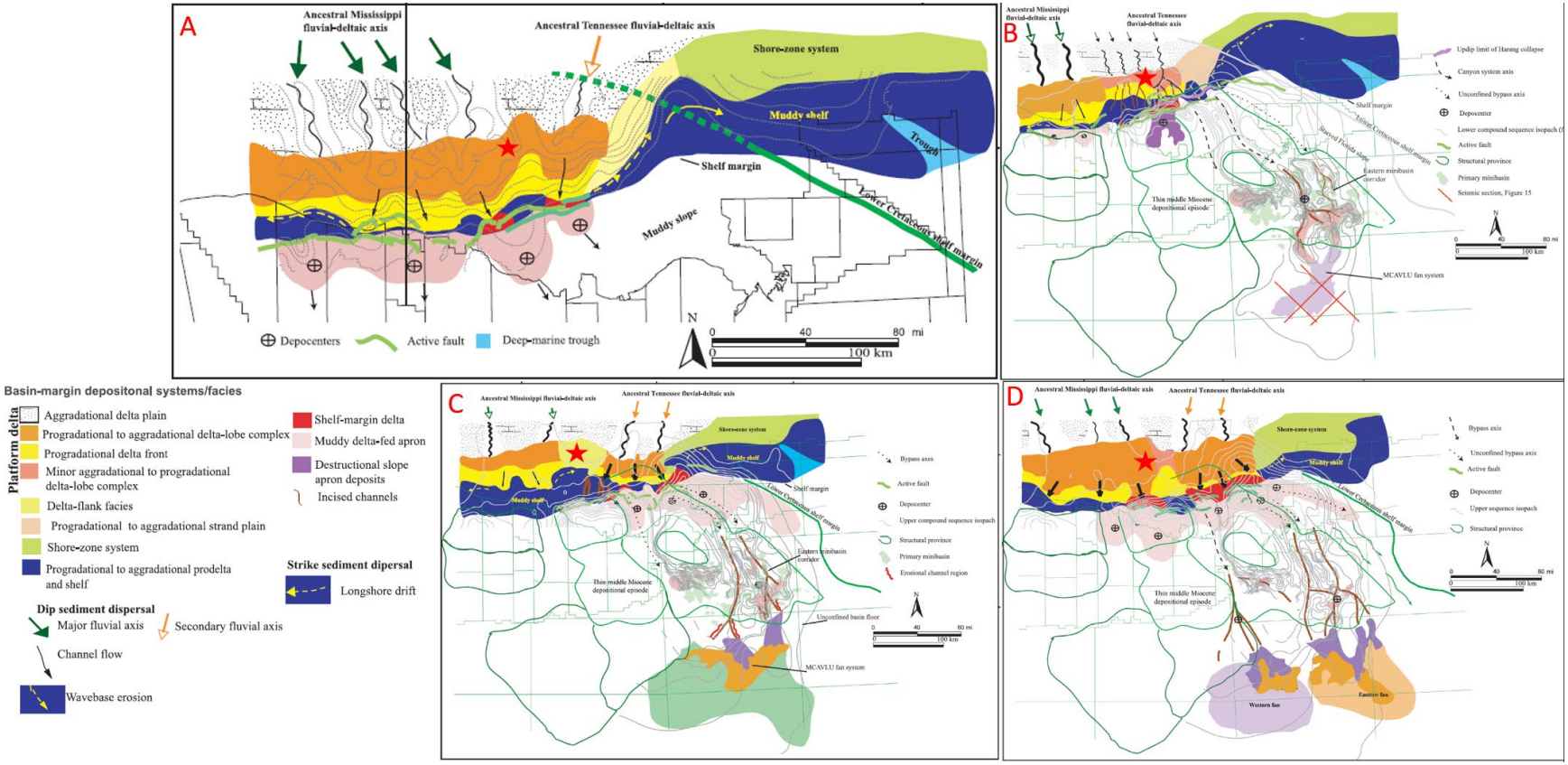

Figure 1-8 – Depositional environment maps of cycles 1–4 (A–D, respectively). The red star represents the White Castle location (Combellas-Bigott & Galloway, 2005).

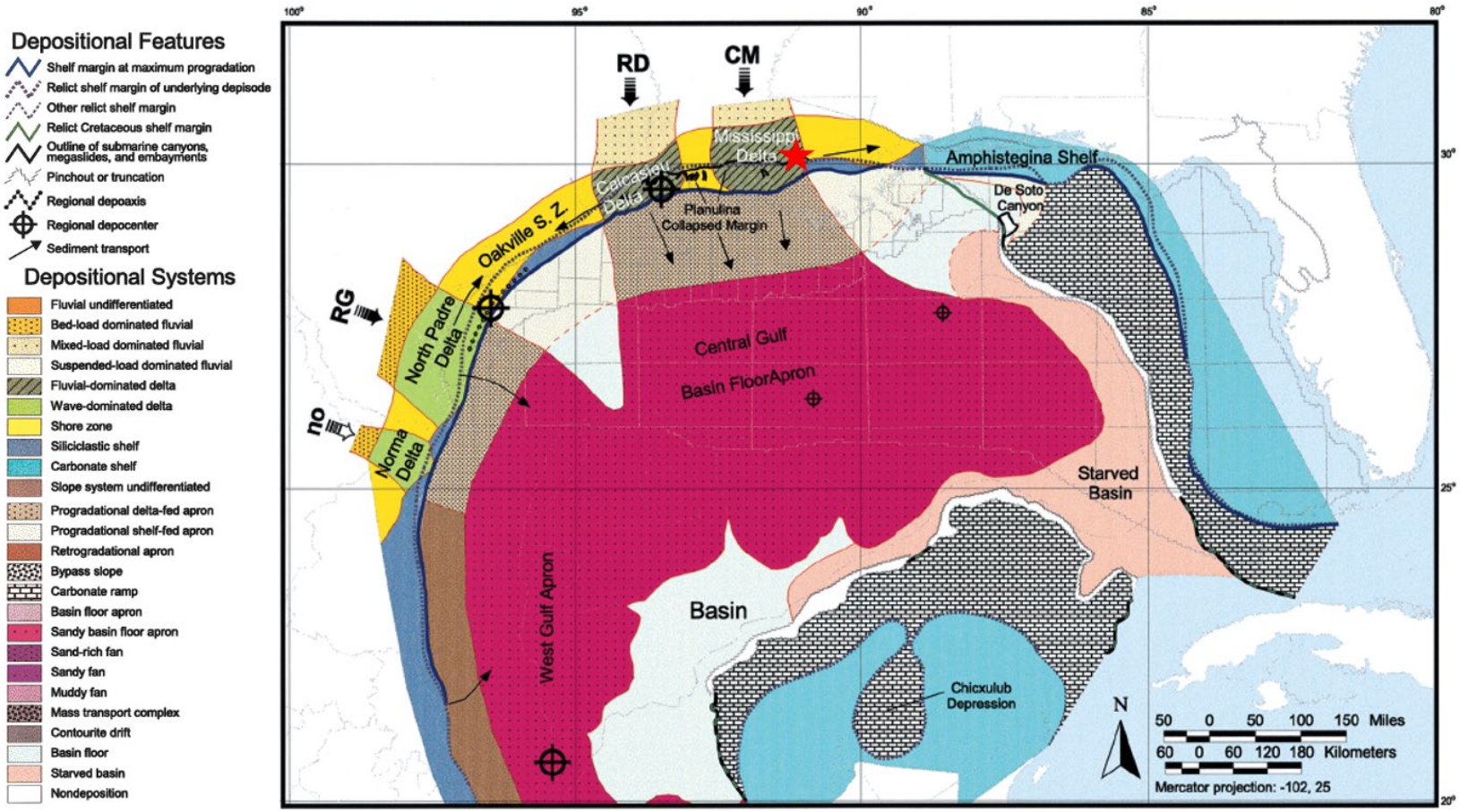

Figure 1-9 – Lower Miocene depositional systems map (Combellas-Bigott & Galloway, 2005).

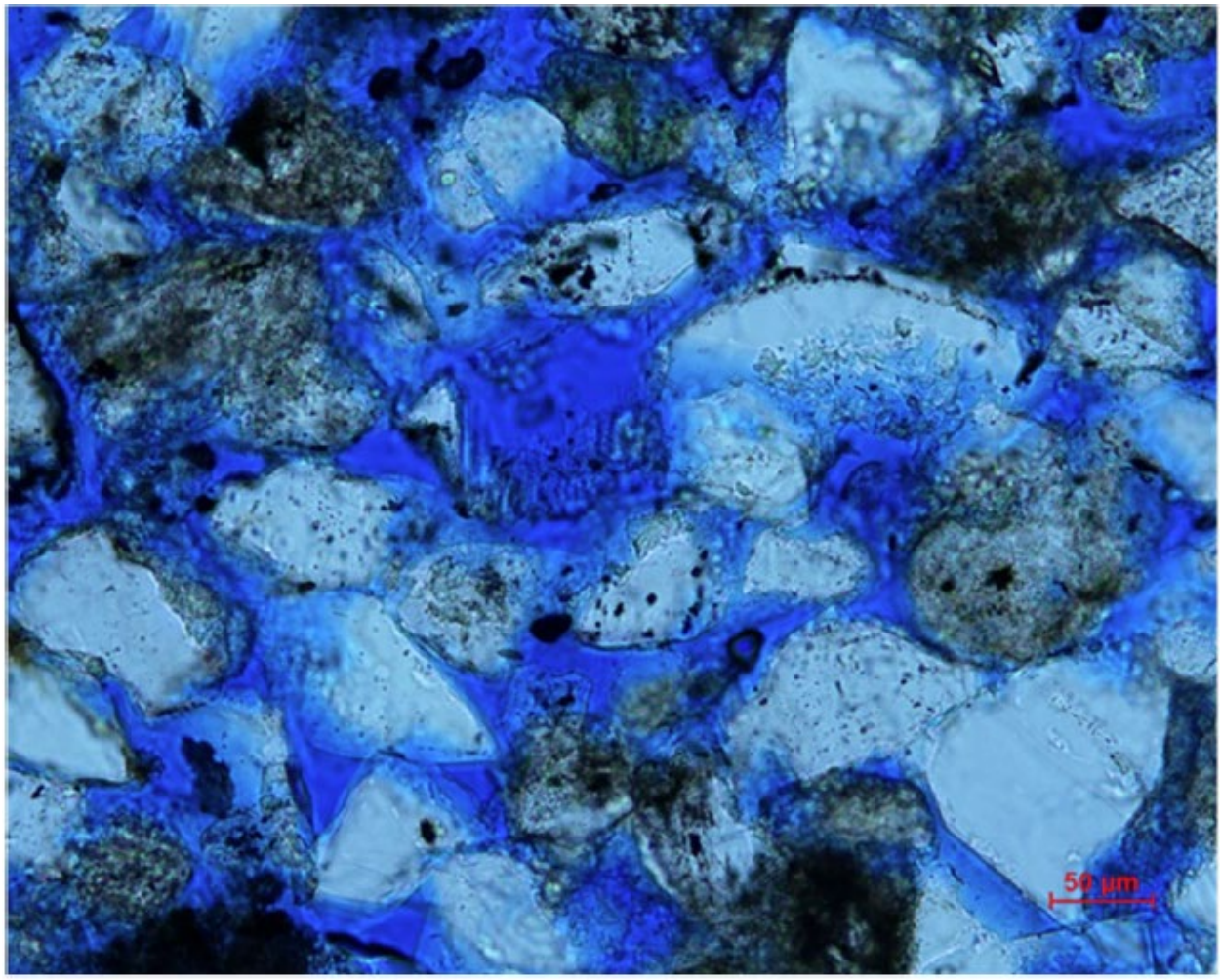

Figure 1-10 – Thin section image of fine-grained Miocene sandstone sample.
Blue is pore space and white is quartz grains with little calcite cementation present (Meckel & Trevino, 2014).

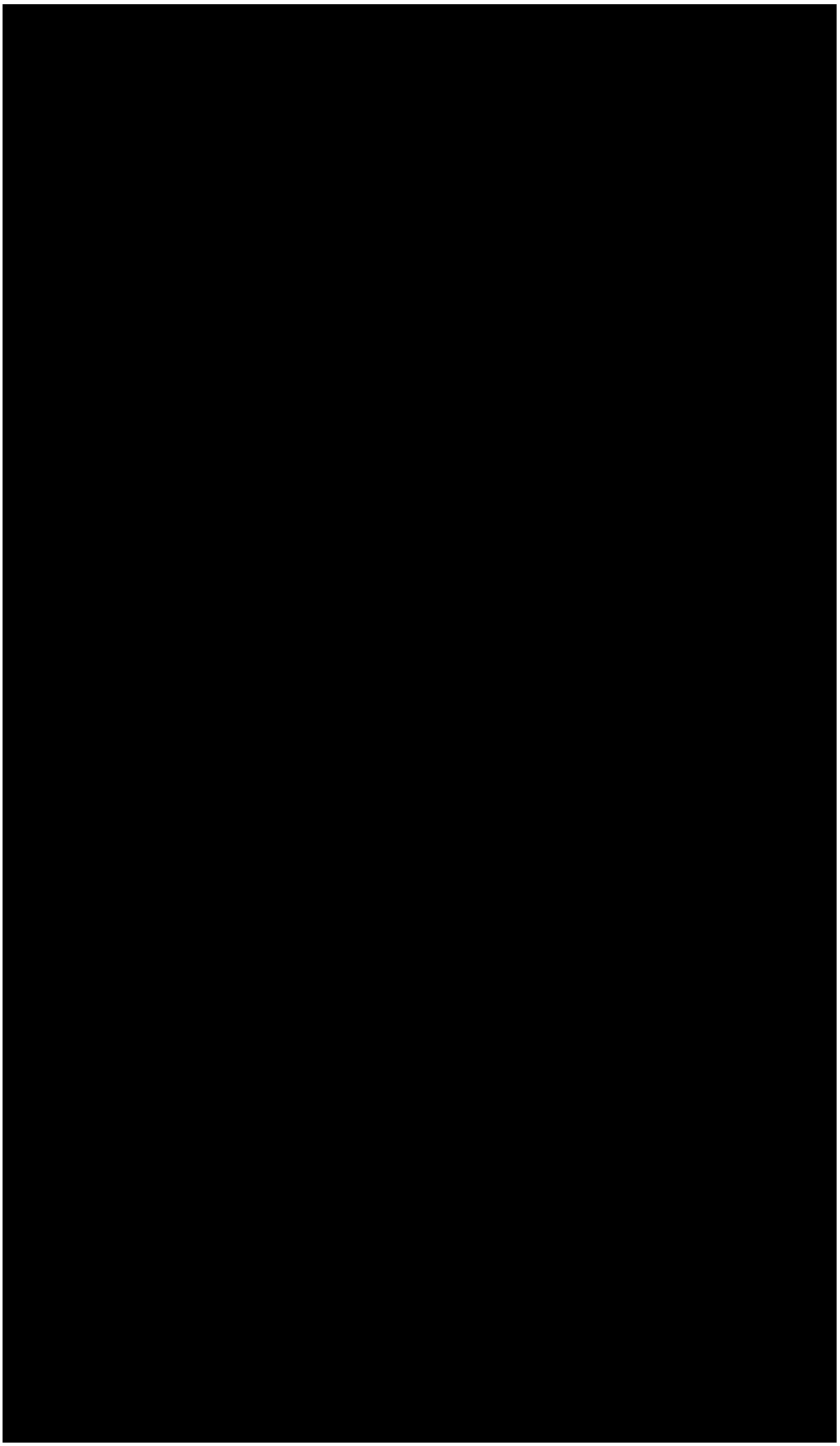

Figure 1-11 – Open-hole log of offset well SN [redacted] depicting the injection interval.

1.3.2 Upper Confining Zone

During the Upper Miocene period, sediment dispersal and paleogeography remained "relatively stable." A significant deposition event occurred, mainly focused on the Mississippi dispersal axes, following the [redacted] flooding event. This depositional episode came to an end when a regional flooding event related to either the [redacted] or, in certain basin areas without the [redacted], the slightly older [redacted] (William E. Galloway, 2000). Due to the difficulty in differentiating the [redacted] from the [redacted], the latter is utilized as the upper bounding Upper Miocene maximum flooding surface.

Figure 1-12 is a map of the paleogeography of the Upper Miocene with the WC IW-B No. 001 and No. 002 well locations. The proposed well locations fall within the Mississippi Delta System, near the shore zone. There are additional maximum flooding surfaces within the Upper Miocene, between the [redacted] and the [redacted], that include [redacted], but for the sake of this permit, the primary confining zone will be referred to as the [redacted].

Figure 1-13 (page 26) is a depiction of the upper confining zone from the offset well (SN [redacted]) as used above. A Vshale curve in track 1 illustrates the sand and shale distributions within the upper confining section. The methodology of calculating the Vshale curve is later discussed within the porosity and permeability sections (*1.5.1.1* and *1.5.1.2*, respectively). Figure 1-13 shows [redacted] net feet of rock with greater than 70% shale content based on the Vshale curve, which translates to a [redacted] shale volume within the [redacted]. These same calculations were made on five additional wells within 5 miles of the proposed White Castle location. The average results of all wells were [redacted] of net shale and [redacted] shale volume within the [redacted]. The wells used for these calculations are depicted in the map shown in Figure 1-14 (page 27).

The high shale content and multiple maximum-flooding events recorded between the [redacted] and the [redacted] provide ideal sealant properties between the injection zone and Underground Source of Drinking Water (USDW). This sealing nature is evidenced by the hydrocarbon production within the [redacted] formation, [redacted]. There, one well produced out of the [redacted] sand (SN [redacted]), which correlates to the top of the proposed injection interval. This production demonstrates not only the sealing capabilities of the overlying [redacted] formation in the area but also that hydrocarbons were contained.

Structural trends and gross thickness of the [redacted] can be seen in *Appendices B-1* and *B-4*, respectively. These depict the relationship of structural and depositional features within the area.

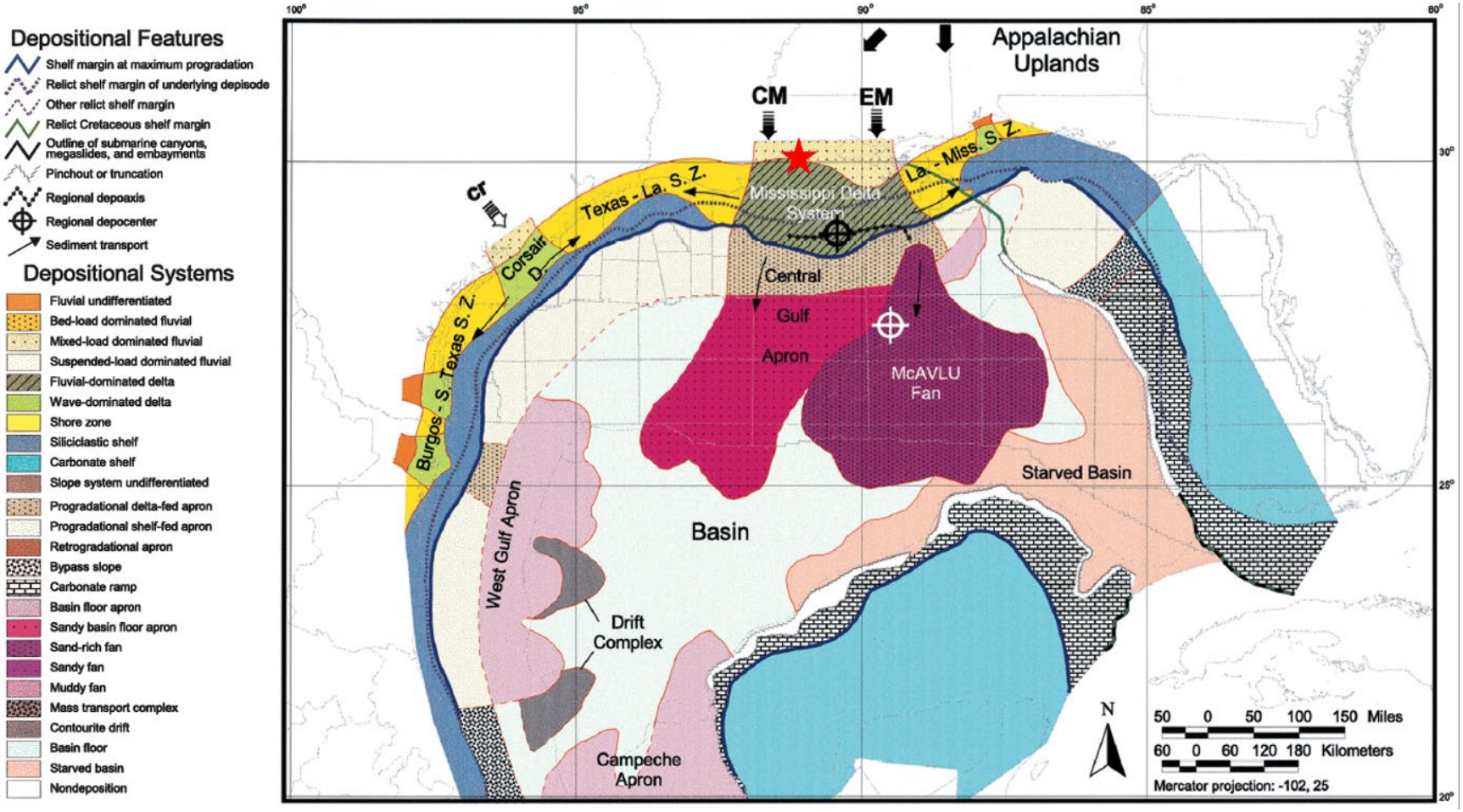

Figure 1-12 – Depositional Map of Upper Miocene (Combellas-Bigott & Galloway, 2005)

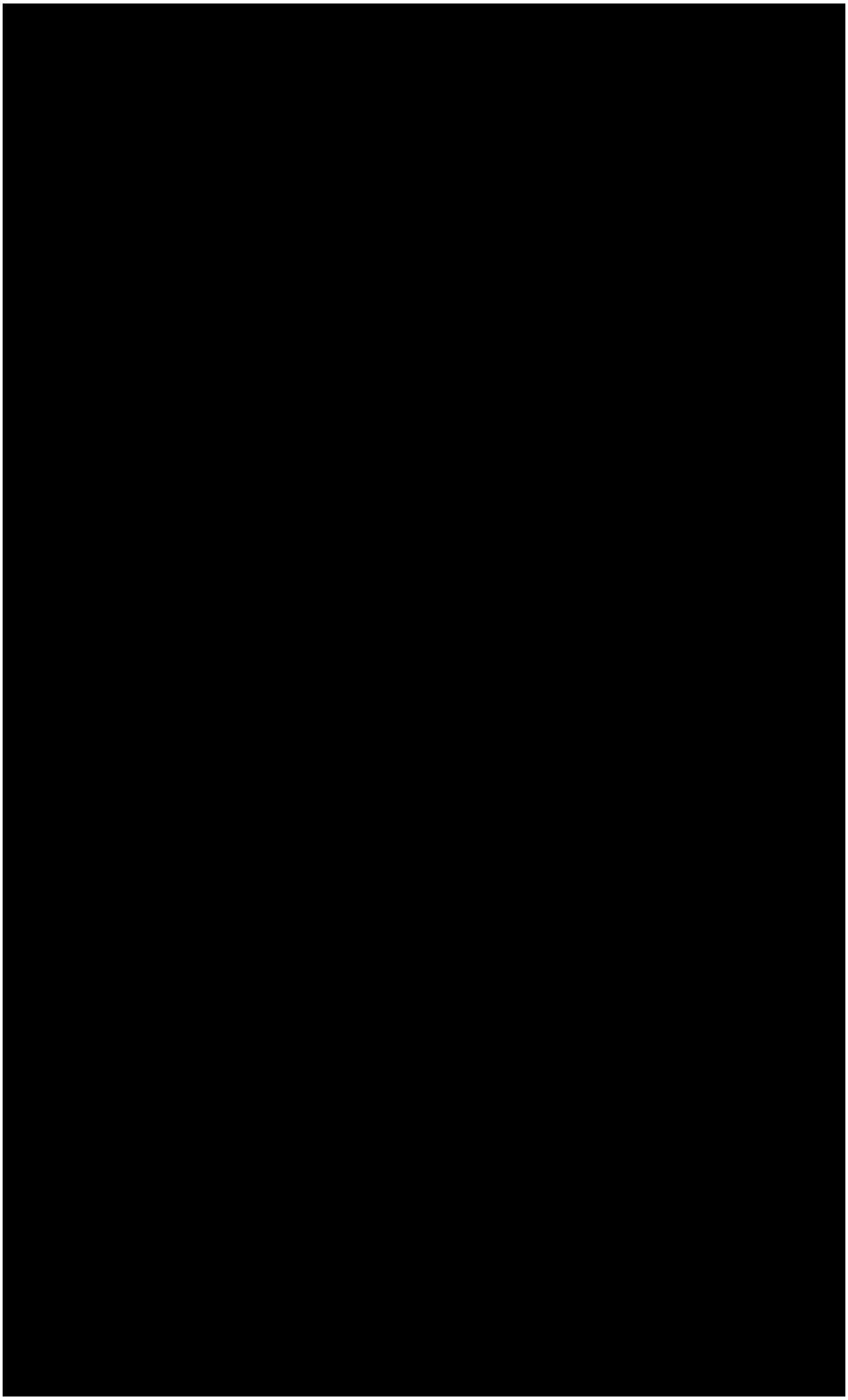

Figure 1-13 – Open-hole log of offset well SN [redacted] depicting the upper confining interval.

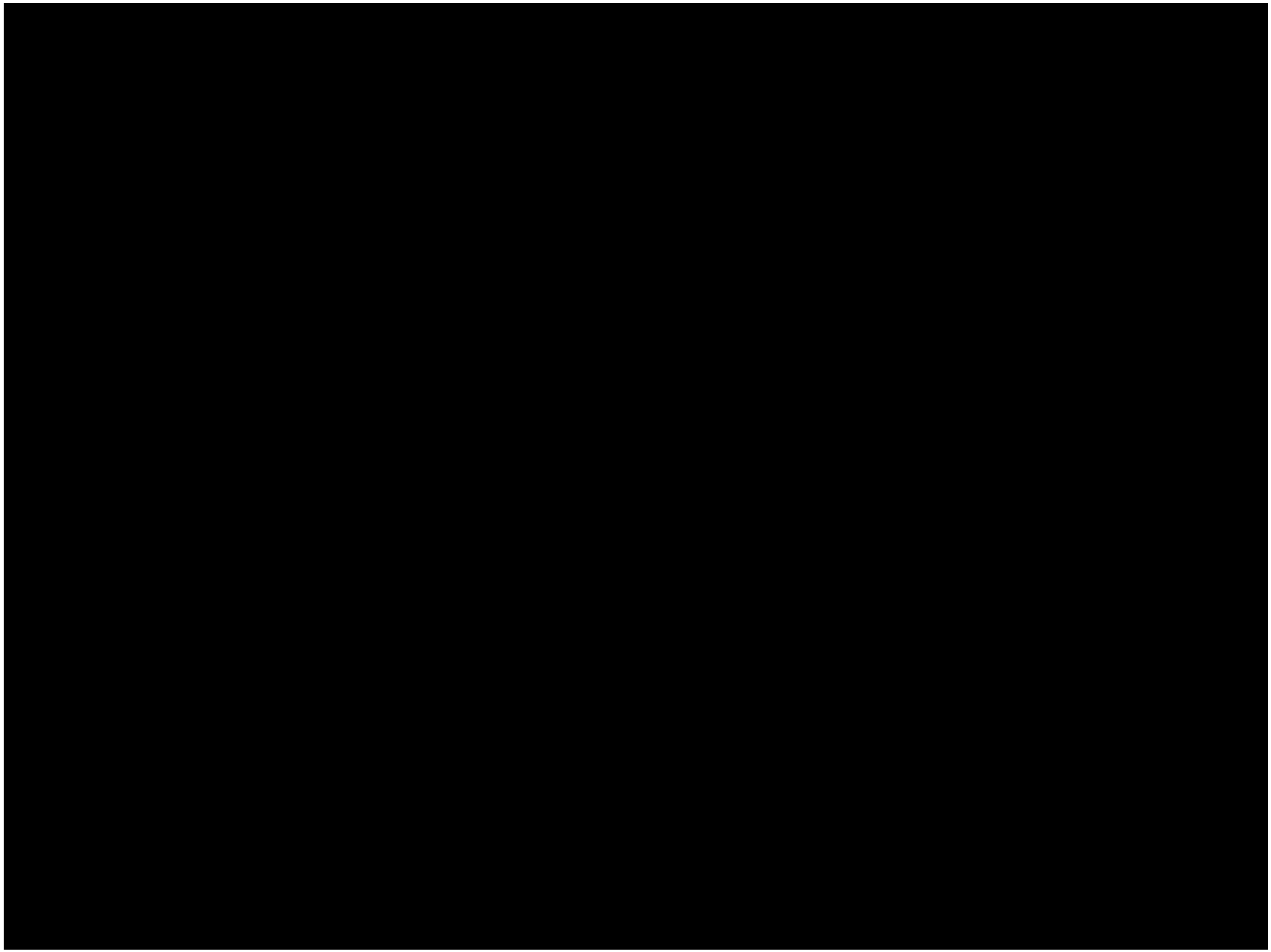

Figure 1-14 – Map of well control used to determine Vshale, porosity, and permeability distributions.

1.3.3 Lower Confining Zone

The early Miocene was a period of relative paleogeographic stability of the Gulf basin. Early Miocene sediment influx exhibited the first clear shift to the central Gulf fluvial axes that dominate the later Neogene. Uplift of the Edwards Plateau and adjacent inner coastal plain is reflected in the influx of reworked Cretaceous and older Cenozoic debris in the lower Miocene fluvial deposits (William E. Galloway, 2000). Figure 1-9 (*Section 1.3.1*) is a paleogeographic map of the Lower Miocene.

Within the Lower Miocene, the maximum flooding surface identified as the [redacted] will act as the lower confining unit. The [redacted] sequence was deposited during the Liebusella regression, which terminated the second-order late Oligocene Anahuac sequence. The [redacted] was deposited on a second-order relative sea level fall (Fillon & Lawless, 2000). Prior to regressive deposit of the [redacted] sand, a blanket marine shale was deposited as depicted in the regional cross sections within the area (Figure 1-17, *Section 1.3.4*).

Figure 1-15 is an open-hole log image of the lower confining interval represented in the offset well SN [redacted]. [redacted] As displayed in Figure 1-15, a thick marine shale sequence can be identified by the Vshale curve directly below the lowest most injection sand. This will act as an optimal lower confining seal for the proposed permitted injection interval. Graphs depicting the relationships between clay content and permeability/mercury injection pressure from the BEG study are displayed in Figure 1-16 (page 30). These relationships establish that higher clay contents within the interval increase the sealing capabilities of the [redacted]. This study concluded that the clay-rich Miocene mudrocks have sealing capability sufficient for potential CO_2 storage due to the clay-rich mudstone with smaller pore throats (Lu, Carr, Treviño, Rhatigan, & Fifariz, 2017).

The structural trends and overall thickness of the [redacted] are illustrated in *Appendices B-3* and *B-8*, respectively. These visuals showcase the correlation between structural characteristics and deposition patterns in the designated area.

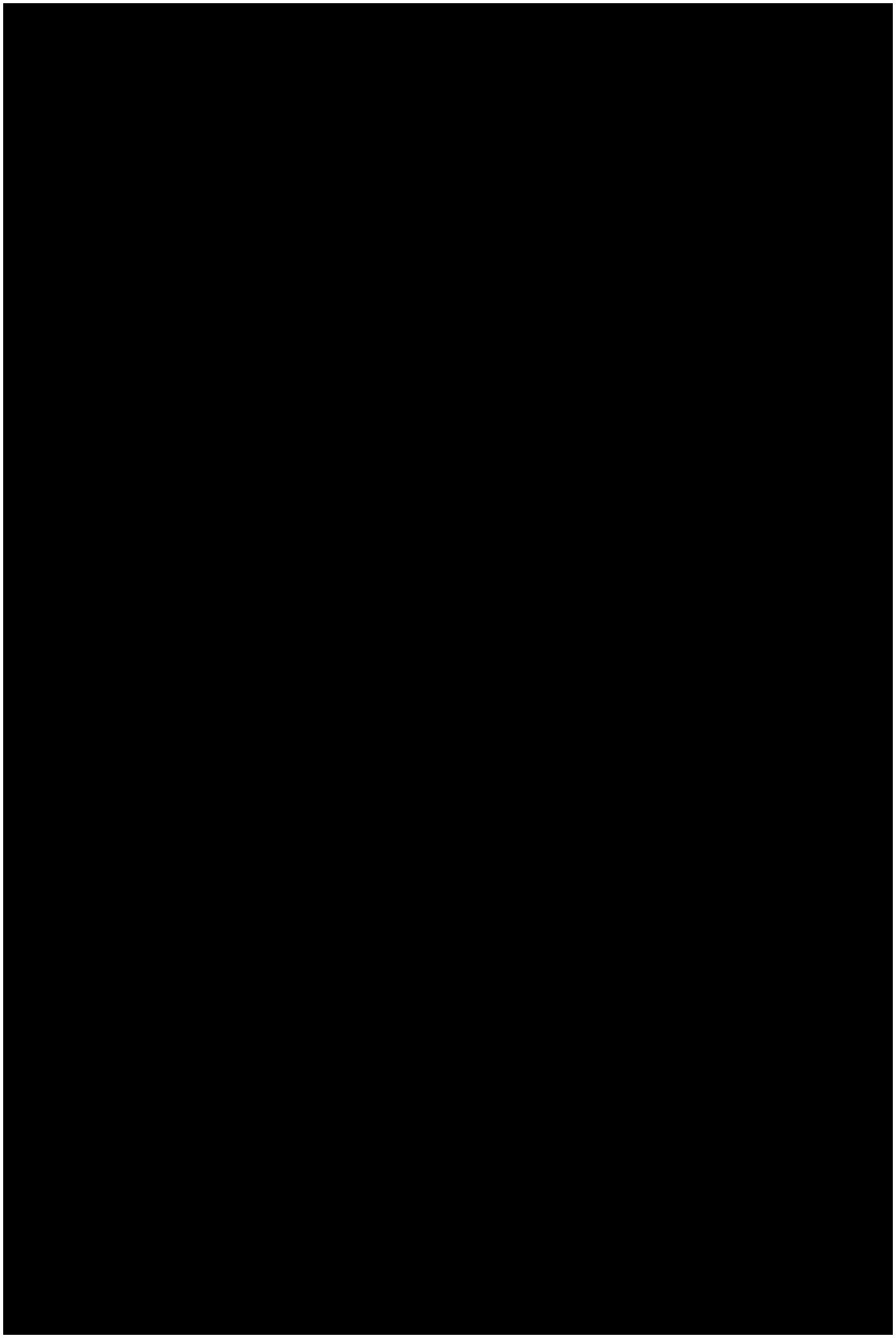

Figure 1-15 – Open-hole log of offset well SN [redacted] depicting the lower confining interval.

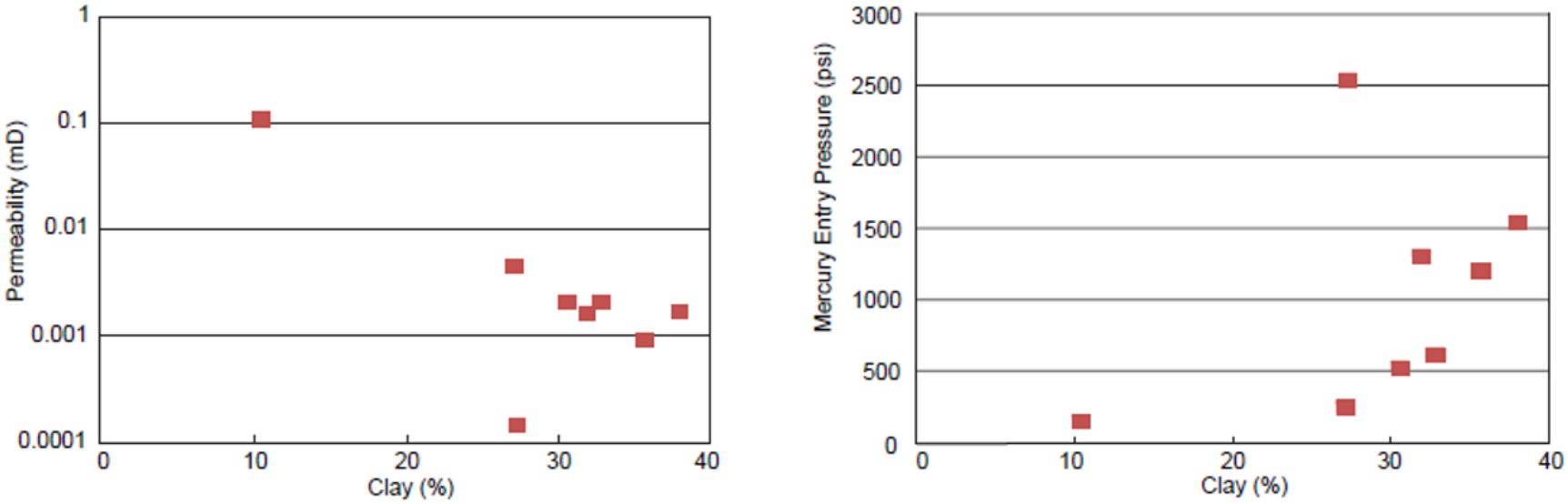

Figure 1-16 – Scatterplots showing higher clay content reflect lower perms and higher mercury entry pressure (Lu, Carr, Treviño, Rhatigan, & Fifariz, 2017).

1.3.4 Geologic Structure

Structural dip of sedimentary strata within the injection interval were mapped, utilizing well control and 3D seismic data. A full examination of well data available to the public was conducted over the AOI. To ensure data accuracy, the Louisiana Department of Natural Resources' (LDNR) SONRIS database, IHS, TGS, Enverus and GEOMAP were reviewed to locate surface and bottomhole positions for existing wells. Professional geologists and engineers double-checked by cross-referencing multiple databases and also obtained plats and scout cards for wells found only in some databases. The verified well data and locations were then imported into a geologic software with their associated well logs, if available. Sixty-nine wells and their associated logs were utilized for the subsurface control; 32 of these well logs were digitized and used to assist in tying in the seismic data. Tops were correlated across the region based on log responses and incorporated into the structural interpretation. These tops were sourced from offset field papers to assist in identifying paleo features. Figure 1-17 (*Appendix B-10*) represents a cross section displaying correlative maximum flooding surfaces used in the structural interpretation. Supplementary structural and stratigraphic cross sections, as well as a reference map, are provided in *Appendices B-9* through *B-12*.

Figure 1-17 – South-North Structural Cross Section

1.3.5 Reflection Seismic Profiles

Approximately 74 square miles of 3D surface seismic data ( ) were licensed by Harvest Bend CCS and included in this interpretation (Figure 1-18).

Figure 1-18 – Overview map of licensed seismic surveys.
The blue highlight represents and yellow highlight represents .

The (highlighted in blue) was acquired in 1996 and reprocessed using Pre-Stack Time Migration (PSTM) in 2013. The data was acquired using dynamite as the energy source, 75' x 75' bin size, and 16,670' maximum offset, resulting in (nominal) 32-fold data. The (highlighted in yellow) was acquired in 2002 and reprocessed using PSTM in 2008. The data was acquired using dynoseis as the energy source, 110' x 110' bin size, and a 12,320' x

39,380’ patch, resulting in (nominal) 36-fold data. The resulting 3D reflection profiles, which image the subsurface based on density and velocity contrasts, were combined with subsurface well control (geologic formation tops) to map the proposed injection and confining intervals. The resulting maps represent formation depths (Figures 1-19 and 1-20) and any discontinuities such as faulting. The 3D seismic volume was used to map a thick sequence of Miocene-aged rocks approximately 8,600’ thick. The seismic data is of good quality with sufficient offset information to image the target section (between [redacted] subsea depth). The 3D seismic data recorded and interpreted across the proposed CO_2 storage area does not indicate large-scale changes in thickness of the injection or confining zones.

The proposed WC IW-B No. 001 and No. 002 falls between the [redacted]. Major radial faulting associated with these domes occurs at depths and geographical locations outside the proposed injection area. They are all normal faults with an average dip of 45 degrees. The “radial” faults on the southeast side of [redacted] are more than [redacted] away from the edge of the currently predicted carbon front. All additional faults to the north are either well beyond the carbon front of WC IW-B No. 001 and No. 002 wells or are buried below the sealing [redacted] section and pose no threat of transmissibility.

Multiple faults to the southwest and west of the proposed locations occur at different levels of strata. These faults are normal faults that have similar orientations striking northwest-southeast with offsets ranging from 0 to 100 ft. [redacted]. Both fault offsets are well under 100 feet and pose no threat of transmissibility outside of the proposed injection interval. These faults are labeled [redacted] V and displayed in [redacted] *B-3*. [redacted]. These faults are displayed in [redacted] *B-1* as fault C and B. Although the modeled carbon front does not intersect either of these fault planes, additional fault seal analysis was performed and can be seen in *Section 1.8*.

Stratal dip within the injection interval varies with depth. The dip range within the carbon front outline at the [redacted] level is from 1 to 3 degrees, with the primary direction being updip to the northwest and downdip to the southeast. Little dip rotation occurs at the [redacted] level except for the [redacted], where it rotates to a more east-west trend. Dip ranges at the [redacted] level within the carbon front outline range from [redacted]. Primary dip direction follows the [redacted] trend, with the [redacted] dipping down to the southeast and up to the northwest. There is slight dip rotation within the northwestern portion of the carbon front, with the dip orientation rotating to a more west-northwest to east-southeast orientation. These attributes are displayed in the structure maps in *Appendix B-1, B-2*, and *B-3*.

Figure 1-19 – Location of a northwest-to-southeast (A-A') 3D seismic survey line crossing the proposed CO_2 storage area.

Figure 1-20 – North-south 3D seismic survey intersecting the proposed injection well,
which does not indicate the presence of obvious faults or large changes in thickness of the injection or confining zones at the proposed site.

1.3.6 Velocity Control and Synthetic Seismogram

Three velocity surveys were available around the 3D data used for the seismic interpretation shown in Figure 1-21. The checkshot velocity information, along with a synthetic tie from a well roughly [redacted] miles away from the proposed injection well, were used to confirm the time-to-depth relationship of the PSTM data, shown in Figure 1-22.

Figure 1-21 – Location of velocity surveys (indicated by magenta symbols) near 3D seismic data.

Figure 1-22 – Location of synthetic seismogram (blue circle) near the proposed injection well.

1.3.7 Gravity Data

Publicly accessible gravity data is available surrounding the proposed injection site. The data, though sparse (spatially), was reviewed for the project; the scale of the data is therefore insufficient to detect local features, such as *all* salt domes—and it may not augment the geological interpretation of the site. Figures 1-23 and 1-25 (pages 40 and 42, respectively) are regional overview maps by Steven Dutch, Professor Emeritus, Natural and Applied Sciences, University of Wisconsin – Green Bay ((Dutch, 2020). Figure 1-24 (page 41) displays a data set of gravity-station measurements from the USGS (Bankey & Daniels, 2008)—across the states of Louisiana and Arkansas, which cover the proposed storage site. Although these data points encompass a relatively widely spaced grid (approximately one data point every 9 miles), the grids shown in Figures 1-24 and 1-26 (page 43) are consistent with the known regional geologic setting of large thicknesses of Mesozoic sediments deposited in a wedge that thickens towards the Gulf of Mexico.

For Figures 1-24 and 1-26, the original data was extracted from the 1999 version of a gravity database maintained by the National Geophysical Data Center. Observed gravity measurements relative to the International Gravity Standardization Net 1971 (IGSN–71) datum were reduced to the Bouguer anomaly using the 1967 gravity formula (Cordell, Keller, & Hildenbrand, 1982) and a reduction density of 2.67 grams per cubic centimeter (g/cc). Terrain corrections were

calculated radially outward from each station to 167 km (100 mi) using a method developed by Plouff (Plouff, 1977).

The Isostatic Residual Gravity Map (Figure 1-26) reflects variations in the earth's gravity field caused by density variations in the rocks composing the upper part of the earth's crust. The isostatic residual gravity grid was derived from the Bouguer gravity anomaly data by removing the gravitational effect of the compensating mass that supports topographic loads. The thickness of this compensating mass was calculated using averaged digital topography by assuming a crustal thickness for sea-level topography of 30 km (18 mi), a crustal density of 2.67 g/cc, and a density contrast between the crust and upper mantle of 0.40 g/cc.

Positive value trends delineate rocks denser than the Bouguer reduction density of 2.67 g/cc, whereas a negative closure such as the -25.6 milligals (mGal) contour in Figure 1-23 results from rocks of lower density (such as salt structures). In general, gravity minimums highlight subsurface salt structures. However, in this area neither the regional map nor the USGS gravity data highlight the salt dome [redacted] northeast of the proposed storage site.

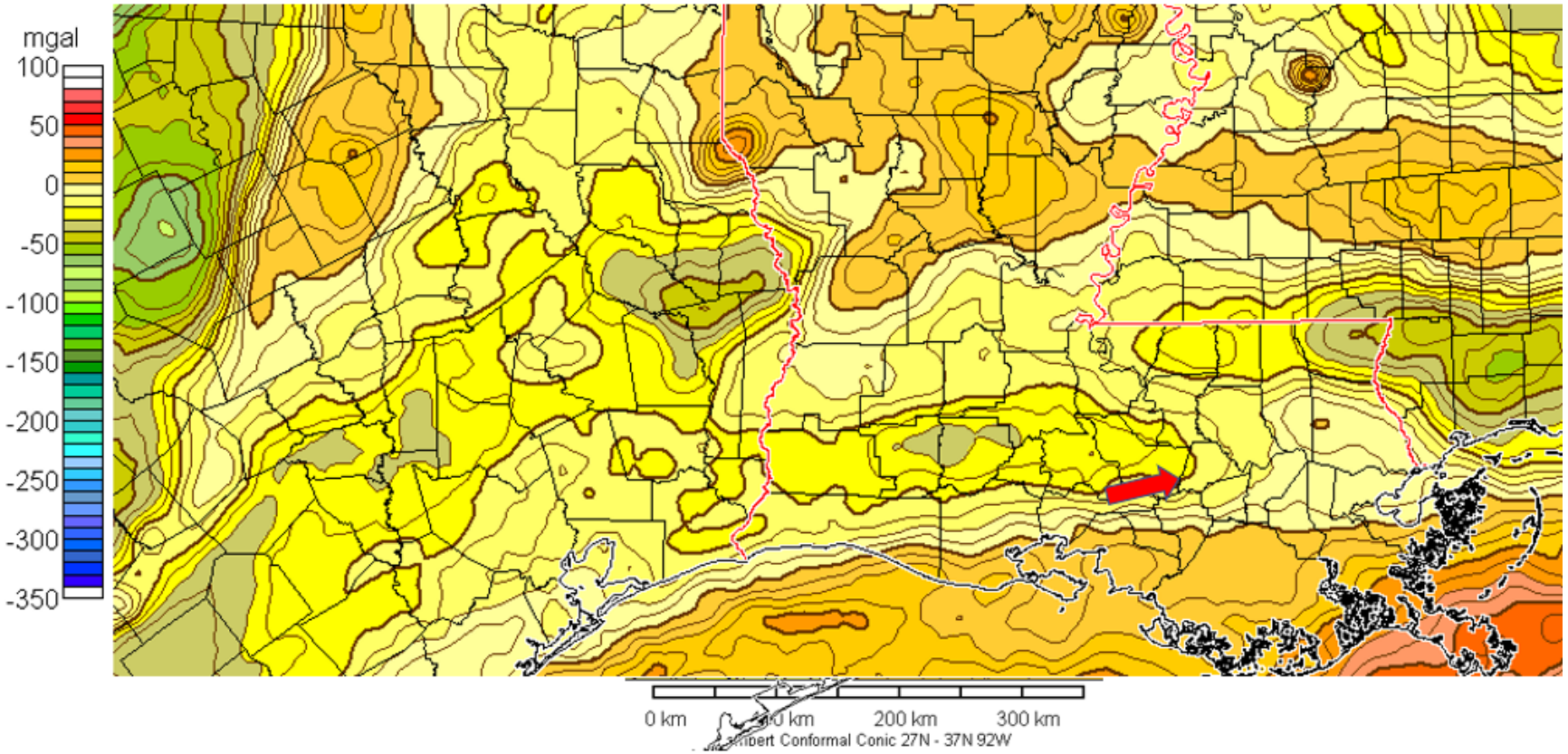

Figure 1-23 – A regional view of the Bouguer Gravity Anomaly Map for Louisiana. The red arrow indicates the proposed injection site (from https://www.stevedutch.net/stategeophmaps/lagphmap.htm).

Figure 1-24 – A view of the Bouguer Gravity Anomaly Map surrounding the proposed storage site (74 sq mi 3D) based on USGS data points.

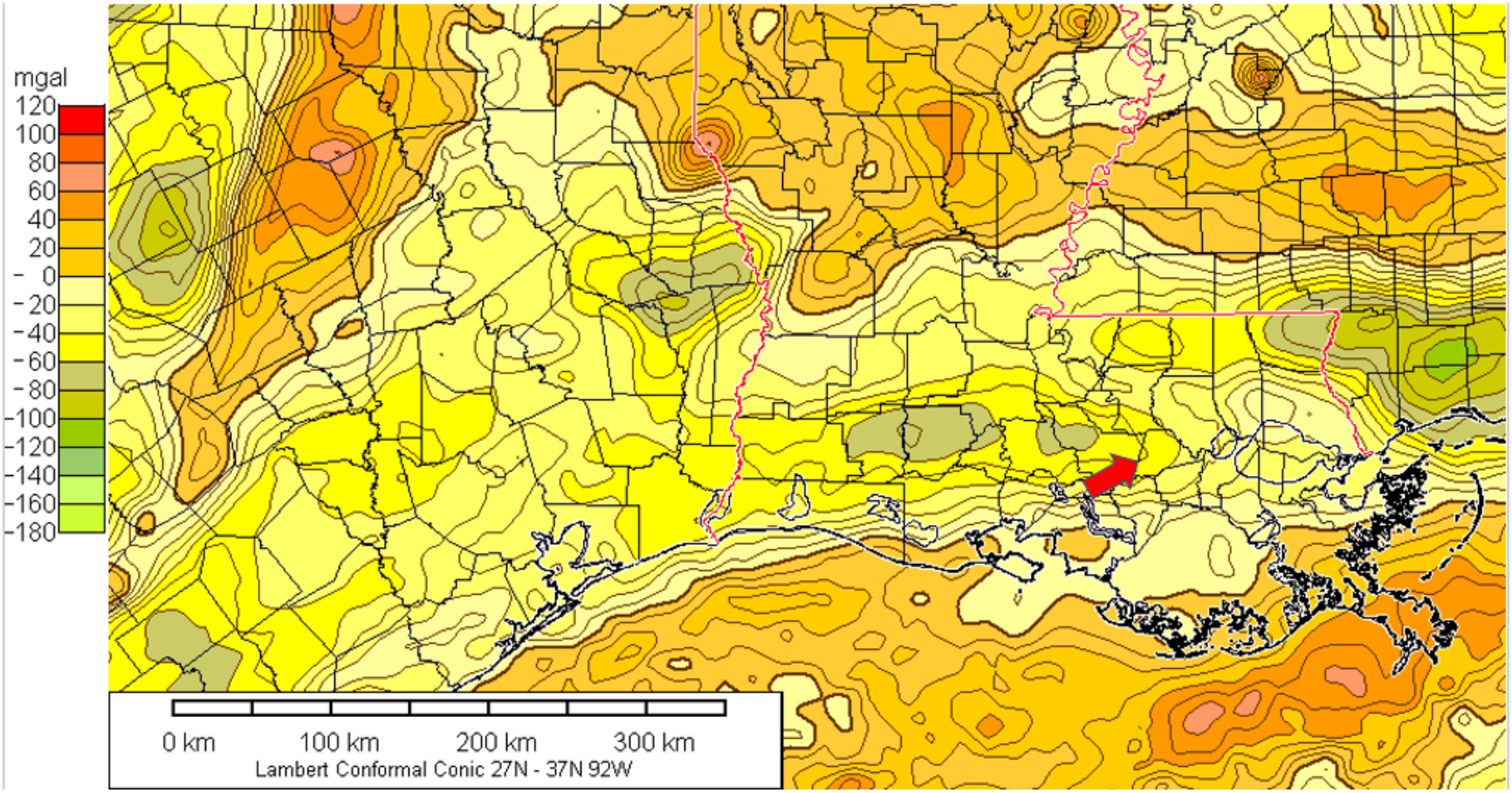

Figure 1-25 – A regional view of the Isostatic Gravity Anomaly Map for Louisiana. The red arrow indicates the proposed injection site (from https://www.stevedutch.net/stategeophmaps/lagphmap.htm).

Figure 1-26 – Isostatic Gravity Anomaly Map using the same USGS data points and spacing as Figure 1-24.

1.4 Geomechanics

1.4.1 Local Stress Conditions

Local stresses will be determined by running an X-dipole open-hole log in addition to performing "minifrac" tests, which are discussed in *Section 5 – Testing and Monitoring Plan*. Published maps of crustal stress orientation along the northern coast of the Gulf of Mexico basin indicate that the orientation of maximum horizontal stress (SHmax) is largely parallel to the coast, east-northeast, near the area of review (AOR) (Yassir & Zerwer, 1997).

1.4.1.1 Determination of Vertical Stress (S_v) from Density Measurements

The vertical stress can be characterized by the pressure exerted on a formation at a given depth due to the total weight of the rocks and fluids above that depth (Aird, 2019). The bulk density for the upper and lower confining and injection zones was calculated from log data at the offset [redacted]). Values were calculated for the top depth of the injection and lower confining zones. Due to the substantial thickness of the upper confining zone, values were calculated for the depth 100' above the base of the zone. The overburden gradient and vertical stress were calculated by integrating the bulk density from the surface to the formation depth in five-foot intervals. Table 1-4 shows the overburden gradient, vertical stress, and bulk densities of the top confining, injection, and lower confining zones.

Table 1-4 – Calculated Vertical Stresses

Formation	Depth (ft)	Bulk Density (g/cm^3)	Bulk Density (lb/ft^3)	Vertical Stress (psi)	Overburden Gradient (psi/ft)
[redacted]	[redacted]	[redacted]	[redacted]	[redacted]	[redacted]
[redacted]	[redacted]	[redacted]	[redacted]	[redacted]	[redacted]
[redacted]	[redacted]	[redacted]	[redacted]	[redacted]	[redacted]

(a) Values calculated for the depth 100' above the base of the corresponding zone.

1.4.2 Elastic Moduli and Fracture Gradient

Elastic moduli and fracture gradients are determined from laboratory analysis of core samples. Tests are performed on two-inch diameter vertical plugs from each core. Core samples are not available at this time and will be recovered during the drilling of the stratigraphic test well. The core samples will undergo triaxial compressive strength testing to provide the geophysical properties listed in Table 1-5.

Table 1-5 – Triaxial Compressive Strength Test Results

Sample Number	Depth (ft)	Zone	Formation	Confining Pressure (psi)	Compressive Strength (psi)	Young's Modulus (10^6 psi)	Poisson's Ratio
N/A[(a)]	N/A[(a)]	Upper Confining	[redacted]	N/A[(a)]	N/A[(a)]	N/A[(a)]	N/A[(a)]
N/A[(a)]	N/A[(a)]	Injection	[redacted]	N/A[(a)]	N/A[(a)]	N/A[(a)]	N/A[(a)]
N/A[(a)]	N/A[(a)]	Lower Confining	[redacted]	N/A[(a)]	N/A[(a)]	N/A[(a)]	N/A[(a)]

(a) Results are pending the retrieval and lab testing of cores, which will occur when the stratigraphic test well is drilled.

1.4.3 Fracture Gradient Calculation

The fracture pressure gradient was estimated using the uniaxial strain equation and fracture mechanics. The calculation inputs included vertical stress (S_v), pore pressure (P_p), and a value for the constant "K," which is the ratio of minimum horizontal effective stress to vertical effective stress. These variables can be changed to match the site-specific injection zone. "K" was assumed to equal 0.52 for shale and 0.48 for sand formations. To arrive at a conservative estimate, the fracture pressure was calculated as the minimum horizontal stress. This is the pressure required to open an existing fracture, which is less than the pressure required for fracture extension. The inputs as well as the resulting fracture pressure gradients are shown in Table 1-6, for the upper and lower confining zones and injection zone.

Inputs for the fracture gradient calculations were sourced from log data at the offset [redacted]. Using these values in Equation 1, a fracture gradient of [redacted] psi/ft was calculated for the upper confining zone. Due to the substantial thickness of the upper confining zone, values were calculated for the depth 100' above the base of the zone. This gradient was selected to calculate the maximum allowable bottomhole pressure, because it is slightly lower than the fracture gradients of the injection and lower confining zones. A [redacted] safety factor, as recommended in SWO 29-N-6 **§3621.A.1** [40 CFR **§146.88(a)**], was then applied to this number—resulting in a maximum allowable bottomhole pressure of [redacted] psi/ft. This was done to ensure that the injection pressure would never exceed the fracture pressure of the injection zone.

Equations with Variables:

(Eq. 1) $$FG = K \times (S_v - P_p) + P_p$$
$$FG\ with\ SF = FG \times (1 - 10\%)$$

Where:
K = the ratio of minimum horizontal effective stress to vertical effective stress
S_v = vertical stress
P_p= pore pressure
FG= fracture gradient
SF= safety factor

Equations with Values for Upper Confining Zone:

$$FG = 0.52 \times (0.902 - 0.460) + 0.460 = 0.690\ psi/ft$$
$$FG\ with\ SF = 0.690 \times (1 - 10\%) = \mathbf{0.62\ psi/ft}$$

Table 1-6 – Fracture Gradient Calculation Inputs and Results

Depth (ft)	Zone	Formation	Vertical Stress (psi/ft)	Pore Pressure (psi/ft)	Fracture Gradient (psi/ft)
[redacted]	[redacted]	[redacted]	[redacted]	[redacted]	[redacted]
[redacted]	[redacted]	[redacted]	[redacted]	[redacted]	[redacted]
[redacted]	[redacted]	[redacted]	[redacted]	[redacted]	[redacted]

(a) Values calculated for the depth 100' above the base of the corresponding zone.

Ultimately, the fracture pressure of the injection and confining zones, as required by SWO 29-N-6 **§3617.B.4.a** [40 CFR **§146.87(d)(1)**], will be determined by minifrac tests completed during the open-hole logging program on the proposed injection well. Maximum allowable injection pressures will be determined based on the results of these tests in accordance with SWO 29-N-6 **§3621.A.1** [40 CFR **§146.88(a)**]. If the minifrac tests cannot identify a fracture gradient, core analysis will be performed and the results used in conjunction with Eaton's method, to determine the fracture pressure.

1.5 Porosity and Permeability

Porosity and permeability distributions at the WC IW-B No. 001 and 002 locations are heavily driven by deposition and post-burial events. High influx of sediments from the Mississippian

delta system created an environment with channelized sands with intermittent shales and silts. The injection sands contain high concentrations of quartz and have little calcite cementation at the depth of injection (Smith & Tieh, 1984). Due to the injection interval being normal in pressure and temperature, permeability destruction due to quartz overgrowth is unlikely. Therefore, injection sands within the injection interval should be unconsolidated in nature and reflect higher vertical-to-horizontal permeability ratios. These ratios are directly proportionate to effective porosity due to the shales and silts within these sands acting as baffles. The primary porosity trend seen on the Gulf Coast is *compaction*, which is the reduction of porosity with depth due to the decreasing amount of intergranular pore space—due to greater mechanical compaction. This trend can be seen in Figure 1-36 (*Section 1.5.2.2*) with porosity decreasing with depth.

Porosity and permeability estimates for the reservoir and confining intervals were made through a petrophysical analysis on offset open-hole logs and core data. The nearest well to the proposed storage site with available density/neutron porosity log data over the proposed injection interval is [redacted]). The following process was applied to that well to establish a relationship between lithology-indication logs and effective porosity. *Effective porosity* is a measure of the amount of intergranular or connected void space in a rock, which approximates available pore space for fluid movement better than *total porosity*. Total porosity includes intragranular pore space that may be detached from the pore network.

Quality assurance was performed to ensure that only valid data is used in forward calculations. A comparison of digital or Log American Standard Code for Information Interchange (ASCII) Standard (LAS) log data with a corresponding raster log was performed; digital curves were corrected as necessary, to honor the original raster log data. Washouts in the bulk density log that may artificially inflate porosity values were excluded from trend lines, as shown in Figure 1-27. A trend line to explain SP drift over depth was established to correct SP with depth. Baseline shifts in SP were identified during this analysis, shown in Figure 1-28.

Figure 1-27 – Log depicting example of washouts identified during the quality assurance process.

Example of SP Baseline shift

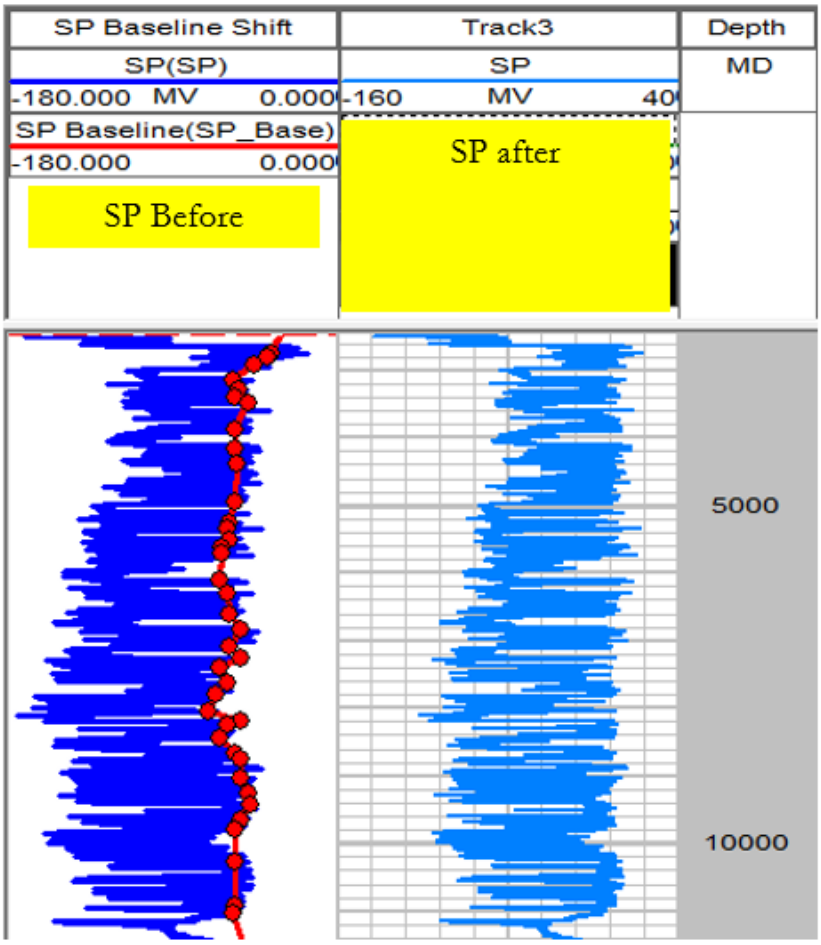

Figure 1-28 – Example of SP Baseline Shift Over Depth

After SP curves were corrected, Vshale was computed from the SP logs.

$$Vshale = \frac{(SP - SPsand)}{(SPshale - SPsand)}$$

Where:
SP = spontaneous potential
$SPsand$ = spontaneous potential reading of a sand
$SPshale$ = spontaneous potential reading of a shale

Estimated effective porosity (PHIEST, Φ_{eff}) is calculated using the Vshale log and PHIMEAN.

$$\emptyset_{eff} = \emptyset_{mean} * (1 - Vshale)$$

Where:
$\emptyset_{eff}$ *= effective porosity*
$\emptyset_{mean}$ *= mean porosity*

A quality check of the PHIEST curve was performed by overlaying the computed PHIEST with the PHIE curve calculated from measured density porosity logs. Figure 1-29 (page 51) demonstrates a good fit between the computed and measured curves. The PHIEST curve was applied to surrounding wells with SP log data to produce best estimates of effective porosities over the Miocene intervals.

As Φ_{eff} is a measure of interconnected pore space, a relationship with permeability can be established. Sidewall core reports were taken from an offset well, [redacted]), roughly [redacted] miles away, and analyzed. A copy of this core report is attached in *Appendix B-14*. A relationship was determined between porosity and associated permeabilities from this core data as shown in Figure 1-30 (page 52). The cores were taken from a wide range of Vshale intervals, which allowed for a robust depiction of permeability ranges that will most likely be encountered within the injection and confining intervals. This variability is shown in Figure 1-31 (page 53) through a histogram of the Vshale log readings within the cored intervals. To better represent the core vs. porosity relationship, two trend lines were determined within the same data set. The trends were separated by the [redacted] effective porosity mark, with each being applied when effective porosities were greater or less than [redacted]. The equations used to determine permeability are as follows:

[redacted]

These equations were applied to 32 wells offset from the proposed injection site and used to develop porosity and permeability distributions within the model.

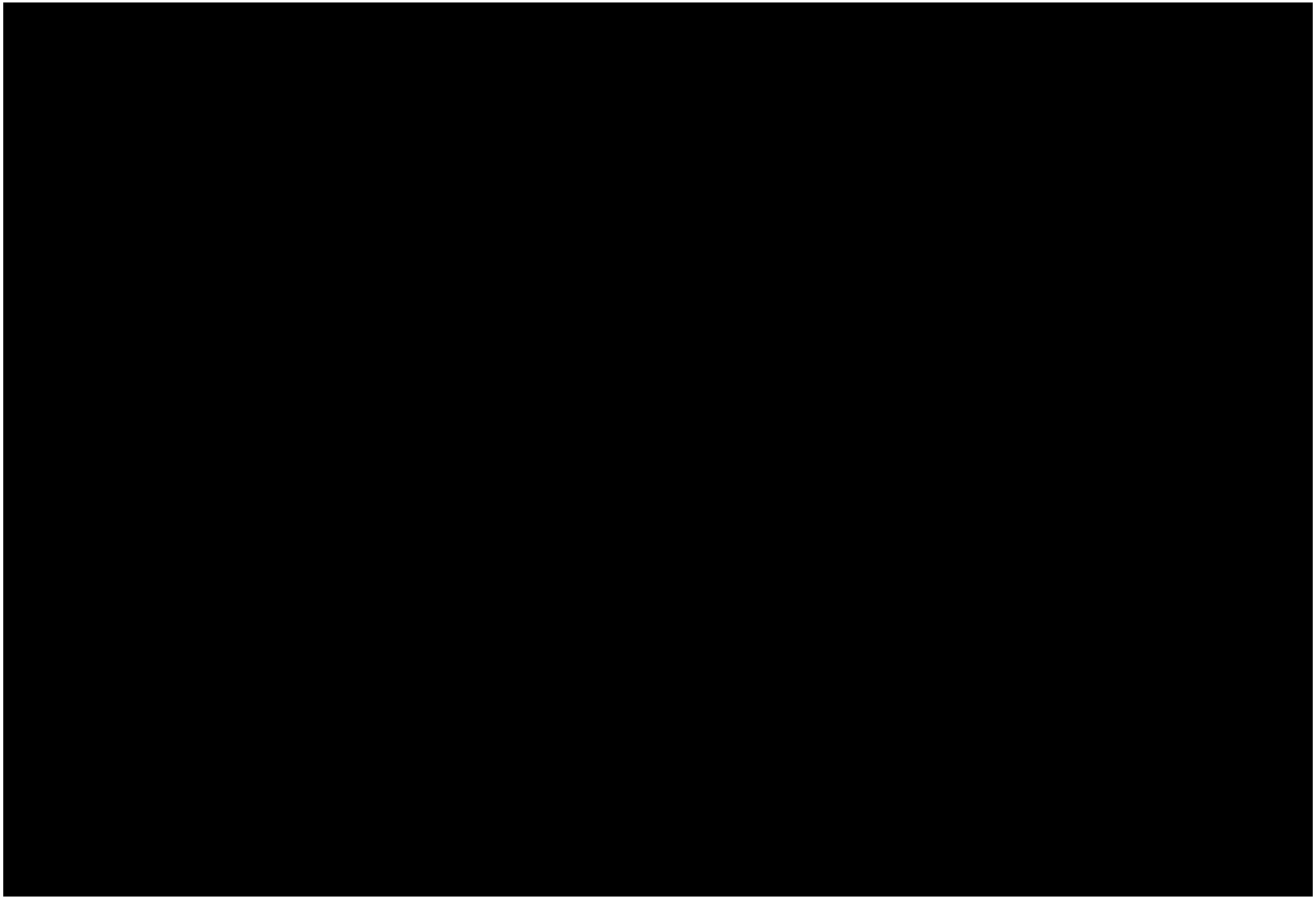

Figure 1-29 – Comparison between calculated effective porosity (PHIE) and estimated effective porosity (PHIEST).

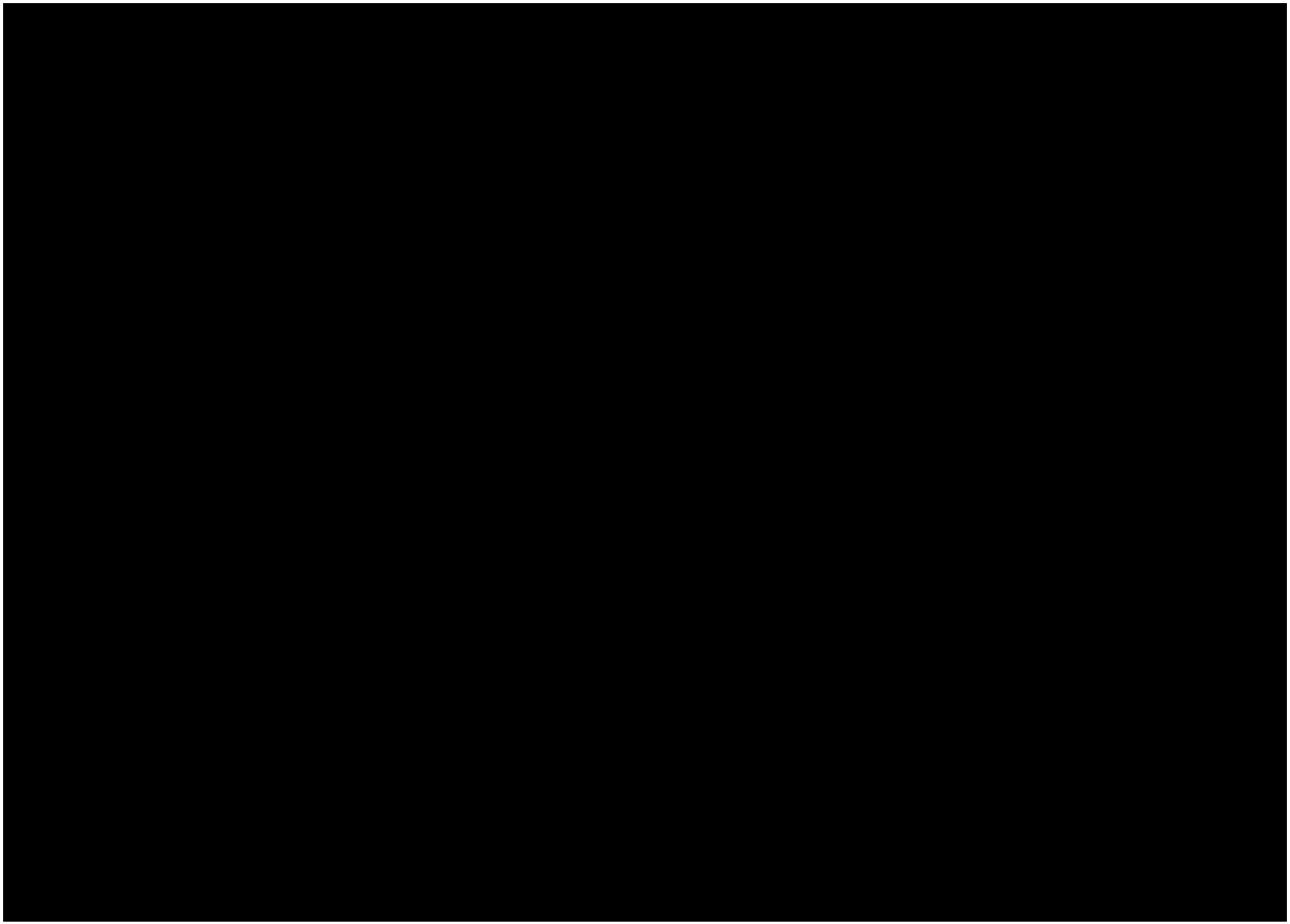

Figure 1-30 – Porosity vs. Permeability Scatterplot of Sidewall Core from SN [redacted]

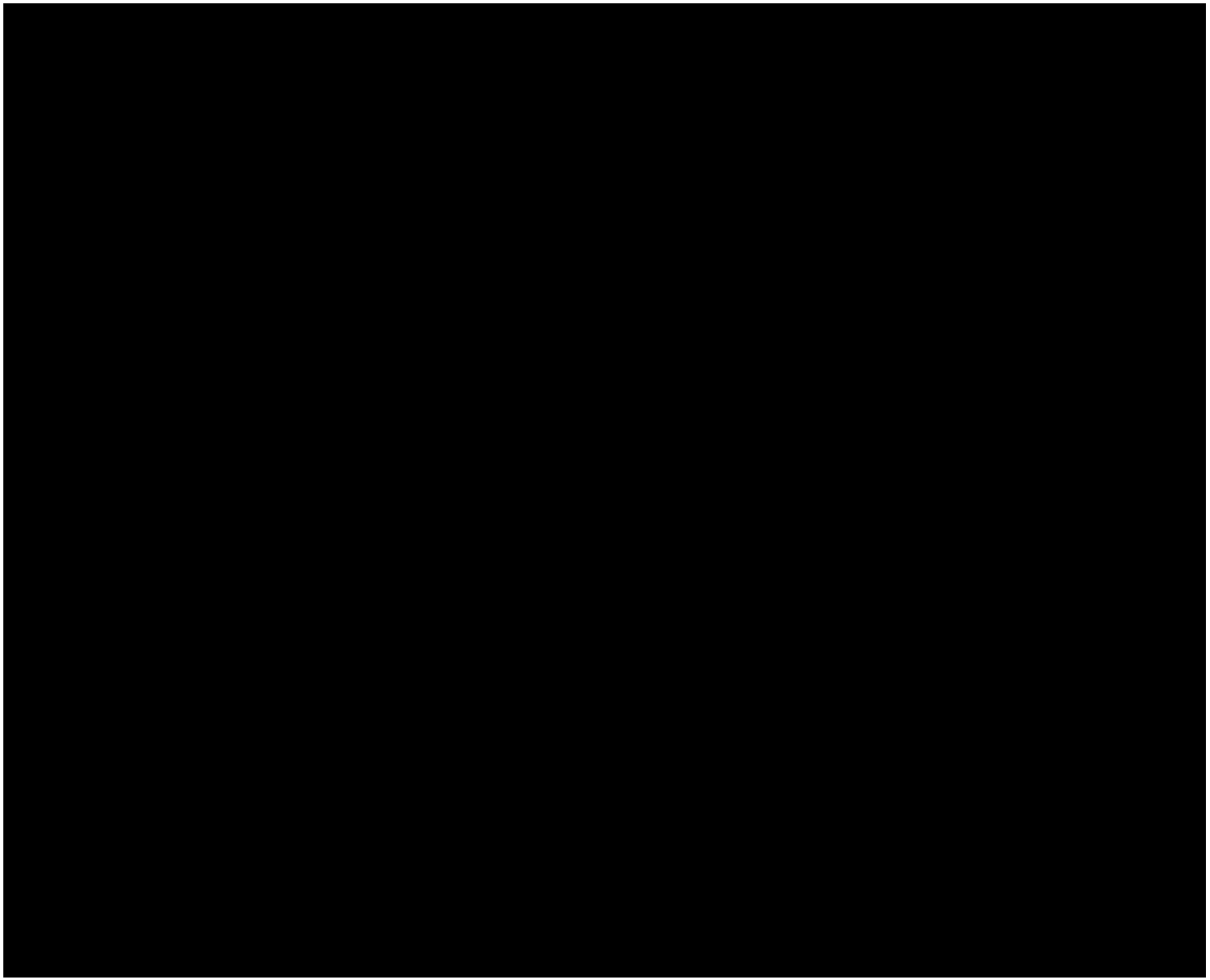

Figure 1-31 – Histogram of the Vshale distribution over the cored intervals within SN [redacted].

1.5.1 Upper Confining Zone

The [redacted] contains high clay content due to the depositional features described in *Section 1.3.2*. The high shale net to gross ratio is reflected within the permeability and porosity distributions within the Big A. Figure 1-32 is an open-hole log image of SN [redacted], with PHIEST representing estimated effective porosity and K_Core_2500 representing permeability. Within the gross confining interval, thin channel sands are present that display higher porosity and permeabilities. Although the confining unit clearly displays a much higher proportion of low permeability/porosity shales, these sands will affect the gross average porosity and permeabilities within the upper confining zone, skewing the values to not reflect its confining nature. Therefore, permeability and porosity filters were applied to depict the confining nature of the shale facies within the upper confining zone. The filters applied to the porosity and permeability were [redacted], respectively, and are referred to as the shale facies. Distributions of the porosity and permeabilities within the model that reflect these facies are depicted in Figures 1-33 and 1-34 (pages 56 and 57, respectively).

1.5.1.1 Porosity

Within the shale facies in the upper confining interval, the average effective porosity is [redacted]. Figure 1-32 presents the histograms displaying these distributions. With the same filters applied within the [redacted] unit, there is a projected net value of [redacted] at the proposed WC IW-A No. 001 location. This is portrayed in Figure 1-35 (page 58), which is a net isopach map of the filters described above. With such an ample amount of net low-porosity facies within the upper confining zone, transmissibility through this confining unit is unlikely.

1.5.1.2 Permeability

Within the shale facies in the upper confining interval, the average permeability is [redacted] Figure 1-33 presents the histograms displaying these distributions. Similar net values of [redacted] will be seen with the [redacted] filter applied as shown in Figure 1-35 (*Appendix B-5*). Due to very low horizontal and vertical permeabilities, along with abundant net interval, transmissibility through this confining unit is unlikely.

Further evidence that the [redacted] will act as an optimal confining unit comes from a study by Bump et al. (2023), describing the pros of having a "composite confining system," which is defined by a "multi-layer stratigraphic system of sub-horizontal but potentially discontinuous flow barriers with no a priori requirement for minimum capillary entry pressure values or lateral continuity of individual elements" (Bump, et al., 2023). This study was conducted in southern Louisiana in a very similar depositional environment, in formations similar to the ones being proposed for sequestration, and concluded "permanent storage may be better served by composite confinement than by classic petroleum seals" (Bump, et al., 2023). This was concluded despite the lack of continuous seal, because the CO_2 tends to channelize underneath the capillary barriers, spreading the CO_2 laterally with significant residual trapping that attenuates and ultimately immobilizes the carbon front (Bump, et al., 2023). [redacted], located just northeast of the proposed injection site, was included in this study—furthering certainty that the proposed upper confining zone will sufficiently seal any injected CO_2.

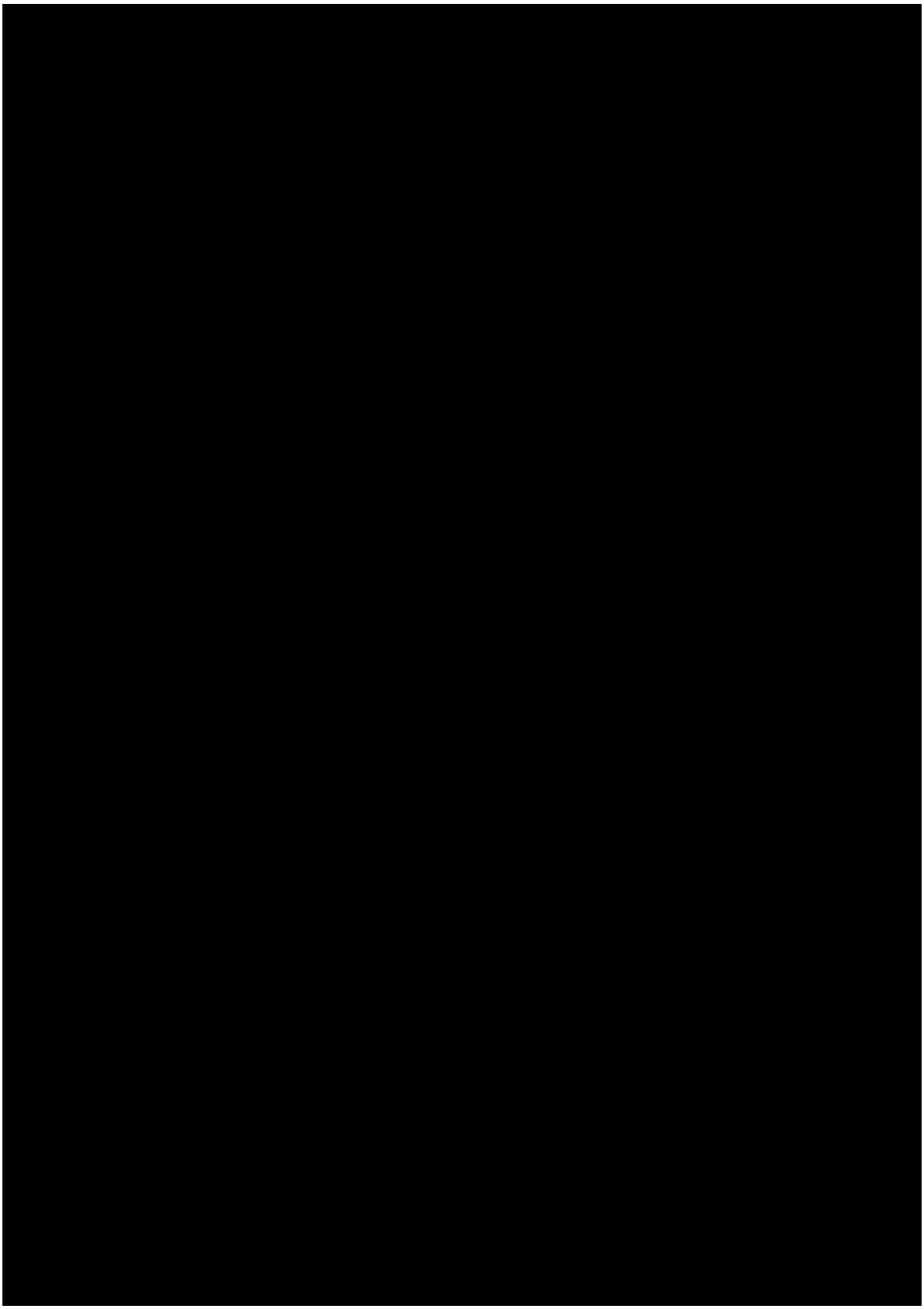

Figure 1-32 – Open-hole log of offset well SN [redacted] depicting the upper confining interval. Effective porosity is displayed in green and permeability in red.

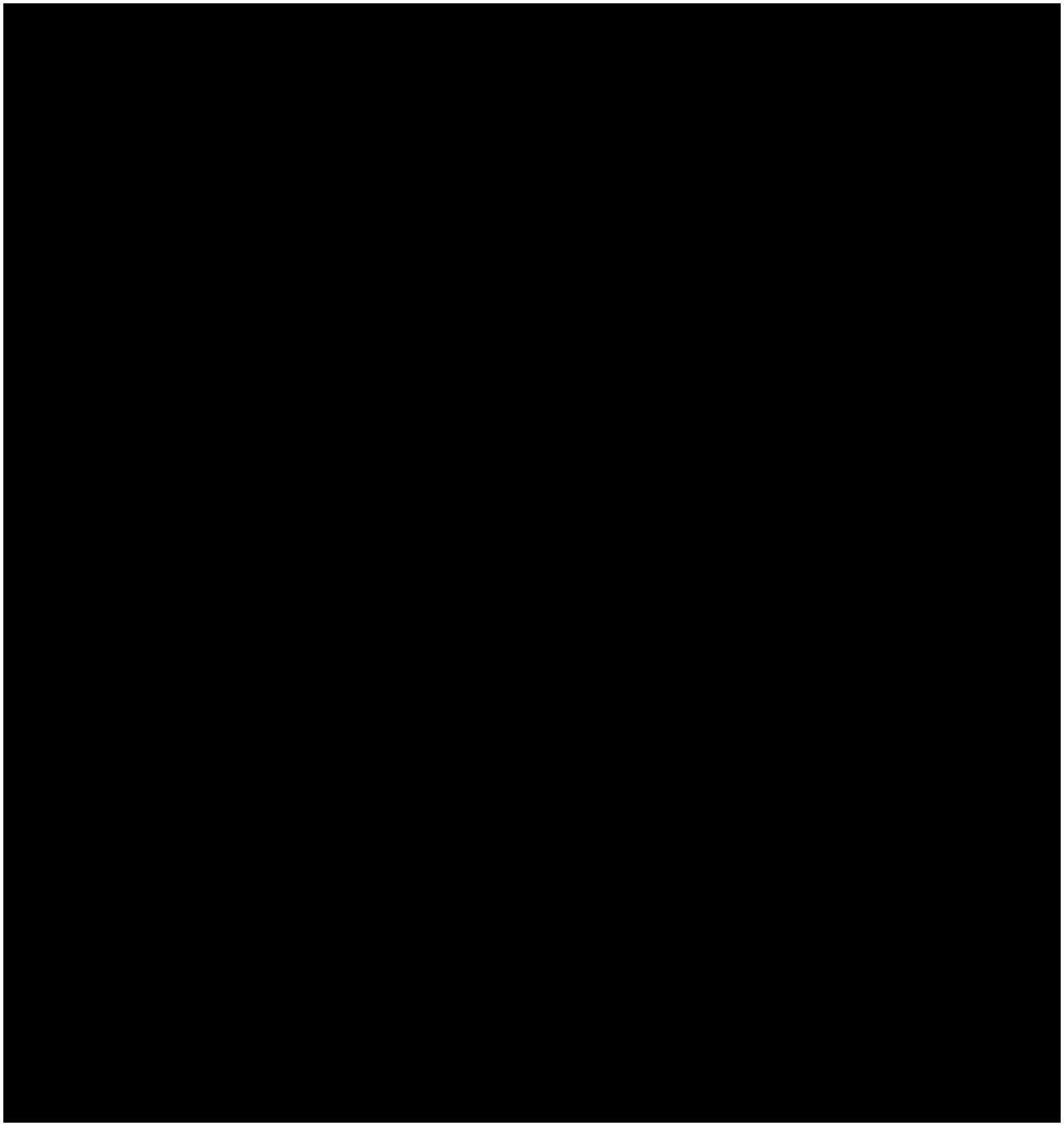

Figure 1-33 – Histogram of Porosity Distributions Within the Upper Confining Zone

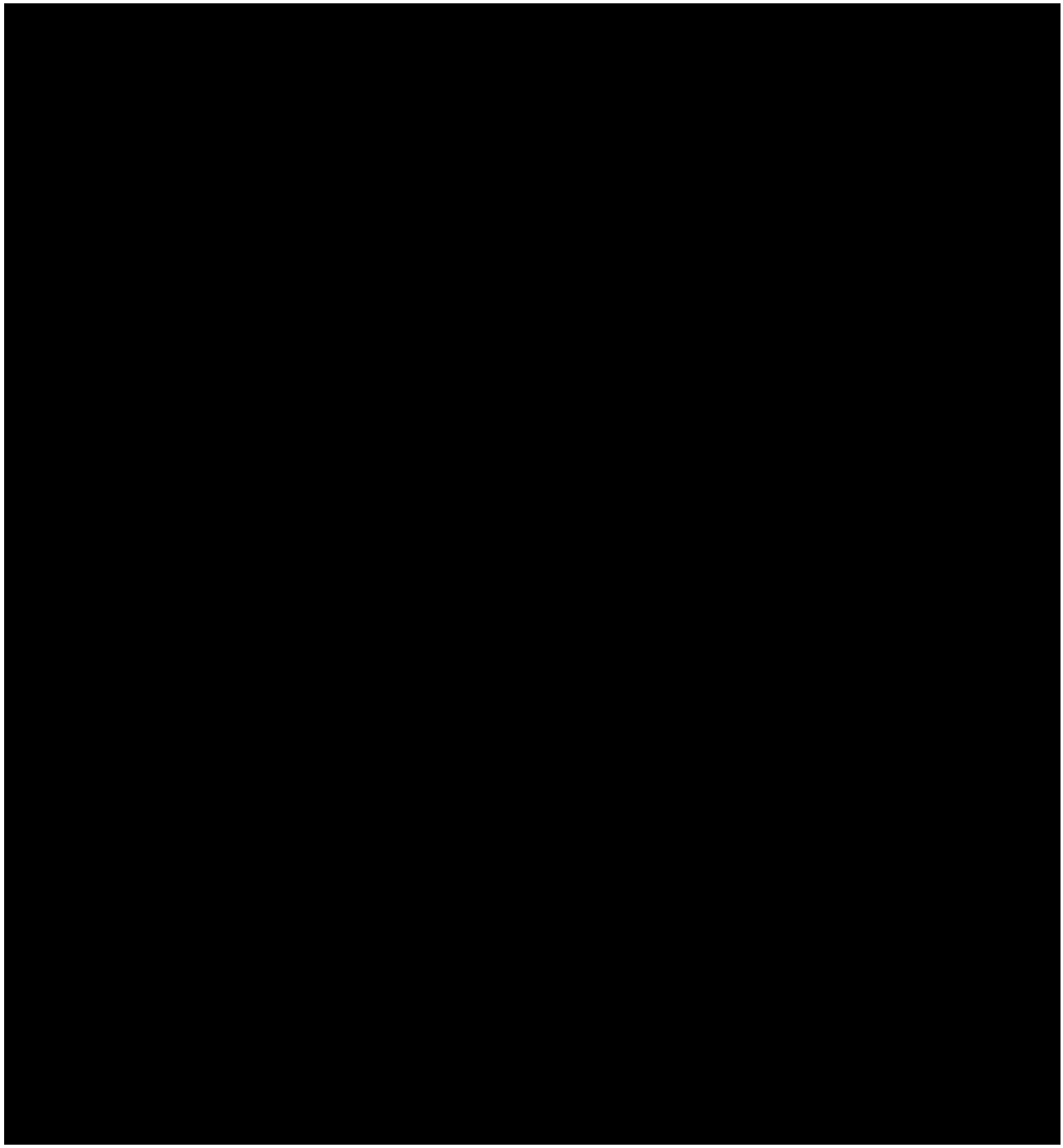

Figure 1-34 – Histogram of Permeability Distributions Within the Upper Confining Zone

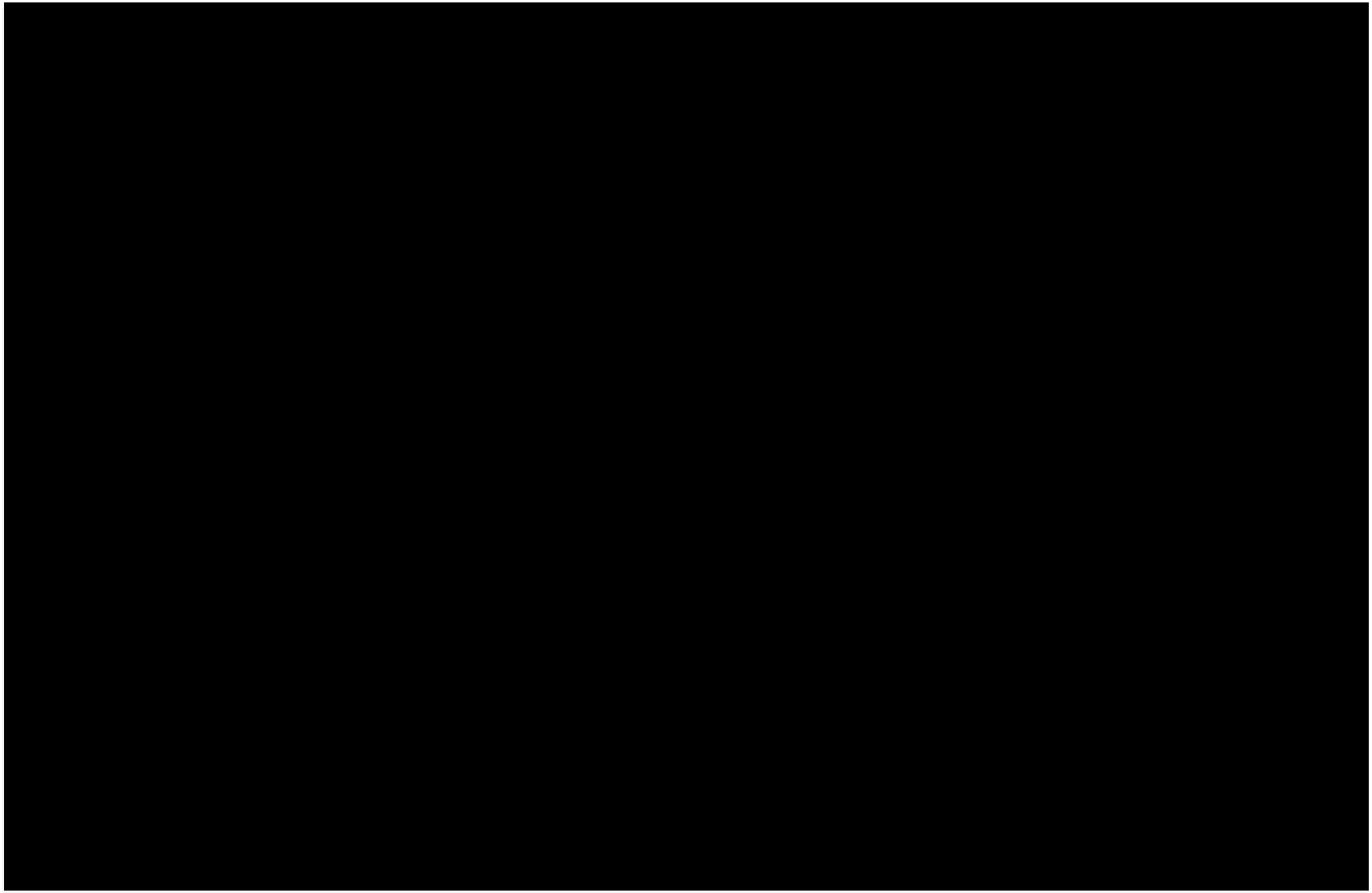

Figure 1-35 – Net Upper Confining Isopach Map of the facies reflecting a [redacted] porosity and [redacted] permeability.

1.5.2 Injection Zone

The Upper and Middle Miocene formations make up the injection zone for the proposed WC IW-B No. 001 and 002. The permeability and porosity distributions within this interval are heavily influenced by the deposition depicted in *Section 1.3.1*. Figure 1-36 is an open-hole log image of SN [redacted], with PHIEST representing estimated effective porosity and K_Core_2500 representing permeability. Within the injection interval, deltaic sands with higher effective porosities and permeabilities will be the target compartments for injection, with the interbedded shales acting as compartment seals. Figure 1-36 depicts these injection compartments where the permeability and porosity are clearly higher within the sand intervals than the shale intervals. Filters applied to the porosity and permeability were [redacted], respectively, to filter out the shalier porosity and permeabilities, to better depict the injection sands' reservoir characteristics within the injection interval.

1.5.2.1 Porosity

Within the sandier sections of the injection interval, the average effective porosity is 24[redacted]. Figure 1-37 (page 60) presents the histograms displaying these distributions. These porosities reflect the depositional environments and lack of diagenetic destruction of the Miocene sands on the Gulf Coast. As previously stated, porosity trends within the Miocene sands decrease with depth due to compaction, which can be seen in Figure 1-36. A net map of [redacted] porosity was created for the injection zone and can be found in *Appendix B-7*. As seen in this map, [redacted] porosity will be found at the proposed injection well location.

1.5.2.2 Permeability

Within the sandier sections of the injection interval, the average permeability is [redacted]. Figure 1-38 (page 61) presents the histograms displaying these distributions. Due to the fact that permeability is directly related to porosity, similar trends can be seen within the permeability distributions as the porosity described above. Vertical vs. horizontal (Kv/Kh) permeability ratios will increase with increased porosity/permeability due to the lack of diagenetic sequences within the injection interval. Therefore, porosity readings that are directly affected by the cleanliness of the sands will dictate the ratios attributed to each sand. This ratio trend will be further discussed in *Section 2 – Carbon Front Model*.

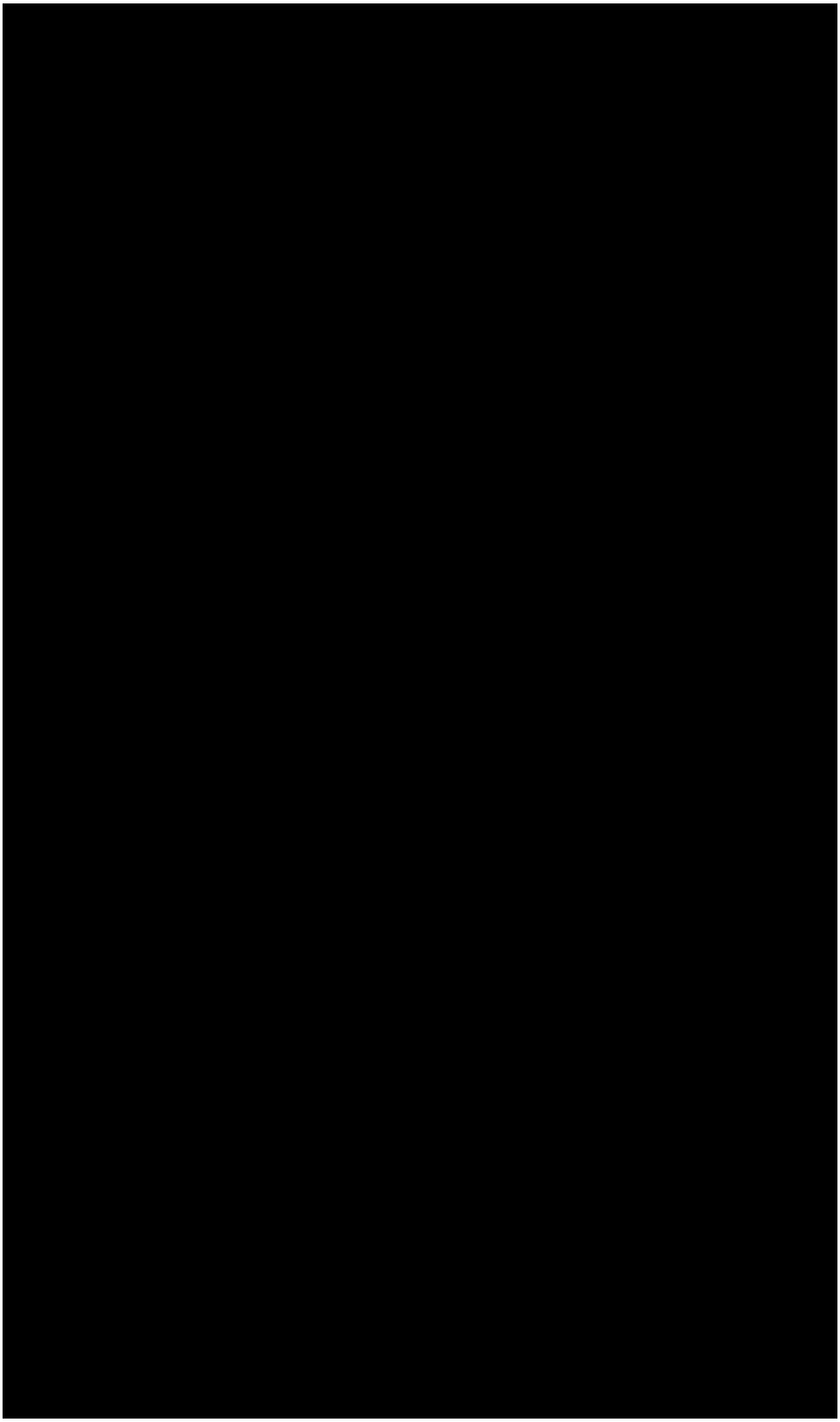

Figure 1-36 – Open-hole log of offset well SN [redacted] depicting the injection interval. Effective porosity is displayed in green and permeability in red

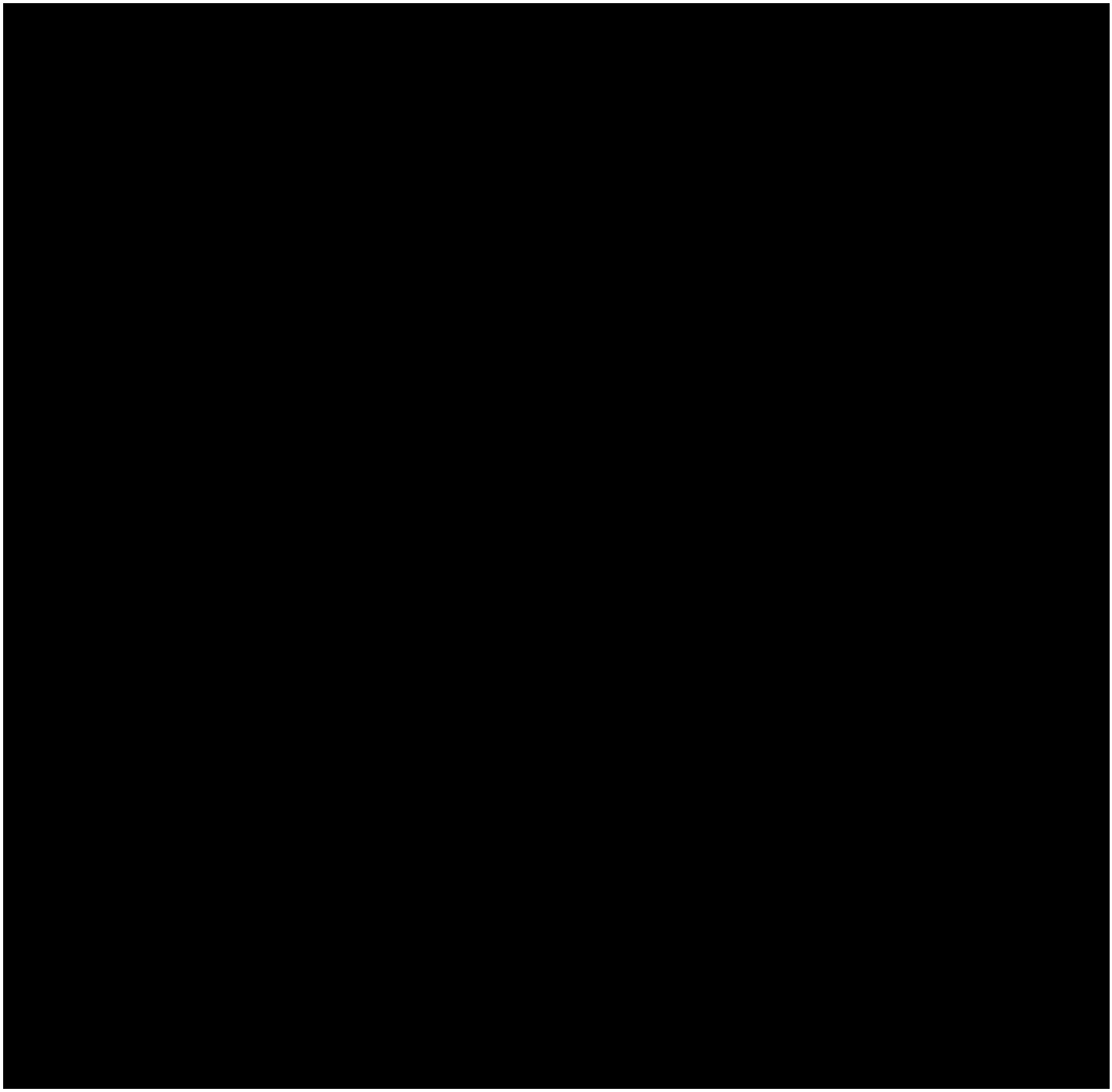

Figure 1-37 – Histogram of Porosity Distributions Within the Injection Interval

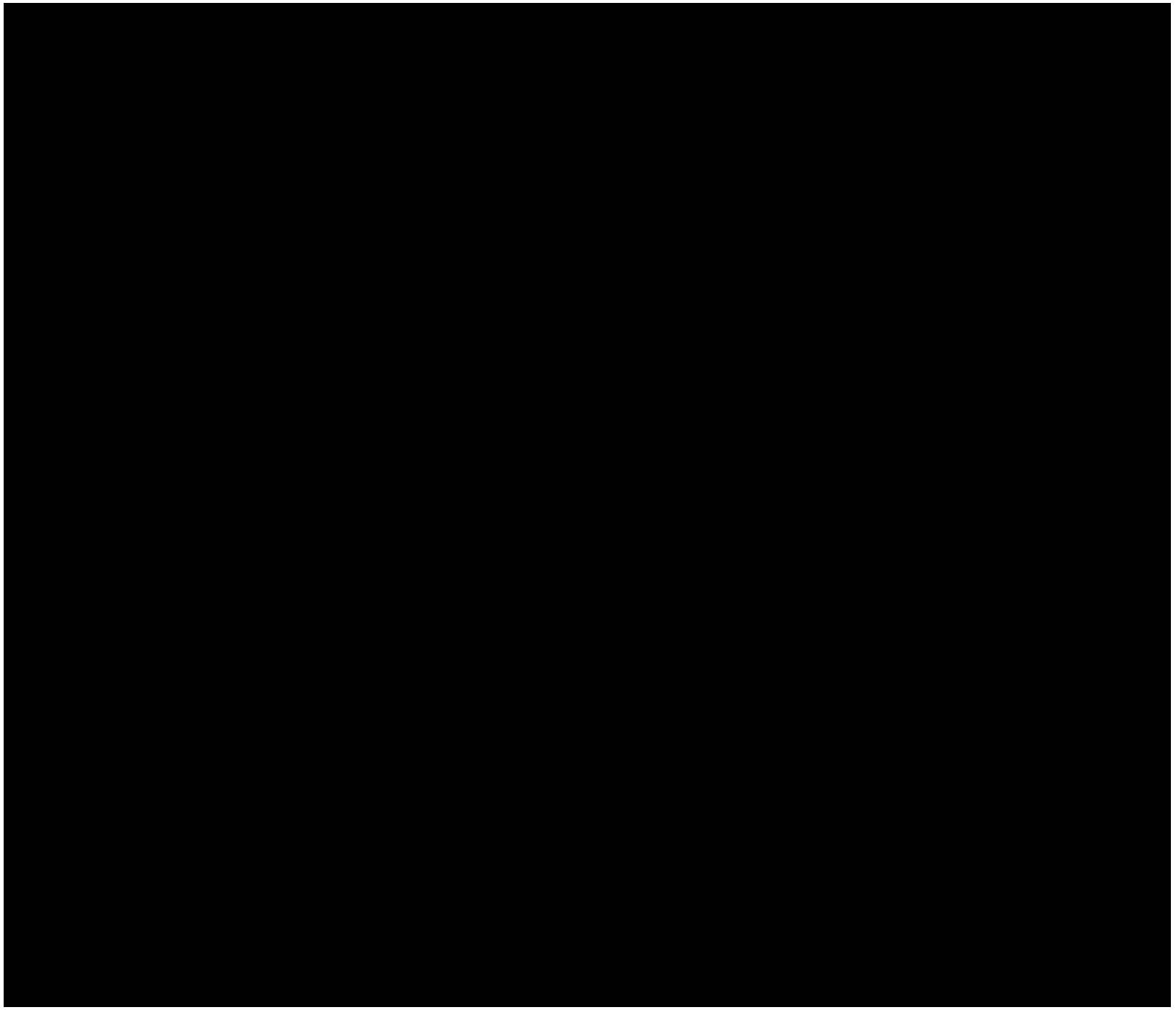

Figure 1-38 – Histogram of Permeability Distributions Within the Injection Interval

1.5.3 Lower Confining Interval

The [redacted] is a laterally extensive regional maximum flooding surface that occurred in the early portion of the Lower Miocene, depositing a regional layer of clay and silt. Further detail on the depositional environment was discussed in *Section 1.3.3*. Figure 1-39 is an open-hole log image of SN [redacted], with PHIEST representing estimated effective porosity and K_Core_2500 representing permeability. A thick and continuous bed interpreted as a maximum flooding surface occurs within the [redacted] lower confining interval, depicting impermeable shale with little to no effective porosity. The filters applied to the porosity and permeability were [redacted], respectively—even though both gross and net values display a very impermeable section.

1.5.3.1 Porosity

Within the shalier facies in the lower confining interval, the average effective porosity is [redacted]. Figure 1-40 (page 65) presents the histograms displaying these distributions.

1.5.3.2 Permeability

Within the shalier facies in the lower confining interval, the average permeability is [redacted]. Figure 1-41 (page 66) presents the histograms displaying these distributions.

These results reflect an optimal lower confining zone that will adequately act as a lower seal for the proposed injection site.

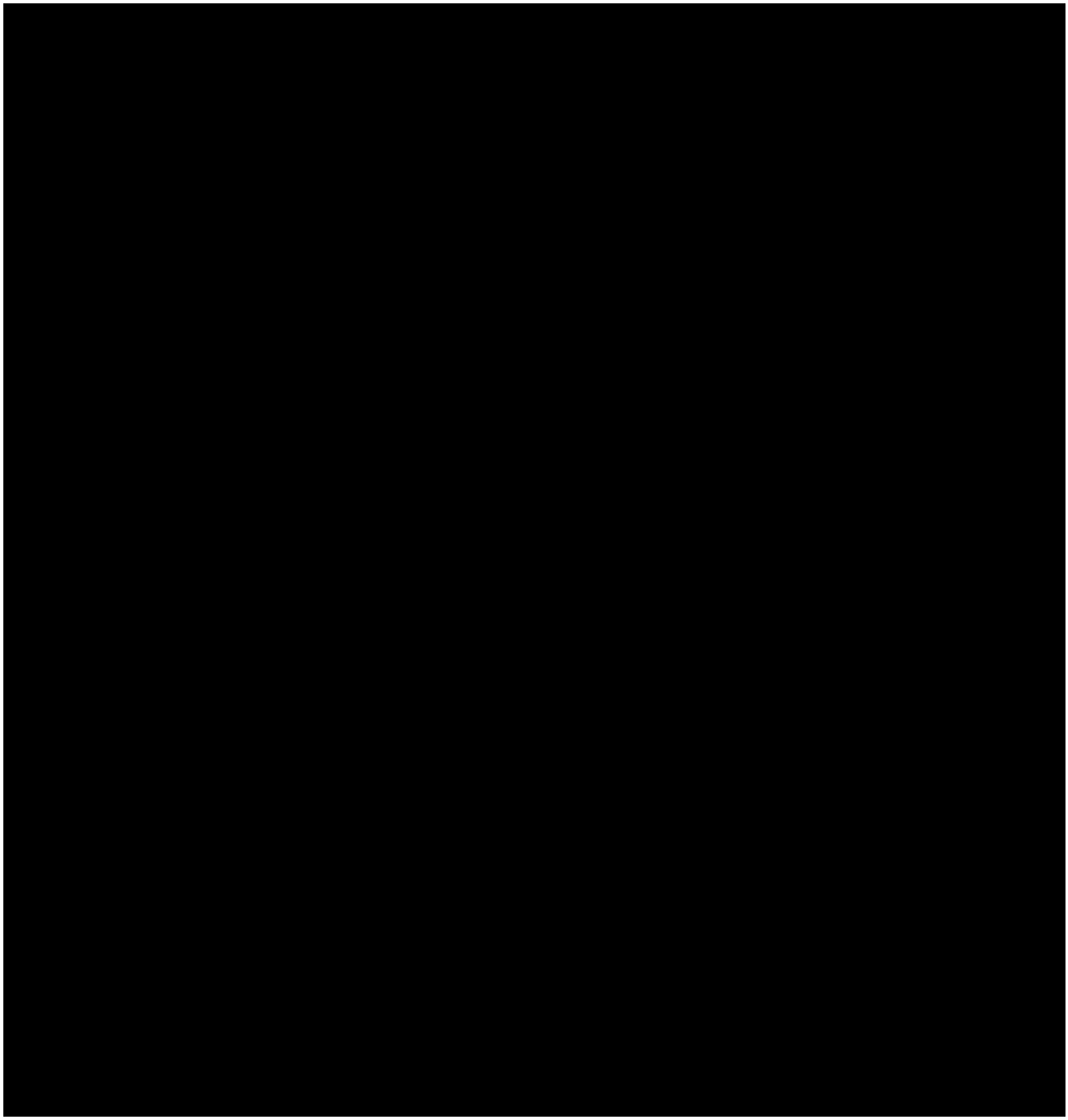

Figure 1-39 – Open-hole log of offset well SN [redacted] depicting the lower confining interval. Effective porosity is displayed in green and permeability in red.

Figure 1-40 – Histogram of Porosity Distributions Within the Lower Confining Zone

Figure 1-41 – Histogram of Permeability Distributions Within the Lower Confining Zone

1.6 Injection Zone Water Chemistry

A water sample from [redacted] on the eastern flank of the [redacted] field was provided to Core Lab for analysis. Figure 1-42 is a complete water analysis of sample RFS ID No. 202206840-02. (A copy of the analysis is included in *Appendix B-15*.) To ensure the analyzed samples are representative of the entire project AOR, a review of nearby produced waters from Miocene sandstones was performed.

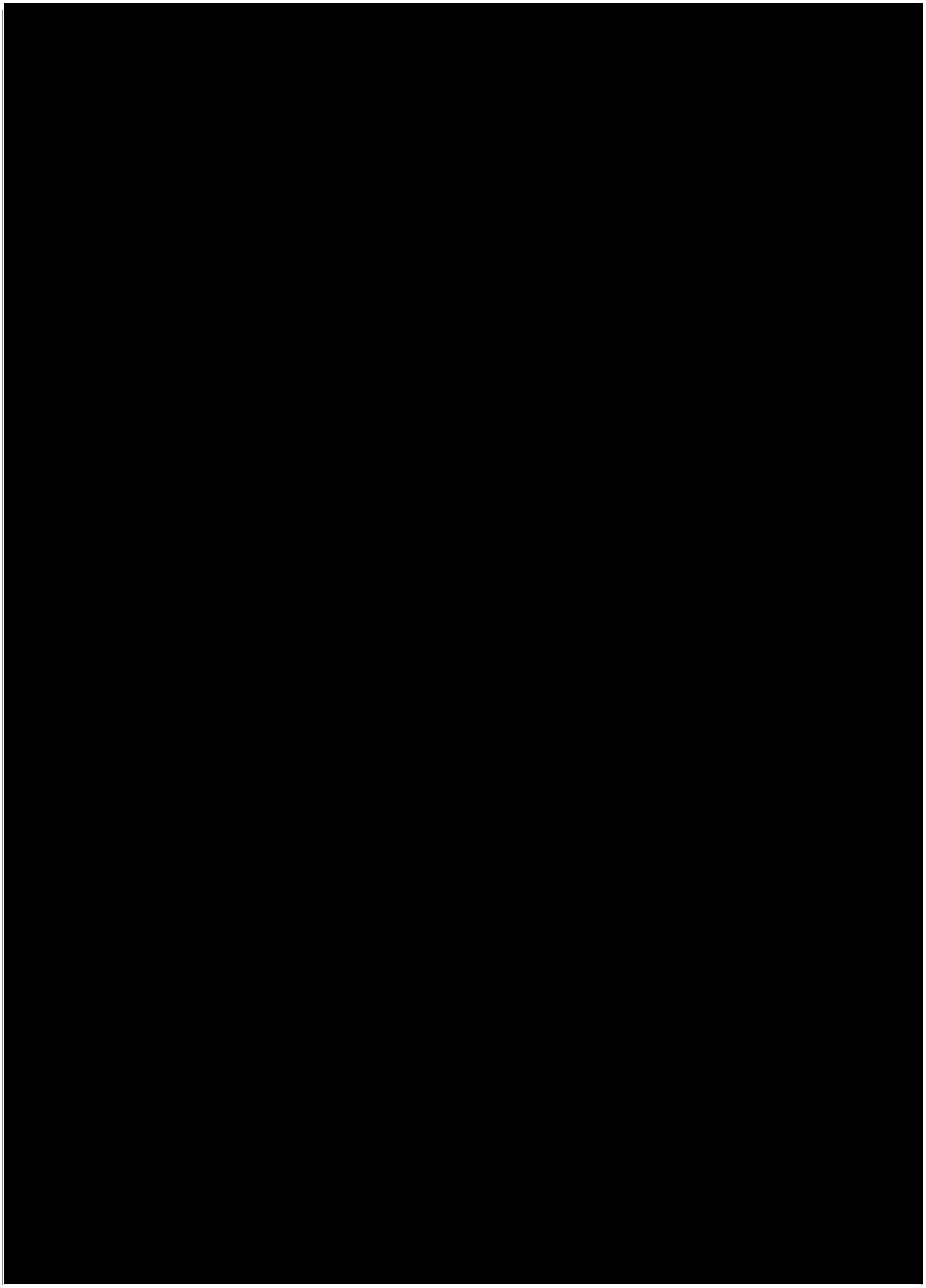

Figure 1-42 – RFS ID No. 202206840-02 Complete Water Analysis Report

The USGS National Produced Waters Geochemical Database was filtered to fluid samples from Miocene sands, in a geographic window ranging from [redacted] This area was chosen to incorporate a range of depth values to examine the relationship between salinity and depth. Figure 1-43 is a plot of measured depth (ft) and total dissolved solids (TDS) (mg/l) from the filtered USGS data set and the water analysis from [redacted]. Approximate depths of the proposed injection interval are included on the scatterplot for reference. Over the depths of the injection interval, the average salinity profile is consistent at approximately [redacted] mg/l. The measured data from Core Lab's analysis, sample RFS ID No. 202206840-02, lies within the anticipated values of the regional data set and is considered representative of the entire injection interval.

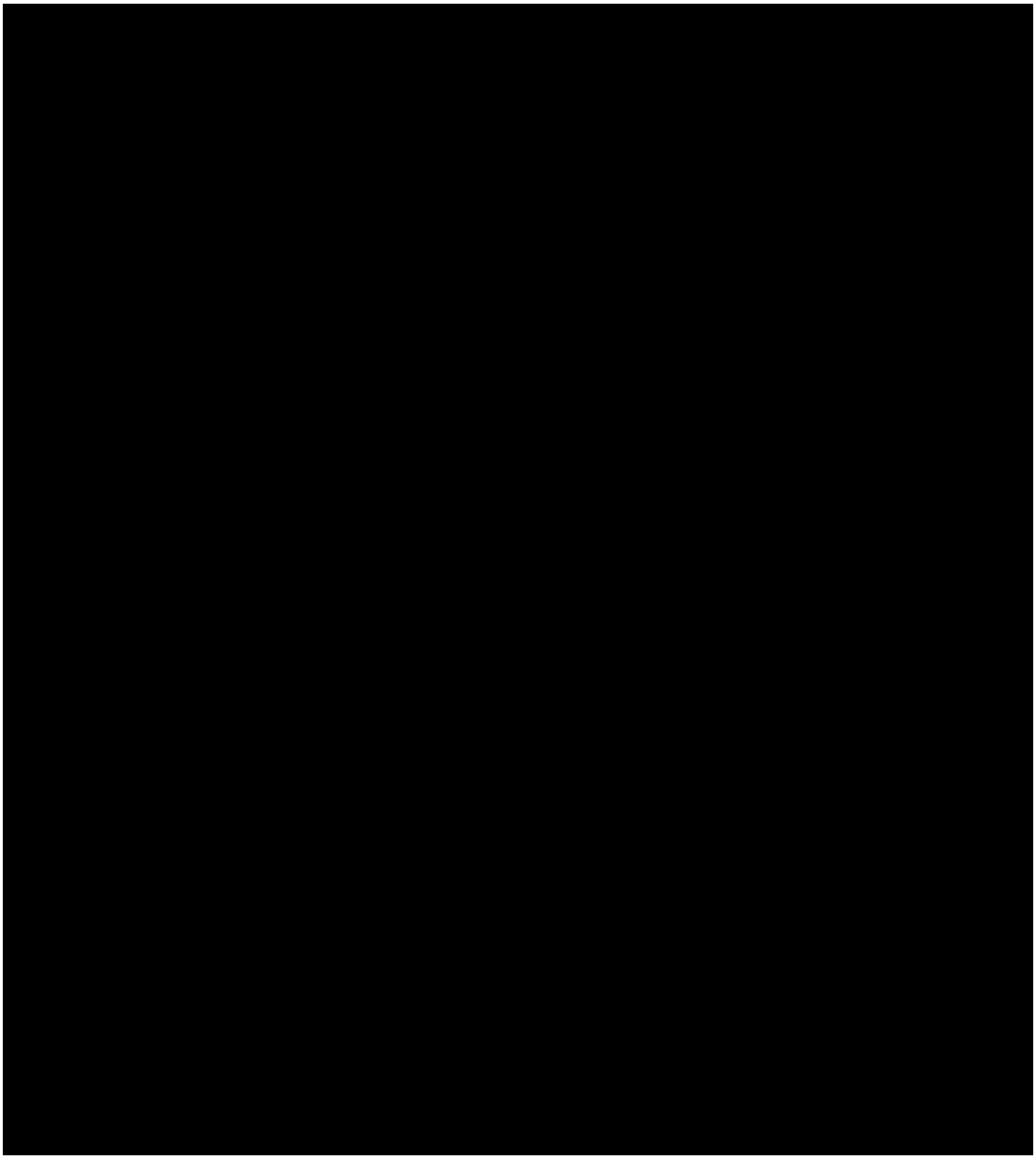

Figure 1-43 – Plot of USGS Produced Water Samples and [redacted] Well

Water samples of the injection interval will be obtained during drilling operations of the proposed injection well, and complete water analyses will be performed to establish baseline reservoir fluid conditions.

1.7 Baseline Geochemistry

1.7.1 Mineralogy

Approximate locations within depositional environments and regional studies of provenance were considered in constructing mineralogical composition estimates of the Upper, Middle, and Lower Miocene reservoirs. Samples of the Middle and Lower Miocene sediments transported by the Mississippi and Tennessee rivers from Appalachian and Cumberland Plateau provenances are plotted on QFL diagrams (Xu, 2022). Upper Miocene mineralogy was best estimated from qualitative descriptions of Louisiana coastal Upper Miocene sandstones (Gold, 1985). Quartz is the dominant mineral in these deltaic sand deposits, followed by feldspar. Both plagioclase and potassium feldspars are present, in an approximate 3:2 ratio (Gold, 1985).

Local variations of calcite and clay were best estimated from qualitative core descriptions of the [redacted]), located north of the AOR in [redacted] field. Only smectite clay at deposition was assumed. A linear trend line applied to a plot of smectite-to-illite ratios by depth, from analyses of Late Miocene and Pliocene shales in [redacted] field, was used to estimate the percentage of each clay mineral at the depths of the Miocene intervals (Totten, 2002). Table 1-7 is an approximate mineralogical composition by volume of the formations that constitute the injection interval, normalized to 100%.

The primary mineralogy of the upper and lower confining intervals is anticipated as clay, quartz, feldspar, and calcite. The clay percentage was estimated by the average Vshale over the confining intervals to be 80%. Calcite was included, as it is one of the most reactive minerals anticipated to be present in this mineral assemblage. The remaining composition was assumed to be similar ratios of the sediment present in the adjacent Miocene injection zones. Table 1-8 displays the approximated mineralogical composition of the [redacted] shales.

Table 1-7 – Estimates of injection-interval mineralogical composition by volume (%).

Interval	Quartz	Plagioclase	Kspar	Calcite	Smectite	Illite
[redacted]	[redacted]	[redacted]	[redacted]	[redacted]	[redacted]	[redacted]
[redacted]	[redacted]	[redacted]	[redacted]	[redacted]	[redacted]	[redacted]
[redacted]	[redacted]	[redacted]	[redacted]	[redacted]	[redacted]	[redacted]

Table 1-8 – Estimates of Confining Units' Mineralogical Composition by Volume (%)

Confining Unit	Smectite	Illite	Quartz	Plagioclase	Kspar	Calcite
[redacted]	[redacted]	[redacted]	[redacted]	[redacted]	[redacted]	[redacted]
[redacted]	[redacted]	[redacted]	[redacted]	[redacted]	[redacted]	[redacted]

1.7.2 Brine and Rock Inputs

The brine composition used for the injection simulations comes from a produced water sample (RFS ID No. 202206840-02) as described in *Section 1.6*. The sample was analyzed for a standard set of anions and cations as well as TDS, pH, resistivity, conductivity, and specific gravity. All analyses were conducted at a temperature of 60°F. The concentrations of cations and anions inputted into PHREEQC and the calculated molality values are shown in Table 1-9.

In practice, it is presumed that formation brines are in equilibrium with the host formations due to long residence times and limited reactive surface area in the pore space. In simulation studies, analyzing the equilibrium between the produced water and non-reservoir intervals (i.e., seals) provides insight into the reactivity of the reservoir formation brine and the non-reservoir interval away from the reservoir-seal interface. This equilibrium reaction is useful in assessing extreme upper bounds of water-rock reactivity. The results are also shown in Table 1-9.

Table 1-9 – Estimate of reservoir brine composition (column 1) and the equilibration of the brine composition with the seal formations.

PHREEQC Equilibrated Zone Brines			
	Produced Water RFS ID No. 202206840-02	**Upper Confining Zone**	**Lower Confining Zone**
Temperature (°C)	[redacted]		
pH			
Water Mass (kg)			
Al			
B			
Ba			
Br			
C			
Ca			
Cl			
Fe			
I			
K			
Li			
Mg			
Mn			
Na			
S			
Si			
Sr			
Ti			

The mineralogic composition of the confining zones as well as the reservoir zones were estimated as described in *Section 1.7.1*. The upper and lower confining zones are principally composed of clay and quartz; the upper reservoir interval is principally quartz with minor amounts of calcite, feldspars, and clay; and the lower reservoir interval is principally quartz with a significant amount of feldspar and some calcite (all displayed in Table 1-10).

Table 1-10 – Mineralogic Composition of the Confining and Reservoir Intervals

Zone Compositions	[redacted]
Water Mass (kg)	
Plagioclase (mol) as Albite	
Anhydrite (mol)	
Feldspar (mol) as Anorthite	
Calcite (mol)	
Chlorite (mol) as Chamosite-7A	
Dolomite (mol)	
Illite (mol)	
Potassium Feldspar (mol)	
Kaolinite (mol)	
Pyrite (mol)	
Quartz (mol)	
Siderite (mol)	
Smectite (mol)	

To model the injection process, an approximate gas composition was derived from current pipeline specifications. The pipeline gas is [redacted], with accessory gases and water making up the remaining [redacted]. While it is likely that this gas composition is more heterogenous than the final CO_2 injection stream, the reaction modeling is not highly sensitive to the accessory gasses ([redacted]), thus the simulations are representative of the expected reactions.

1.7.3 Rock-Brine-Gas Interaction

The interactions between the rock mineralogy, brine, and CO_2 gas injectate were modeled using PHREEQC batch reactions. In the batch reaction, a 1 cubic meter rock-brine system is injected with 1,000 moles of injection gas. The simulation holds the formation pressure and temperature constant at values relevant for each interval, and calculates the solution and dissolution of mineral phases over ten equilibration steps. Simulations were run for the upper and lower confining formations as well as the upper and lower reservoir intervals.

The equilibrated brine compositions for the reservoir rock-brine-gas systems are shown in Table 1-11(A). The simulation for the upper reservoir layer shows that the formation brine loses mass due to the precipitation of quartz, dolomite, kaolinite, and siderite, while calcite and albite are dissolved. The simulation of the lower reservoir layer shows that the formation brine loses mass because of the precipitation of kaolinite, calcite, and dolomite, while anorthite, quartz, and illite are dissolved.

The equilibrated brine compositions for the confining layer rock-brine-gas systems are shown in Table 1-11(B). The simulation for the upper confining layer shows that the formation brine gains mass due to the dissolution of calcite and k-feldspar (kspar), while the precipitation of quartz, siderite, illite, albite, and dolomite occurs. The simulation of the lower confining layer shows that the formation brine loses mass due to the precipitation of quartz, dolomite, and kaolinite while the dissolution of illite, calcite, and anorthite occurs. The modest mass gain for the upper seal brine, coupled with precipitation of assorted minerals including clays, will have a net neutral effect on seal capacity—due to pore-occlusion and a limited amount of minerals available for dissolution. The modeled net precipitation of minerals for the lower confining layer suggests that seal capacity will increase due to pore-occlusion processes.

Table 1-11 – Upper and Lower Reservoir (A) and Confining Zone (B) Brine Outputs

(A) Equilibrated Reservoir Rock-Brine-Gas			
	Upper Reservoir	Middle Reservoir	Lower Reservoir
Temperature (°C)			
pH			
Water Mass (kg)			
Al			
B			
Ba			
Br			
C			
Ca			
Cl			
Fe			
I			
K			
Li			
Mg			
Mn			
Na			
S			
Si			
Sr			
Ti			

(B) Equilibrated Seal Rock-Brine-Gas		
	Upper Seal	Lower Seal
Temperature (°C)		
pH		
Water Mass (kg)		
Al		
B		
Ba		
Br		
C		
Ca		
Cl		
Fe		
I		
K		
Li		
Mg		
Mn		
Na		
S		
Si		
Sr		
Ti		

1.8 Fault Seal Analysis

The Fault Seal Analysis was conducted jointly for most of the normal faults within the area. The Shale Gouge Ratio (SGR) based analysis provides useful information about fault properties and estimation of their sealing capacities in addition to a permeable-impermeable rocks juxtaposition captured in the geostatic model and typically accounted for at the dynamic modeling stage. To

estimate fault sealing capacity, the SGR, fault zone entry capillary pressure (FZP), and faults' permeability were calculated.

While accounting for the lithological juxtaposition, the SGR is an important parameter used to estimate the amount of clay within the fault gouge, as the very-fine phyllosilicates result in very small pore-throats, leading to high FZP and low permeabilities within the fault zone (Yielding, 2002). The accuracy of the SGR estimations certainly depends by quality of input data, but overall, the SGR "has proven to be a robust and quantitative predictor of fault seal in mixed clastic sequences" (Yielding, 2002). The SGR and SGR equation (Yielding et al., 1997) is a widely accepted method used to estimate the amount of clay within the fault gouge (Figure 1-44).

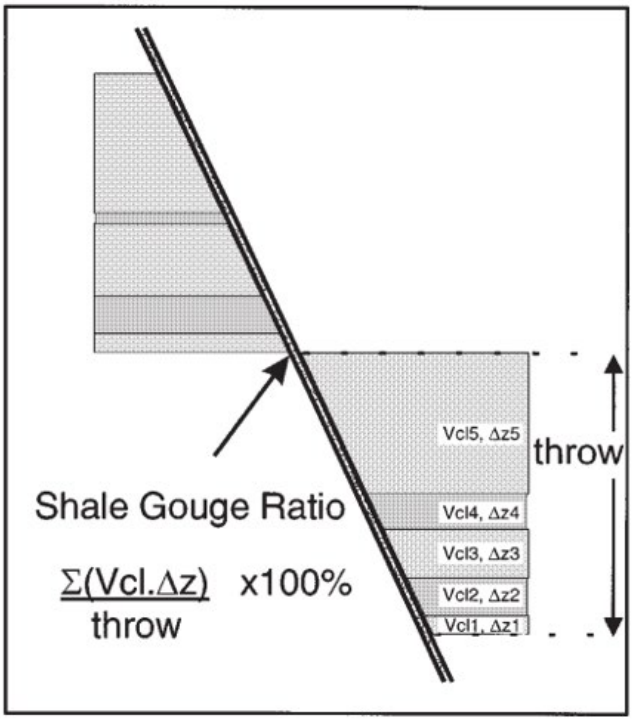

$$\text{SGR} = \frac{\Sigma\left[\left(\text{Zone thickness}\right)\times\left(\text{Zone clay fraction}\right)\right]}{\text{Fault throw}} \times 100\%$$

Figure 1-44 – Shale Gouge Ratio conceptual diagram and equation. Calculation for a sequence of reservoir zones; Δz is the thickness of each reservoir zone and Vcl is the clay volume fraction in the zone (Yielding et al., 1997).

The SGR has been shown to be an effective qualitative predictor for sealing vs. non-sealing faults in hydrocarbon systems. SGR data from the fault-bounded reservoirs of both sealing and non-sealing faults show that SGR values of approximately 15-20% are the typical cutoff for sealing vs. non-sealing faults (e.g., Bretan et al., 2003; Meckel and Trevino, 2014). [redacted].

SGR and other calculated parameters were analyzed for the injection and upper confining intervals, predicting their horizontal and vertical sealing capacities. The sealing capacity of the upper confining interval and penetrating faults are of particular importance. Figure 1-45 depicts the facies distribution within the upper confining interval, [redacted]. This significant shale presence serves as the foundation for the consistent behavior observed in both the interval and penetrating faults.

Figure 1-45 – Facies distribution within the upper confining interval and corresponding histogram, showing that [redacted] of this interval is presented by shales. Histogram codes represent the following facies: 1 – shale; 2 – siltstone; 3 – distal; 4 – proximal; 5 – axial sandstones.

Figure 1-46 shows the histograms of SGR distribution for the upper confining and injection intervals, accompanied by the 3D view at the fault planes with the SGR values distribution along them.

Figure 1-46 – Histograms and corresponding 3D inserts of the calculated Shale Gouge Ratio (SGR) distribution along the faults within the model for (a) upper confining and (b) injection intervals.

FZP calculations were then performed to identify if the capillary entry pressure of the fault gouge was reached from the influence of the injected CO_2. The classic SGR equation for hydrocarbon systems (Bretan et al., 2003) used to calculate the FZP using SGR and fault rock strength is

$$FZP\ or\ P_C\ (bar) = 10^{\left(\frac{SGR}{27} - C\right)}$$

Where: C is fault rock strength, which varies with depth.

The C values are as follows: C = .5 for burials depths less than 9,850'; C = .25 for burial depths between 9,850-11,500'; and C = 0 where burial depths exceed 11,500' (Bretan P. Y., 2003). However, since the wetting properties of various rock-forming minerals are different for CO_2 and hydrocarbons, this equation needs modification. The most recent work to address this difference was done by Karolyte et al. (2020). As noted by Bretan et al. (2022), proposed modifications lead to FZP reduction of about [redacted] off of the classic FZP results. Thus, the correction multiplier of [redacted] was applied to the resulting FZP value as well as a unit conversion from bar to psi. Figure 1-47 shows calculated threshold FZP values vs. SGR for the upper confining and injection intervals. The threshold lines represent the maximum capillary entry pressure that can be supported at a specific SGR value at certain ranges of the burial depth.

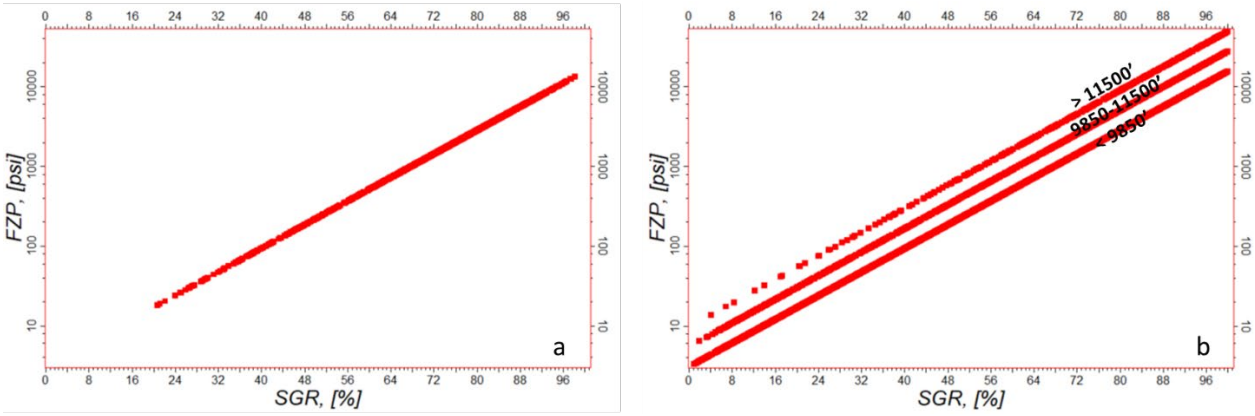

Figure 1-47 – Fault zone entry pressure (FZP) vs Shale Gouge Ratio (SGR) for (a) upper confining and (b) injection intervals. Lines are ''seal-failure envelopes'' (or thresholds) that represent the maximum capillary entry pressure that can be supported at a specific SGR value at certain ranges of the burial depth.

Another valuable application of SGR calculations lies in estimating fault permeability, particularly when capillary pressure differences are absent, and only a single fluid type (brine) is present on both sides of the fault. This assessment becomes crucial in such scenarios. Different general equations have been proposed and used for this. Permeability calculations from SGR using Jolley et al., 2007, equation have been applied here. Figure 1-48 shows fault zone permeabilities vs SGR for upper confining and injection intervals. Figure 1-49 shows the histograms of permeability distribution for the upper confining and injection intervals and accompanied by the 3D view at

the fault planes with the permeability values distribution along them. [redacted]

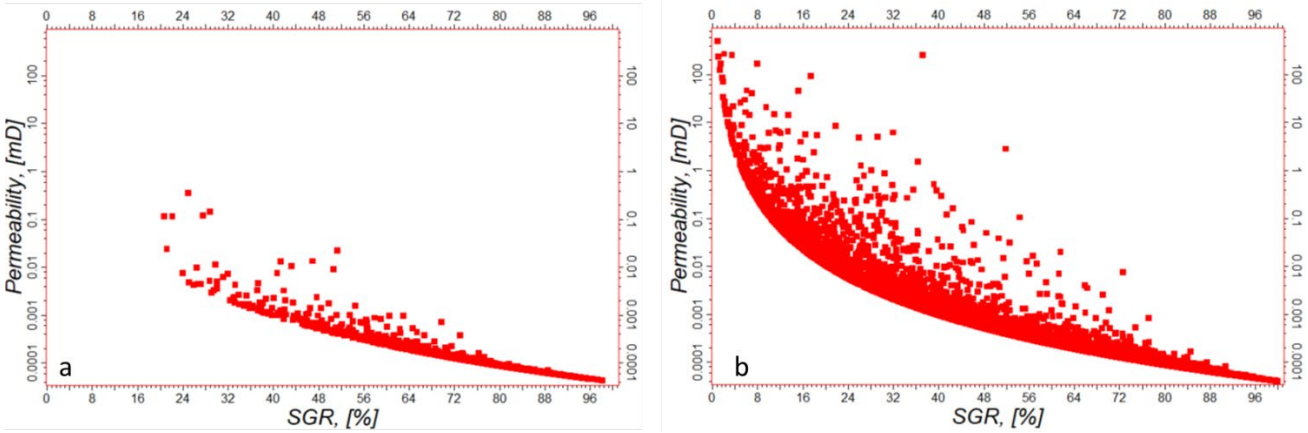

Figure 1-48 – Fault zone permeabilities vs. Shale Gouge Ratio (SGR) for (a) upper confining and (b) injection intervals.

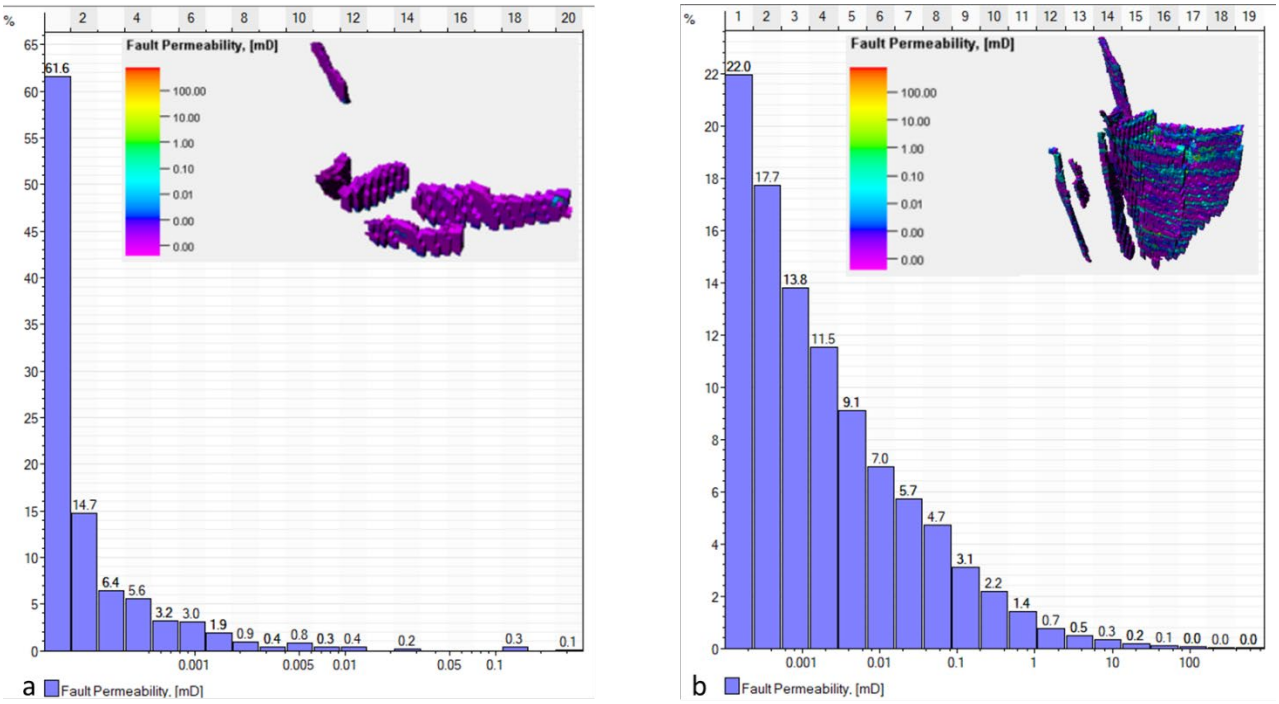

Figure 1-49 – Histograms and corresponding 3D inserts of the calculated fault permeability distribution within the model for (a) upper confining and (b) injection intervals.

The Shale Gouge Ratio based analysis provides useful information about fault properties and estimation of their sealing capacities in addition to a permeable-impermeable rocks juxtaposition captured in the geostatic model and typically accounted for at the dynamic modeling stage. Three parameters provided by the fault seal analysis are shale gouge ratio, fault zone entry capillary pressure, and fault permeability at the present/static conditions. These calculated parameters indicate that at present conditions the fault planes are characterized by a moderately high to high sealing capacity for the injection and upper confining intervals, respectively. [redacted]. Notice that in the presence of only one fluid (brine) and, therefore, lack of the capillary pressure within the fault zones, permeabilities may play a more important role to estimate fault sealing properties. [redacted]. SGR and permeability define the fault behavior under present conditions and, along with FZP, set thresholds for the fault behavior under changing dynamic conditions.

1.9 Hydrology

The hydrogeologic framework of southeastern Louisiana is generally characterized as a shallow alluvial aquifer and an interconnected series of deeper aquifers that dip and thicken toward the Gulf of Mexico. These aquifer systems are primarily recharged by precipitation, in eastern Louisiana and western Mississippi, that percolates down through the geologic section. Once in the system, freshwater continues to flow downdip toward the gulf at rates of several tens of feet to hundreds of feet per year (Lindaman & White, 2021; Griffith, 2003).

The three deep aquifer systems in Iberville Parish—the Jasper equivalent, the Evangeline equivalent, and the Chicot equivalent—are comprised of a complex sequence of interbedded clay, sand, and gravel with aquifers occurring as lenticular sand and gravel deposits. These deposits typically contain a high degree of heterogeneity, can terminate bluntly, and are hydraulically connected to overlying and underlying deposits. Each aquifer system is comprised of a series of deposits that coalesce within clay-rich confining intervals, as depicted in Figure 1-51 (page 84) (Lindaman & White, 2021; Griffith, 2003). The stratigraphic column in Figure 1-50 (page 82) clarifies individual sand nomenclatures of each aquifer system, and Figure 1-52(A) (page 85) illustrates their freshwater extents relative to the proposed White Castle Project location. The thickness of the Jasper equivalent aquifer system ranges from 780’ to 1,350’, the thickness of the Evangeline equivalent aquifer system ranges from 150’ to 2,000’, and the thickness of the Chicot equivalent aquifer system ranges from 75’ to 1,100’, with thickness increasing towards the south (Griffith, 2003).

Although freshwater production has been reported for several aquifers in Iberville Parish, Harvest Bend CCS only anticipates encountering freshwater within the Mississippi River alluvial aquifer and the Chicot equivalent aquifer system. These formations represent the anticipated

freshwater column near the White Castle Project and tend to be in direct communication with each other. This agrees with published regional literature, which report that deep aquifer systems only produce freshwater in northern Iberville Parish, north of Baton Rouge and the Baton Rouge fault system, where depths are shallower and saltwater encroachment poses less of an issue to water quality. This is also supported by regional studies that verify the Baton Rouge fault corresponds with a quick shift in the depth of the lowest USDW, which is substantially deeper north of the fault (Chamberlain, 2012; Griffith, 2003).

The schematic cross section depicted in Figure 1-51 utilized wireline logs to illustrate the stratigraphic relationship of freshwater and saltwater bearing formations relative to Baton Rouge and the Baton Rouge fault. The figure suggests that a significant majority of deep aquifer systems are interpreted to contain saline water near the proposed White Castle location. Offset open hole logs from the [redacted]. One such open-hole log is included in Figure 1-53, with blue shading to highlight induction values greater than 3 ohms, following the LDNR-suggested methodology to determine the base of the USDW from open-hole logs. Cross sections were generated depicting the USDW in relation to the injection interval. These can be found in *Appendices B-16* and *B-17*. Additionally, a USDW structure map was generated through USDW picks within offset wells and is represented in *Appendix B-18*.

The Mississippi River alluvial aquifer, commonly referred to as the "Mississippi River Valley alluvial aquifer," is a tremendous freshwater resource for southeastern Louisiana and represents the primary freshwater aquifer supplying Iberville Parish. The aquifer consists of a largely uninterrupted mass of sand deposited into an incised valley of the underlying Chicot formation (Lindaman & White, 2021; Griffith, 2003). The aquifer is overlain by 75' to 100' of silt and clay that functions as a surficial confining unit. The thickness of the aquifer ranges from 125' to 300' in southeastern Louisiana and generally thickens to the southeast. Figure 1-52(B) depicts the freshwater extents of the aquifer and illustrates alluvial fill primarily developed west of the Mississippi River (Griffith, 2003).

In 2014, Iberville Parish withdrew an average of 589.87 million gallons of water per day (Mgal/d), sourced from a combination of groundwater (30.86 Mgal/d) and surface water (559.01 Mgal/d) resources. The majority of freshwater withdrawn was provided by surface water from the Mississippi River (551.28 Mgal/d), with some contribution from the Lower Grand River (0.58 Mgal/d) and miscellaneous streams (7.15 Mgal/d). Groundwater production in Iberville Parish was restricted to shallow aquifers that range from Quaternary to Miocene in age. These formations include the Mississippi River alluvial aquifer (26.72 Mgal/d), the Chicot equivalent aquifer system (3.68 Mgal/d), the Evangeline equivalent aquifer system, and the Jasper equivalent aquifer system (0.46 Mgal/d) (Lindaman & White, 2021). Figure 1-50 displays the hydrogeologic units of Louisiana as published by Collier and Sargent (2015). Formations with freshwater potential at the White Castle location are outlined in blue, and formations anticipated to be saltwater bearing are outlined in red.

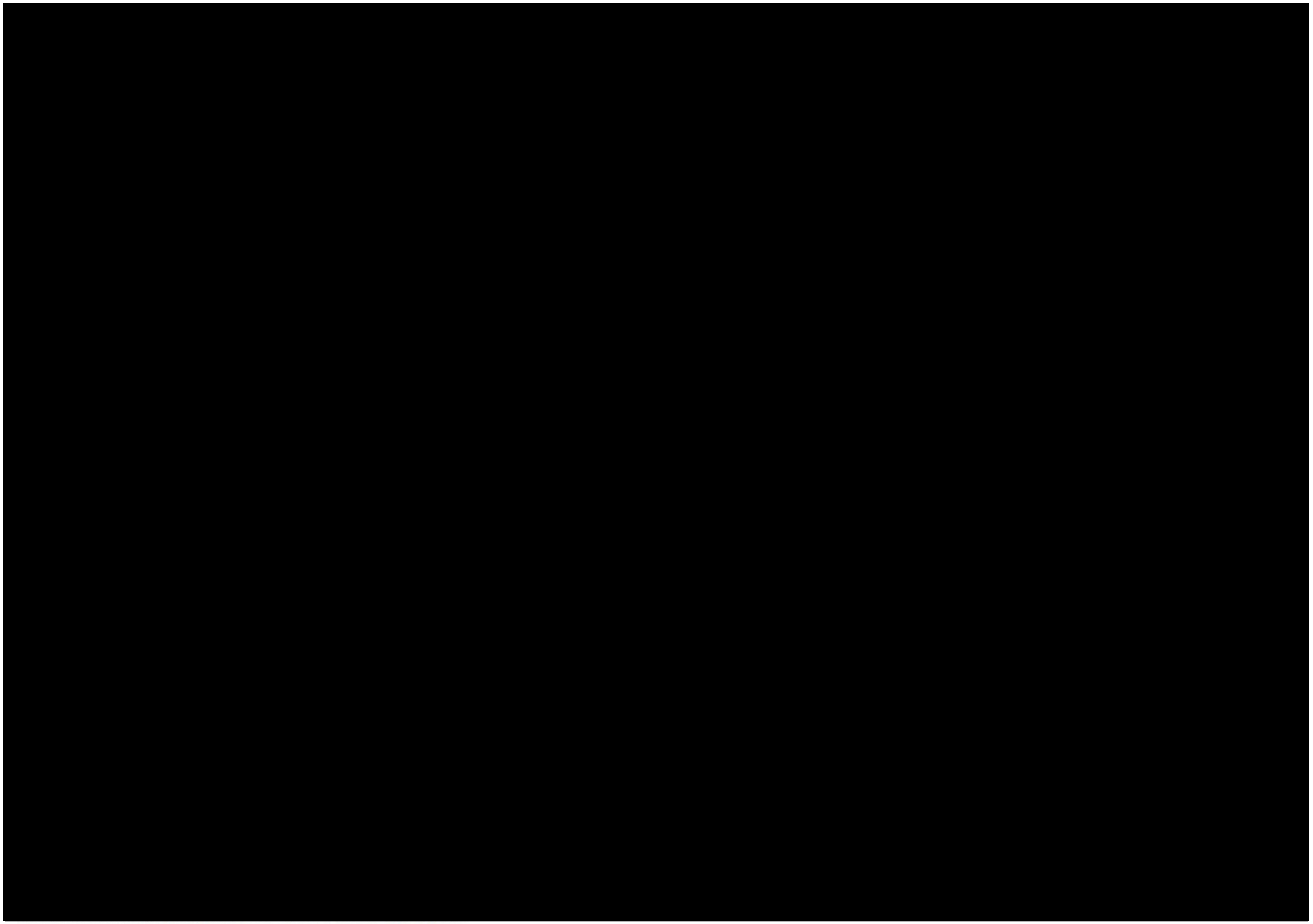

Figure 1-50 – Hydrogeologic units of Louisiana, with formations with freshwater potential outlined in blue (modified from Collier & Sargent, 2015).

In 2017, there were 403 active Iberville Parish water wells screened in the Mississippi River alluvial aquifer, with well depths ranging from 30' to 733' below surface. Water quality samples from the Mississippi River alluvial aquifer contained a medium hardness of 170 mg/L, classifying it as hard. Water samples exhibited variable iron concentrations that range from 30 to 16,000 micrograms per liter (µg/L) with a median of 1,400 µg/L. As a result, approximately 87% of samples analyzed exceeded the EPA's Secondary Maximum Contaminant Level (SMCL) of 300 µg/L for iron.

Water analysis from aquifer samples also indicated that 7% of chloride samples exceeded the EPA's SMCL concentration of 250 mg/L for chlorides. Water levels reported from 18 wells screened in the parish ranged from 7' below to 25' above sea level and indicate a general flow direction of south to southeast. This is substantiated by a potentiometric surface map generated by the USGS in 2016 (Figure 1-54, page 87; *Appendix B-20*), which shows a general flow direction to the south with contours ranging from 10' to 20' around the proposed White Castle location. Additional support is provided in *Appendix B-19*, the *Altitude of the Potentiometric Surface in the Mississippi River Valley Alluvial Aquifer* published by the USGS in the Spring of 2020. Historic water data indicates that the water level of the Mississippi River alluvial aquifer is also affected by the stage of the Mississippi River, with fluctuations increasing along with proximity to the river (Lindaman & White, 2021).

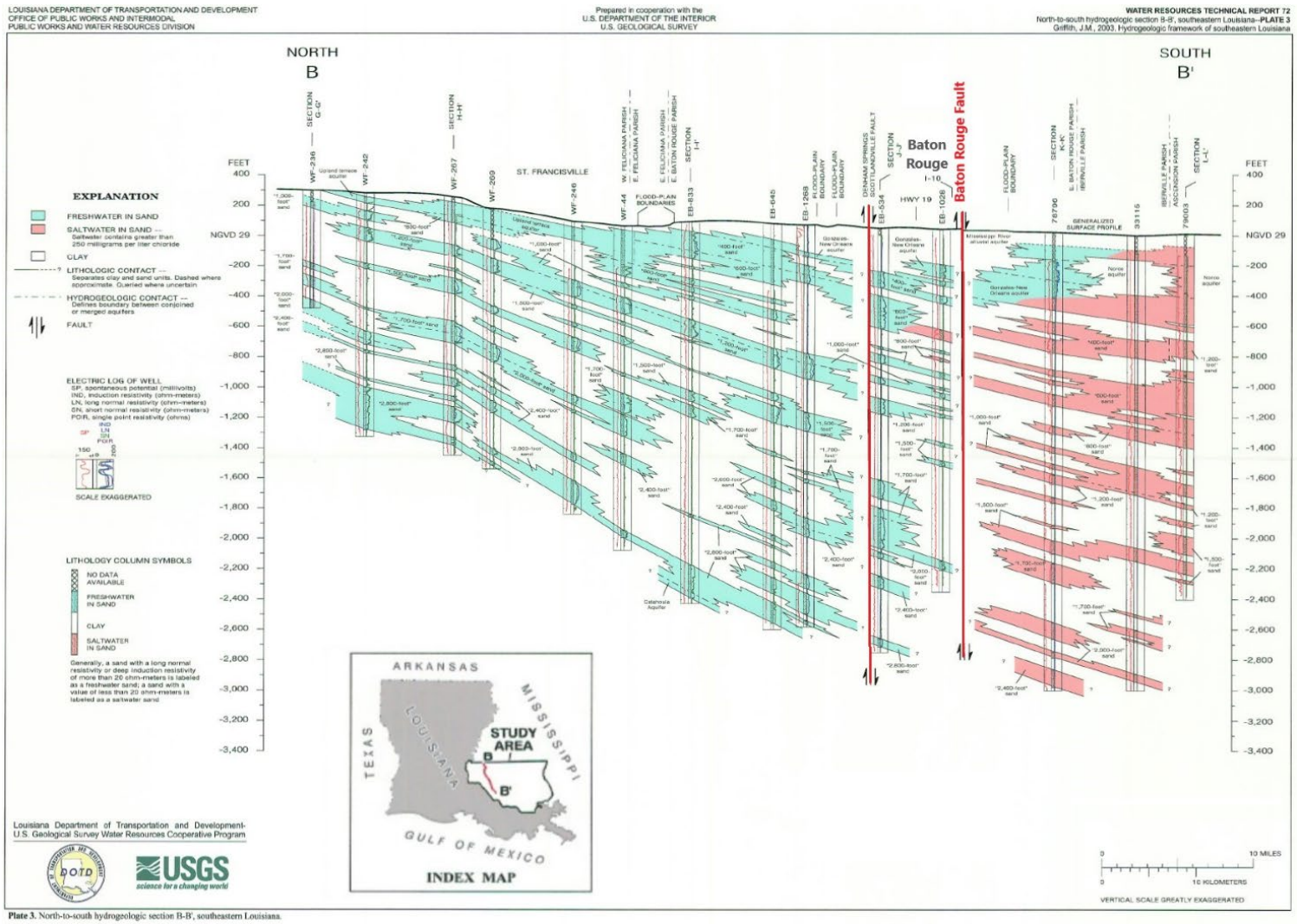

Figure 1-51 – North-south oriented cross section depicting USGS-identified aquifers relative to offset faulting. Freshwater aquifers are indicated in blue, brackish aquifers in red, and mudstones in white. Note: The Baton Rouge fault represents an interpretated boundary of freshwater to the north and brackish water to the south (modified from Griffith, 2003).

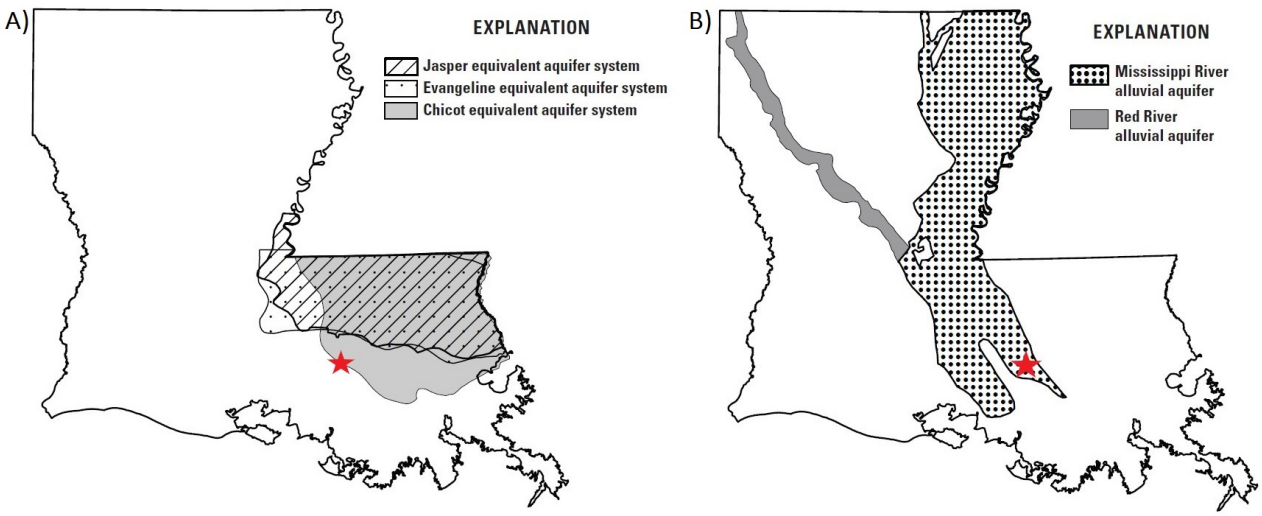

Figure 1-52 (A) – Approximate areal extent of Jasper, Evangeline, and Chicot equivalent aquifer systems. Figure 1-52 (B) – Approximate areal extent of Mississippi River and Red River alluvial aquifers. The red star represents the approximate White Castle Project location (modified from Collier & Sargent, 2015).

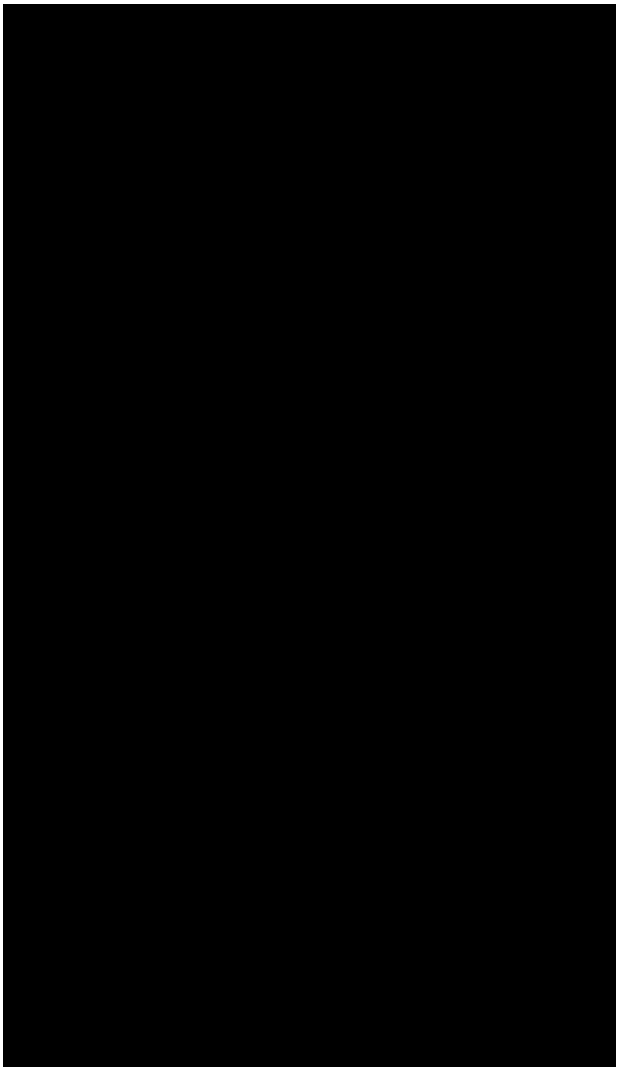

Figure 1-53 – Open-hole log and USDW determination from offset well ( ). The deep induction curve is shaded blue for values >3 ohms to illustrate the state-suggested determination method.

Figure 1-54 – Mississippi River alluvial aquifer potentiometric-surface map for Atchafalaya, Deltaic, and Chenier Plain regions of the Mississippi alluvial plain
(McGuire, Seanor, Asquith, Kress, & Strauch, 2019).

1.10 Site Evaluation of Mineral Resources

The proposed CO_2 storage site lies [redacted], a structural high centered within a depleted oil field. Given its proximity to a producing field, the likelihood of encountering hydrocarbons at the storage site was assessed. Nine wells southeast and downdip from the dome, with representative geology to the storage site, were evaluated (Table 1-12). All nine were dry holes, abandoned after drilling (Table 1-12 and Figure 1-55, page 89). Each of these dry holes did not evidence hydrocarbons as they drilled to anomalously high depths (greater than 12,500') and straight through the targeted injection intervals. Resistivity logs from these wells corroborate the saline nature of the Miocene storage aquifers beneath the injection site. Therefore, for purposes of this permit application, the dry holes indicate the lack of developable hydrocarbon resources in the Miocene sands formation within the proposed storage area.

Table 1-12 – Dry Hole Wells in the White Castle Area

Well Serial	API Number	Well Name	TD	Final Status	Distance from Injector (miles)
[redacted]	[redacted]	[redacted]	[redacted]	[redacted]	[redacted]
[redacted]	[redacted]	[redacted]	[redacted]	[redacted]	[redacted]
[redacted]	[redacted]	[redacted]	[redacted]	[redacted]	[redacted]
[redacted]	[redacted]	[redacted]	[redacted]	[redacted]	[redacted]
[redacted]	[redacted]	[redacted]	[redacted]	[redacted]	[redacted]
[redacted]	[redacted]	[redacted]	[redacted]	[redacted]	[redacted]
[redacted]	[redacted]	[redacted]	[redacted]	[redacted]	[redacted]
[redacted]	[redacted]	[redacted]	[redacted]	[redacted]	[redacted]
[redacted]	[redacted]	[redacted]	[redacted]	[redacted]	[redacted]

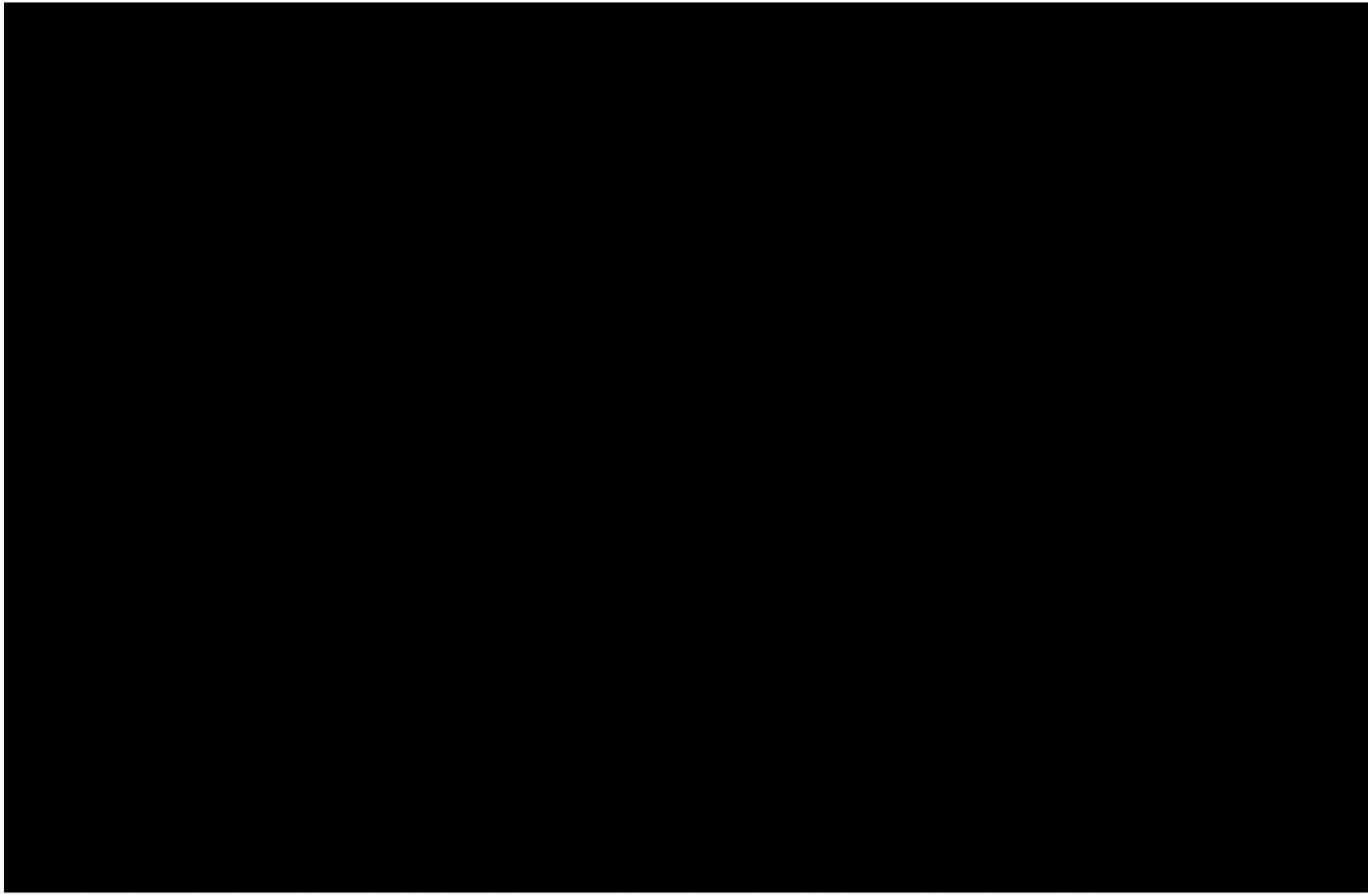

Figure 1-55 – Dry and Abandoned Wells and Producing Wells in the White Castle Area

In the 1920s, the [redacted] was identified using seismic refraction data. Soon thereafter, hydrocarbons were discovered upon drilling the [redacted]) well. A piercement structure and rather cylindrical, the top of the [redacted] is located approximately 2,300' below surface. Faults centered atop the dome trapped hydrocarbon accumulations in Pliocene sands, above the proposed CO_2 injection zone. Moving away from the center of the dome, hydrocarbon accumulations were found trapped in stratigraphically lower Miocene sands between faults radiating from the dome. These sands are age-equivalent to the downdip CO_2 injection intervals. Moving away from the dome, sub-injection Oligocene sand discoveries predominantly produce gas beneath salt overhangs.

[redacted] Approximately 600 wells have been drilled there, of which 96% have been plugged and abandoned. As of late 2022, 25 wells produce and most generate less than 5 bbloe/d with water cut greater than 99%. The highest active producers are withdrawing primarily gas from those Oligocene sands beneath a salt overhang along the northern flank of the dome. Production from these wells is not expected to impact planned CO_2 injection activity, or vice versa.

As mentioned, there are approximately 25 actively producing wells in the [redacted] field. Detailed analysis of log and completion data indicates that 11 of the 25 (Table 1-13) were determined to produce from the targeted injection interval—of which five were deemed to be low impact because of their location around the dome. Therefore, the six closest producing wells along the southeast side of the dome were further evaluated. These six wells produce from the proposed injection interval but are at a sufficient distance (4.65 miles) such that injection activities will likely not communicate. Additionally, facies distributions as determined from the 3D seismic indicate that sand deposition was diverted around the dome during Mid to Late Miocene halokinesis. [redacted] In fact, all six of these wells can be categorized as "stripper wells," in that maximum daily production does not exceed 15 barrels of oil (cumulative for all wells) or 90 thousand cubic feet of gas (Mcf). Additionally, each of these wells produces substantial water (>95% water cut).

Lastly, the nature of these Miocene reservoirs is indicative of stratigraphic and structural compartmentalization. Not only is the likelihood of these hydrocarbon accumulations being communicative to the downdip injection site low, but the maximum carbon front extent is [redacted] from the nearest production, which further minimizes potential impact.

Table 1-13 – Productive Wells in the White Castle Area

Well Serial	API No.	Well Name	TD	Perf Upper	Perf Lower	Current Status	Producing Formation	Distance from Injector (miles)
[redacted]								

The [redacted] is also used for its mineral resources, whereby solution-mining operations supply liquid brine for industrial and chemical operations near Baton Rouge. Salt caverns formed by this activity may be used for storage in the future. The solution mining

operations do not interfere with this project's targeted injection interval as these wellbores do not penetrate the targeted CO_2 injection interval.

1.11 Seismic History

An important consideration in the design and development of all new injection-well projects is the determination for the potential of injection activities to induce a seismic event. This section complies with the requirements in SWO 29-N-6 **§3607.C.2.c** [40 CFR **§146.82(a)(3)(v)**]. A four-step approach is conducted, including:

1. Identification of historical seismic events within proximity to the project,
2. Faulting and determination of operational influences of nearby faults,
3. Performance of a fault-slip potential (FSP) simulation model, and
4. Seismic hazard.

1.11.1 Identification of Historical Seismic Events

To conduct the historical seismic data investigation, an AOR must be established, which is defined as a 5.6-km radius[1] or a 98.5-square-km area surrounding the project. This data is based on seismographic recordings from a global network of seismological stations. According to the USGS Earthquake Archive Search, no seismic events greater than 2.0 magnitude[2] were recorded within the 5.6-km radius of the WC IW-B No. 001 and No. 002 location (Figure 1-56). Further research was conducted on the National Centers for Environmental Information (NCEI), Texas Seismological Network Earthquake Catalog (TexNet), and Volcano Discovery seismic catalogs, which supported the USGS results. Although Louisiana is in an area of low seismic risk, a few earthquakes caused by natural seismicity or induced seismicity have occurred in the state, shown in Figure 1-57 (page 94). [redacted]

[1] The FSP seismicity review radius was established based on local geology and the model extent of the plume.
[2] The magnitude of an earthquake is reported using the Richter scale, which measures the amount of energy (amplitude) generated at the source of an earthquake.

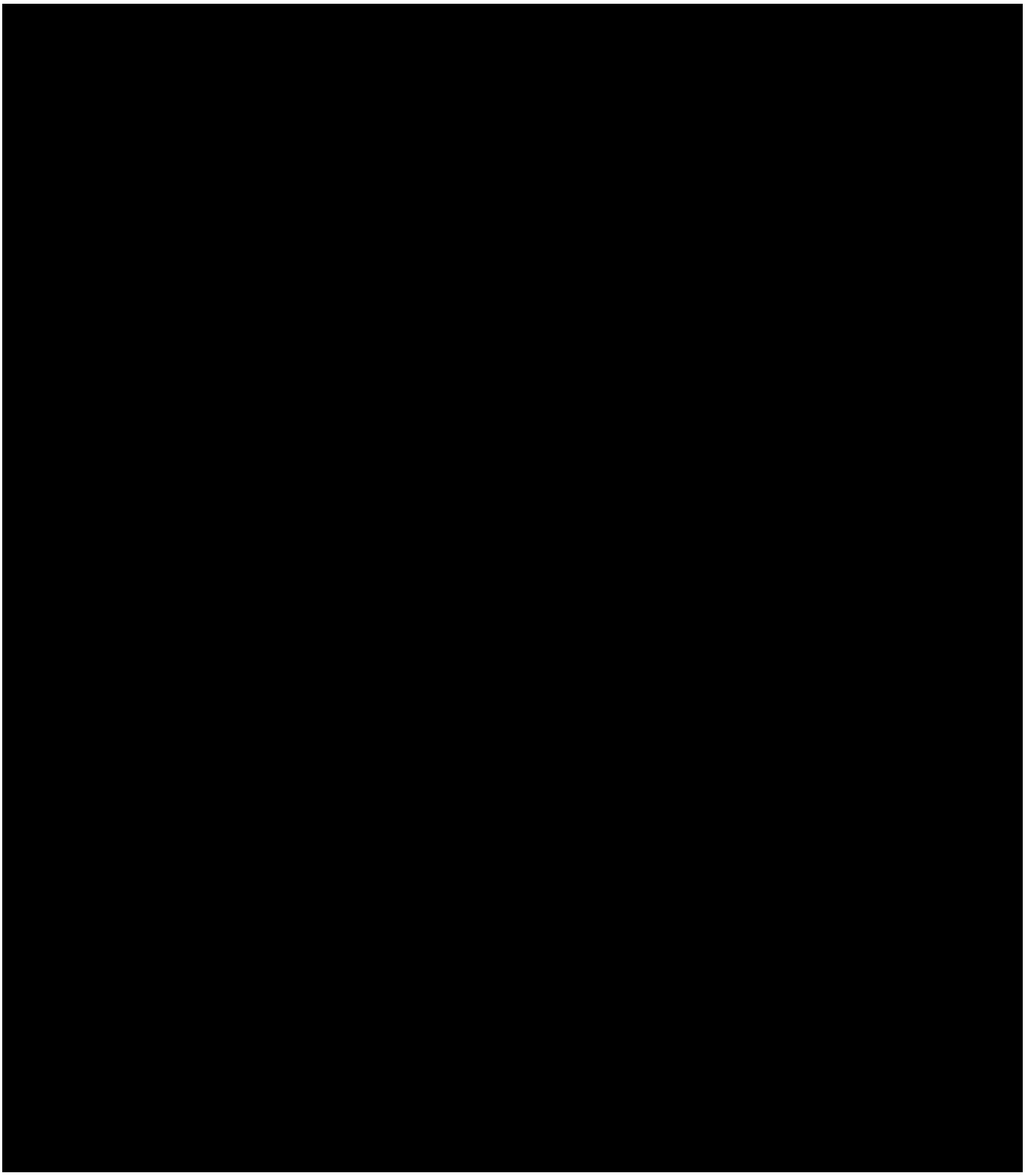

Figure 1-56 – Earthquake Search Parameters and Results from USGS Website

Figure 1-57 – All USGS-Registered Earthquakes in Inland Louisiana.
The red star is the location of the proposed well, the red circles are the 5.6 km area of interest, and the green dot is the closest earthquake.

1.11.2 Faults and Influence

The USGS has developed a database with detailed information on faults and related folds across the United States. EPA regulations require that a complete understanding of the extent and location of the resultant injection plume be determined and identified. Regionally, the USGS catalogs the faults in southwest Louisiana as "Class B" (Figure 1-58), as most of the faults are in sediments and poorly lithified rocks unable to sustain the forces necessary for the propagation of large seismic ruptures that could result in harmful ground motions. It is likely that the post-rift sequence and its band of normal faults along the Gulf of Mexico margin are mechanically

separated from the underlying crust, reducing the risk of a significant earthquake[3] (Crone & Wheeler, 2000). *Section 2 – Carbon Front Model* discusses CO_2 and pressure plume results, demonstrating that multiple faults are adjacent to, WC IW-B No. 001 and No. 002 injection operations. An FSP model was conducted to comply with EPA regulations.

Figure 1-58 – USGS Quaternary Fault and Fold Database of Louisiana and Location of the Proposed Project (indicated by the red star) (USGS U.S. Quaternary Faults, 2023).

1.11.3 Fault-Slip Potential Model

The FSP software provides an initial approximation of the cumulative likelihood of a known fault to exceed Mohr-Coulomb slip criteria due to fluid injection. As additional reservoir data is collected, models will be updated and induced seismicity potential will be further evaluated. It is critical to account for pressure variations at the prospective site to prevent faults from reactivating or the seal from being hydraulically fractured (Meckel & Trevino, 2014). Because faults were observed near the anticipated carbon and pressure front extents, but no historical seismic activity data was found in the study area, the projected induced seismic risk is assumed

[3] The USGS defines a "significant" earthquake as one with a significance >600. This number is derived by magnitude, number of "Did You Feel It" responses, and Prompt Assessment of Global Earthquakes for Response (PAGER) alert level.

to be low. Nevertheless, an FSP model was completed. The results and data used, including assumptions—plus uncertainty—are discussed in *Appendix I*. The FSP demonstrated a low probability of injection-induced seismicity.

1.11.4 Seismic Hazard

The USGS 2018 National Seismic Hazard Model (NSHM) Project and derived maps are recommended by the EPA as tools to assess seismic hazards. This model integrated and updated the 2014 NSHM including fault models, seismic catalogs, ground motion models, soil amplification factors, amplified shaking estimates of long-period ground motions, population density, and seismic hazard calculation. The 2018 Modified Mercalli Intensity (MMI) hazard map, with a 2% probability of exceedance in 50 years for a firm rock site, predicts that southern Louisiana will most likely encounter a class V[4] earthquake. The AOI is in the Class V extent, as shown in Figure 1-59. Figure 1-60 illustrates a 100-year prediction, in which population density is considered, and shows that southern Louisiana has a 4%–19% chance of having a VI[5] earthquake. In terms of 10,000 years, Figure 1-61 (page 98) depicts fewer than two damaging earthquakes[6] to occur in southern Louisiana. Based on the NSHM and the location of the proposed project, some earthquakes could occur in the future. However, the shake will be light to strong, causing furniture to be moved, and minor[7] damage might occur to structures. In terms of natural hazards[8], Iberville Parish is considered "Low" based on the National Risk Index, as hurricanes, landslides, riverine flooding, and tornados could occur, as Figure 1-62 (page 99) also depicts (National Risk Index FEMA, 2023).

Through analysis, it is very unlikely for a class VI MMI earthquake[9] to occur at the proposed location, based on NSHM, regional geology, historical seismic events, and natural hazards.

[4] Note: The Modified Mercalli Intensity (MMI) scale ranges from I to XII. The following descriptions, starting here with "Class V" and continuing into the next five footnotes, are from the Public Domain USGS Earthquake Hazards Program (originally abridged by Wood and Neumann, 1931). Class V. "MODERATE; felt by nearly everyone; many awakened: some dishes and windows are broken. Unstable objects are overturned. Pendulum clocks may stop."
[5] Class VI. "STRONG; felt by all, and many are frightened. Some heavy furniture is moved; a few instances of fallen plaster occur. Damage is slight."
[6] Damaging earthquake shaking; meaning a level VI or higher earthquake causing some structures failure.
[7] Minor damage; structural stable building, but some fallen plaster could occur.
[8] Natural Hazard; 18 natural hazards: Avalanche, Coastal Flooding, Cold Wave, Drought, Earthquake, Hail, Heat Wave, Hurricane, Ice Storm, Landslide, Lightning, Riverine Flooding, Strong Wind, Tornado, Tsunami, Volcanic Activity, Wildfire, and Winter Weather.
[9] Class IX. "Violent; damage is considerable in specially designed structures; well-designed frame structures are thrown off-kilter. Damage is great in substantial buildings, with partial collapse. Buildings are shifted off foundations. Liquefaction occurs. Underground pipes are broken."

Figure 1-59 – Total mean hazard maps for 2% probability of exceedance in 50 years, with the red star indicating the location of the proposed project (Petersen, et al., 2019, p. 33).

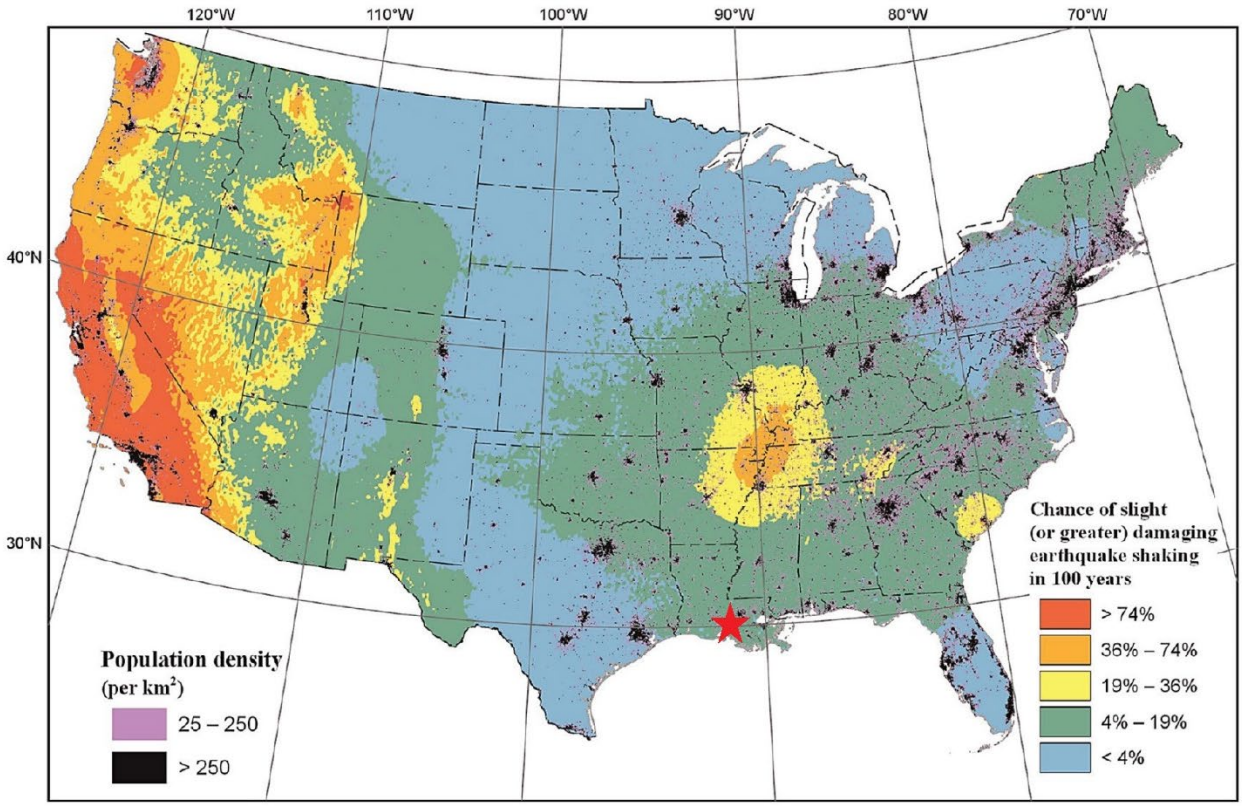

Figure 1-60 – Location of the proposed project (indicated by red star), population density, and the risk of a class VI earthquake shaking in 100 years (Petersen, et al., 2019, p. 7).

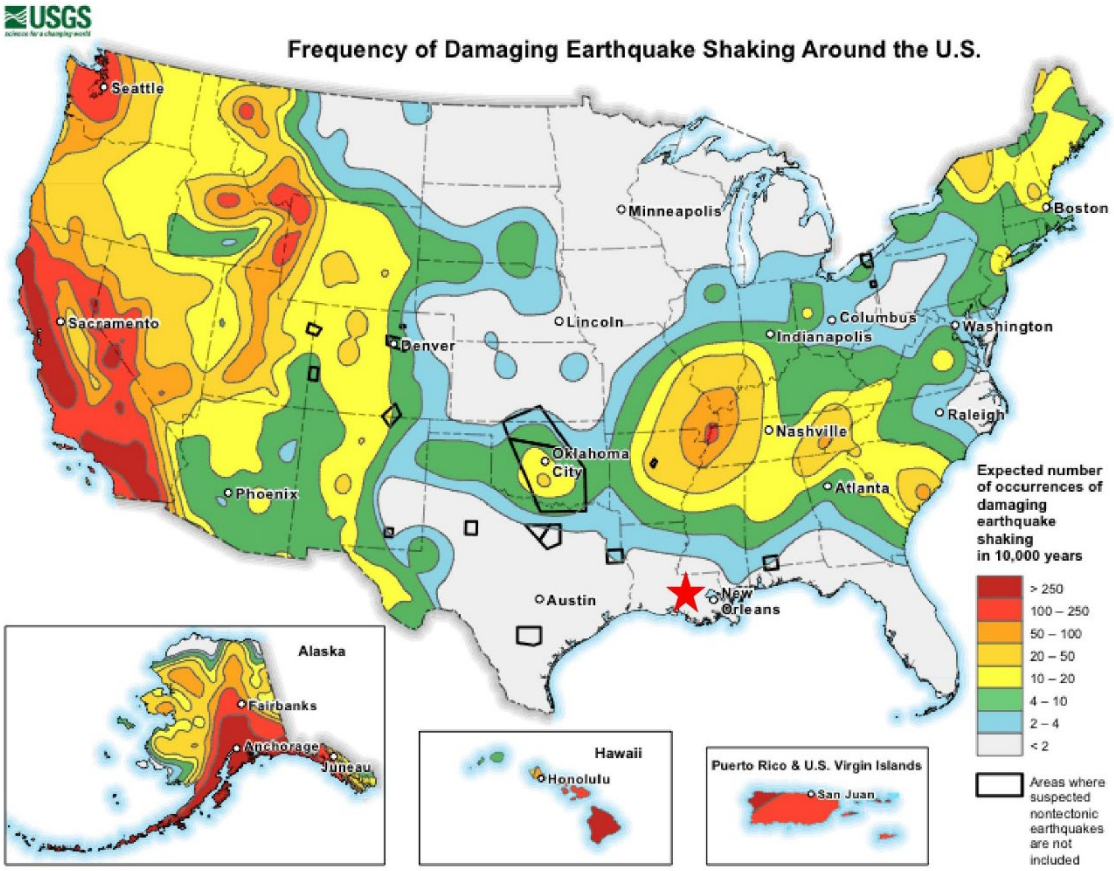

Figure 1-61 – Predicted damaging earthquake shaking around the U.S., with the red star indicating the location of the proposed project (Frequency of Damaging Earthquake Shaking Around the U.S., retrieved 2023).

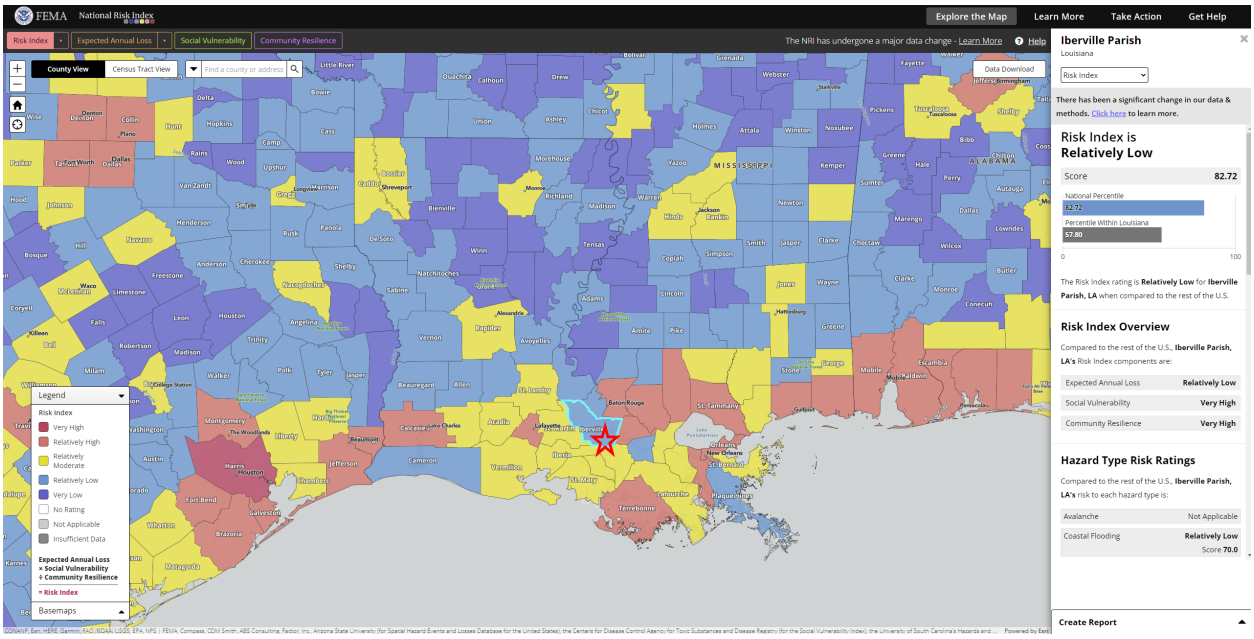

Figure 1-62 – Risk Index Map and the Location of the Proposed Project (National Risk Index FEMA, 2023)

1.12 Conclusion

The site characterization of the proposed White Castle Project and subject injection wells, WC IW-B No. 001 and No. 002, indicates that the Miocene sandstones have sufficient porosity, permeability, and lateral continuity, and are of sufficient depth and thickness to store the proposed amount of CO_2. The [redacted] shale at the site location has low enough permeability and sufficient thickness and lateral continuity of mudstone beds to serve as the primary upper confining zone. At the site, the [redacted] shale has low enough permeability and sufficient thickness and lateral continuity of mudstone beds to serve as the lower confining zone. Potential geologic CO_2 migration pathways in the Miocene injection zones within the AOR are identified, located, characterized, and modeled and determined to be of low risk. No wellbores are located within the AOR. Upon issuance of the Class VI Order to Construct, additional data will be collected and assessed to ensure the site remains low risk for CO_2 injection and storage.

Larger scale versions of the structure maps, cross sections, reference map, and reports are available in *Appendix B.*

Appendix B-1: [redacted] Unit, Top of Structure Map
Appendix B-2: [redacted] Unit, Top of Structure Map
Appendix B-3: [redacted] Structure Map
Appendix B-4: [redacted] Unit, Isopach Map
Appendix B-5: Net Upper Confining Isopach Map
Appendix B-6: Injection Zone, Gross Isopach Map

Appendix B-7:	Net Injection Interval Isopach Map
Appendix B-8:	Lentic Jeff Unit, Lower Confining Zone Isopach Map
Appendix B-9:	Cross Section Reference Map
Appendix B-10:	S-N Structural Cross Section
Appendix B-11:	S-N Stratigraphic Cross Section
Appendix B-12:	W-E Structural Cross Section
Appendix B-13:	W-E Stratigraphic Cross Section
Appendix B-14:	[redacted] Sidewall Core Report
Appendix B-15:	RFS ID No. 202206840-02 Complete Water Analysis Report
Appendix B-16:	NW-SE USDW Structural Cross Section
Appendix B-17:	SW-NE USDW Structural Cross Section
Appendix B-18:	USDW Structure / Cross Section Reference Map
Appendix B-19:	USGS Potentiometric Surface Report
Appendix B-20:	USGS Potentiometric Surface Map

1.13 References

Aird, P. (2019). *Deepwater Geology & Geoscience*. Retrieved from ScienceDirect: https://www.sciencedirect.com/topics/engineering/overburden-stress

Bankey, V., & Daniels, D. L. (2008). *Arkansas and Louisiana aeromagnetic and gravity maps and data—A website for distribution of data*. Retrieved from U.S. Geological Survey Data Series 352: https://pubs.usgs.gov/ds/352/index.html

Bretan, P. (2022). Assessing the predictive capability of the empirical Shale Gouge Ratio–buoyancy pressure calibration: implications for estimating CO2 column heights. *The Geological Society of London*.

Bretan, P. Y. (2003). Using calibrated shale gouge ratio to estimate hydrocarbon column heights. *AAPG*.

Bump, A. P., Bakshian, S., Ni, H., Hovorka, S. D., Olariu, M. I., Dunlap, D., . . . Meckel, T. A. (2023). Composite confining systems: Rethinking geologic seals for permanent CO2 sequestration. *BEG*.

Chamberlain, E. L. (2012). Depositional environments of Upper Miocene through Pleistocene siliciclastic sediments, Baton Rouge aquifer system, southeastern Louisiana. *Louisiana State University, Department of Geology and Geophysics, Master's Theses 4062*.

Collier, A. L., & Sargent, P. B. (2015). Water Use in Louisiana. *Louisiana Department of Transportation and Development, U.S. Geological Survey Report No. 18*.

Combellas-Bigott, R. I., & Galloway, W. E. (2005). Depostional and structural evolution of the middle Miocene depositonal episode, eas-central Gulf of Mexico. *The American Association of Petroleum Geologist*.

Cordell, L., Keller, G., & Hildenbrand, T. (1982). Bouguer gravity map of the Rio Grande Rift, Colorado, New Mexico, and Texas. *U.S. Geological Survey Geophysical Investigations Series*.

Crone , A., & Wheeler, R. (2000). *Data for Quaternary faults, liquefaction features, and possible tectonic features in the Central and Eastern United States, east of the Rocky Mountain front.* U.S. Geological Survey.

Dutch, S. (2020). *Gravity and Magnetic Maps of the United States*. Retrieved from Steven Dutch Home Page: https://stevedutch.net/stategeophmaps/lagphmap.htm

Fillon, R. H., & Lawless, P. N. (2000). Lower Miocene-Early Pliocene Deposystems in the Gulf of Mexico: Regional Sequence Relationships. *Gulf Coast Association of Geological Societies Transactions, Volume L*.

Frequency of Damaging Earthquake Shaking Around the U.S. (retrieved 2023). *USGS sources include Earthquake Hazards Program*. Retrieved from https://www.usgs.gov/media/images/frequency-damaging-earthquake-shaking-around-us

Galloway, W. (2008). Sedimentary Basins of the World, Chapter 15: Depositional Evolution of the Gulf of Mexico Sedimentary Basin. 505-549.

Galloway, W. E. (2008). Sedimentary Basins of the World, Chapter 15: Depositional Evolution of the Gulf of Mexico Sedimentary Basin. 505-549.

Galloway, W., Ganey-Curry, P., Li, X., & Buffler, R. (2000). Cenozoic Depostional History of the Gulf of Mexico Basin. *AAPG*, 1743-1774.

Gold, P. (1985). Diagenesis in Upper Miocene Sandstones, Louisiana Gulf Coast: ABSTRACT. *AAPG Bulletin*, 257.

Griffith, J. M. (2003). Hydrogeologic Framework of Southeastern Louisiana. *Louisiana Department of Transportation and Development, U.S. Geological Survey, Water Resources Technical Report No. 72*.

Hulsey, J. (2016). Applying modern interpretation techniques to old hydrocarbon fields to find new reserves: A case study in the onshore Gulf of Mexico, U.S.A. *University of New Orleans Theses and Dissertations* .

Jolley, S., Stuart, G., & Freeman, S. (2007). Progressive evolution of a late-orogenic thrust system, from duplex development to extensional reactivation and disruption: Witwatersrand Basin, South Africa, In. *Deformation of the Continental Curst. Geologic Society*, 543-569.

Karolyte, R., Johnson, G., Yeilding, G., & Gilfillan, G. (2020). Fault Seal modelling – the influence of fluid properties on fault sealing capacity in hydrocarbon and CO2 systems. *Petroleum Goescience*, 481-497.

Lindaman, M. A., & White, V. E. (2021). Water Resources of Iberville Parish, Louisiana. *U.S. Geological Survey*. Retrieved from https://doi.org/10.3133/fs20213014

Lu, J., Carr, D. L., Treviño, R. H., Rhatigan, J.-L. T., & Fifariz, R. (2017). Evaluation of Lower Miocene Confining Units for CO2 Storage, Offshore Texas State Waters, Northern Gulf of Mexico, USA. *Bureau of Economic Geology* .

Mark-Moser, M., Miller, R., Rose, K., Bauer, J., & Disenhof, C. (2018). Detailed Analysis of Geospatial Trends of Hydrocarbon Accumulations, Offshore Gulf of Mexico. *National Energy Technology Labratory* .

McGuire, V., Seanor, R., Asquith, W., Kress, W., & Strauch, K. (2019). Potentiometric surface of the Mississippi River Valley alluvial aquifer, Spring 2016. *U.S. Geological Survey Scientific Investigations Map 3439*. Retrieved from https://doi.org/10.3133/sim3439

Meckel, T. P., & Trevino, R. (2014). *Gulf Of Mexico Miocene Co2 Site Characterization Mega Transect, Final Scientific/technical Report (Revised).* U. S. Department of Energy National Energy Technology Laboratory.

Meckel, T., & Trevino, R. (2014). GULF OF MEXICO MIOCENE CO2 SITE CHARACTERIZATION MEGA TRANSECT. *Bureau of Economic Geology*.

National Risk Index FEMA, Vermilion Parish, Louisiana. (2023, 04). Retrieved from https://hazards.fema.gov/nri/learn-more

Nwagwu, E. A., Emujakporue, G. O., Ugwu, S. A., & Oghonya, R. (2019). Lithofacies and Depositional Environment from Geophysical Logs of EMK Field, Deepwater Niger Delta, Nigeria. *Department of Geology, University of Port Harcourt, Nigeria*.

Olariu, M. I., DeAngelo, M., Dunlap, D., & Treviño, R. H. (2019). High frequency (4th order) sequence stratigraphy of Early Miocene deltaic shorelines, offshore Texas and Louisiana. *Bureau of Economic Geology*.

Peel, F. J., Travis, C., & Hossack, J. (1995). Genetic structural provinces and salt tectonics of the Cenozoic offshore U.S. Gulf of Mexico: a preliminary analysis. *AAPG*, 153-175.

Petersen, M., Shumway, A., Powers, P., Charles, M., Moschetti, M., Frankel, A., . . . Zeng, Y. (2019). The 2018 update of the US National Seismic Hazard Model: Overview of model and implications. *Earthquake Spectra, 36*, 6-36. doi:10.1177/8755293019878199

Plouff, D. (1977). Preliminary documentation for a FORTRAN program to compute gravity terrain corrections based on topography digitized on a geographic grid. *U.S. Geological Survey*.

Roberts-Ashby, T. L., Brennan, S. T., Buursink, M. L., Covault, J. A., Craddock, W. H., II, R. M., . . . De, C. A. (2012). Geologic framework for the national assessment of carbon dioxide storage resources: U.S. Gulf Coast. *USGS*.

Smith , R. L., & Tieh, T. T. (1984). DEPOSITION, COMPACTION, AND MINERALOGICAL ALTERATION OF MIOCENE SANDSTONES, SOUTH LOUISIANA. *GULF COAST ASSOCIATION OF GEOLOGICAL SOCIETIES*.

Totten, M. (2002). Characteristics of mixed-layer smectite/illite density separates during burial diagenesis. *American Mineralogist*, 1571-1579.

Treviño, R. H., & Rhatigan, J.-L. T. (2017). Regional Geology of the Gulf of Mexico and the Miocene Section of the Texas Near-Offshore Waters. *Bureau of Economic Geology*.

USGS U.S. Quaternary Faults. (2023, 04). Retrieved from https://usgs.maps.arcgis.com/apps/webappviewer/index.html?id=5a6038b3a1684561a9b0aadf88412fcf

Watson, S. T. (1965). Petrography and Lithostratigraphy of Some South Louisiana Subsurface Tertiary Rocks. *Louisiana State University and Agricultural & Mechanical College*.

William E. Galloway, P. E.-C. (2000). Cenozoic depositional history of the Gulf of Mexico basin. *The American Association of Petroleum Geologists.*

Wu, X. a. (2002). Upper Miocene Depositional History of the Central Gulf of Mexico Basin. *Department of Geological Sciences and Institute for Geophysics*.

Xu, J. S. (2022). Quantifying the relative contributions of Miocene rivers to the deep Gulf of Mexico using detrital zircon geochronology: Implications for the evolution of Gulf Basin circulation and regional drainage. *Basin Research*, 1-21.

Yassir, N., & Zerwer, A. (1997). Stress Regimes in the Gulf Coast, Offshore Louisiana: Data from Well-Bore Breakout Analysis. *AAPG*, 293-307.

Yeilding , G. (2002). Shale gouge ratio— Calibration by geohistory, in A. G. Koestler and R. Hunsdale, Hydrocarbon seal quantification. *Norwegian Petroleum Society Special Publication*, 1-15.

Yielding, G., Freeman, B., & Needham, D. T. (1997). Fault seal quantitative prediction: shale smear factor, shale gouge ratio, and smear gouge ratio. *AAPG*.